AD-A221 512

# REPORT DOCUMENTATION PAGE

| 1a. REPORT SECURITY CLASSIFICATION Unclassified | 1b. RESTRICTIVE MARKINGS |
|---|---|

| 2a. SECURITY CLASSIFICATION AUTHORITY | 3. DISTRIBUTION / AVAILABILITY OF REPORT |
|---|---|
| 2b. DECLASSIFICATION / DOWNGRADING SCHEDULE | Approved for public release; Distribution unlimited |

| 4. PERFORMING ORGANIZATION REPORT NUMBER(S) | 5. MONITORING ORGANIZATION REPORT NUMBER(S) |
|---|---|
| | **AFOSR·TR· 90-0440** |

| 6a. NAME OF PERFORMING ORGANIZATION Department of Physics University of Wisconsin | 6b. OFFICE SYMBOL (If applicable) | 7a. NAME OF MONITORING ORGANIZATION Air Force Office of Scientific Research/NP |
|---|---|---|

| 6c. ADDRESS (City, State, and ZIP Code) 1150 University Ave. Madison, WI 53706 | 7b. ADDRESS (City, State, and ZIP Code) Building 410 Bolling AFB DC 20332-6448 |
|---|---|

| 8a. NAME OF FUNDING / SPONSORING ORGANIZATION Air Force Office of Scientific Research | 8b. OFFICE SYMBOL (If applicable) | 9. PROCUREMENT INSTRUMENT IDENTIFICATION NUMBER AFOSR - 84 - 0328 |
|---|---|---|

| 8c. ADDRESS (City, State, and ZIP Code) Bolling Air Force Base Washington, DC 20332 | 10. SOURCE OF FUNDING NUMBERS | | | |
|---|---|---|---|---|
| | PROGRAM ELEMENT NO. | PROJECT NO. | TASK NO. | WORK UNIT ACCESSION NO. |
| | 61102F | 2301 | A7 | |

11. TITLE (Include Security Classification)
Final Report on Research on Optogalvanic Effects (U)

12. PERSONAL AUTHOR(S)
J. E. Lawler

| 13a. TYPE OF REPORT Final | 13b. TIME COVERED FROM 30 Sep 84-31 Aug 89 | 14. DATE OF REPORT (Year, Month, Day) 12/30/89 | 15. PAGE COUNT 54 |
|---|---|---|---|

16. SUPPLEMENTARY NOTATION

| 17. COSATI CODES | | | 18. SUBJECT TERMS (Continue on reverse if necessary and identify by block number) |
|---|---|---|---|
| FIELD | GROUP | SUB-GROUP | |
| | | | |
| | | | |

19. ABSTRACT (Continue on reverse if necessary and identify by block number)
Highly accurate elective field maps, gas density measurements, and a model of ion transport were combined to determine the current balance at the surface of a cold aluminum cathode. The ratio of ion to electron current was found to be 3.3 at the cathode surface. This ratio is independent of total discharge current from a near normal cathode fall of 173V to a highly abnormal cathode fall of 600V

| 20. DISTRIBUTION / AVAILABILITY OF ABSTRACT ☒ UNCLASSIFIED/UNLIMITED ☒ SAME AS RPT. ☒ DTIC USERS | 21. ABSTRACT SECURITY CLASSIFICATION Unclassified |
|---|---|
| 22a. NAME OF RESPONSIBLE INDIVIDUAL Lt Col Bruce L. Smith | 22b. TELEPHONE (Include Area Code) 202/767-4908 | 22c. OFFICE SYMBOL NP |

**DD FORM 1473, 84 MAR**   83 APR edition may be used until exhausted.   SECURITY CLASSIFICATION OF THIS PAGE
All other editions are obsolete.

90 05 10 109

Research on Optogalvanic Effects

Final Report to the

U. S. Air Force Office of Scientific Research

from

J. E. Lawler, Principal Investigator

Department of Physics, College of Letters and Science

The University of Wisconsin

Madison, Wisconsin 53706

Proposal Number: 87NP153, 84NP299

Grant Number: AFOSR-84-0328

Period Covered by Report: Sept. 30, 1984 to Sept. 30, 1989

| Accession For | |
|---|---|
| NTIS GRA&I | ☒ |
| DTIC TAB | ☐ |
| Unannounced | ☐ |
| Justification | |
| By | |
| Distribution/ | |
| Availability Codes | |
| Dist | |

A-1

Table of Contents

# I. Statement of Work

We propose to continue basic research on optogalvanic effects. The primary goals of the research are to develop a detailed quantitative understanding of the cathode fall region in cold cathode discharges, and to develop detailed quantitative understanding of perturbations in the cathode fall region. The major experimental challenges to be addressed in this research are: (1) to develop and apply laser diagnostics for measuring the importance of each mechanism responsible for electron emission from a cold cathode and (2) to develop and apply laser diagnostics for the negative glow region of cold cathode discharges. The mechanisms responsible for electron emission from a cold cathode are ion, metastable atom, and UV photon bombardment. The fraction of the electron emission produced by each mechanism and its dependence on discharge conditions will be studied. The key properties of the negative glow to be measured are the density and temperature of the low energy electron gas in the region. The dependence of the electron density and temperature on discharge conditions will be studied. The major theoretical challenges to be addressed in this research are: (1) the development of a nonequilibrium fluid model for the cathode fall-negative glow region, and (2) the modeling of perturbations at the cathode surface and in the cathode fall region using the nonequilibrium fluid model. Basic research on the cathode fall region of diffuse discharges will benefit many areas of pulsed power engineering. One practical goal of this research is to identify and study key physical processes in the cathode fall region which can be used in a laser controlled diffuse discharge switch.

## II.  Progress on Experimental Problems

The cathode region of diffuse discharges is the least understood and yet most important region for many discharge applications.  The primary difficulty in modeling the cathode fall is due to the large and rapidly changing E/N (electric field divided by ground state atom density).  One result of this E/N behavior is failure of the electron energy distribution function to be in hydrodynamic equilibrium with the local E/N.[1]  It is not satisfactory to use electron drift velocities, first Townsend coefficients, and excitation coefficients which are determined as a function of E/N in equilibrium to describe the behavior of the electrons if they are not in hydrodynamic equilibrium with the local E/N.  A more quantitative understanding of the cathode fall is important to the development of laser controlled and electron beam controlled opening switches.  The cathode fall region is also important because it determines the stability of many gas phase pulsed power devices.  Optogalvanic effects are amplified in the cathode fall, hence a laser controlled opening switch will likely depend on perturbing the cathode fall region.[2]

Optogalvanic diagnostic methods and laser induced fluorescence are the experimental tools needed to develop a more quantitative understanding of the cathode fall.  We developed, shortly before the beginning of Grant AFOSR-84-0328, a powerful new diagnostic for mapping space charge fields in discharge plasmas.[3,4]  This diagnostic is based on optogalvanic detection of Rydberg atoms.  We used this diagnostic and others during subsequent years of research under AFOSR 84-0328 to develop a more quantitative understanding of the cathode region.

One of the uses of the electric field diagnostic is to measure the current balance or ratio of ion to electron current at the surface of a cold cathode.[5] A reprint describing this work is included as Appendix A. We needed, besides very accurate field measurements, a measurement of the gas density reduction due to heating[6] and a realistic model of ion transport in the cathode fall.[7] The issue of ion transport in the cathode fall was settled using analytic Green's function solutions to the Boltzmann equation for ions. The solutions were used to calculate the equilibration distance for ions. These solutions include: (1) symmetric charge exchange in the cold gas approximation, (2) a distributed ion source term from electron impact ionization, and (3) the effects due to a large field gradient. We define the equilibration distance to be the distance, from the cathode fall-negative glow boundary, required for the average velocity of the ions to each 90% of their equilibrium drift velocity. The equilibration distance is 1.7 mean-free-paths for a planar source of ionization near the cathode fall-negative glow boundary where the electric field extrapolates to zero. The equilibration distance is 6 mean-free-paths for a uniform source of ionization. These two limiting cases bracket a realistic case in which ionization peaks near the boundary. The limiting cases provide a rigorous proof that ions are equilibrated when more 6 mean-free-paths from the cathode fall-negative glow boundary. A reprint of this paper is included as Appendix B.

The highly accurate electric field maps, gas density measurements, and model of ion transport were combined in determining the current balance at the surface of a cold aluminum cathode. We found that the ratio of ion to electron current is 3.3 at the cathode surface. This ratio is independent of total discharge current from a near normal cathode fall of 173V to a highly abnormal cathode fall of 600V as reported in Appendix A.

We published in September 1988 a major Physical Review A article entitled "Laser Optogalvanic and Fluorescence Studies of the Cathode Region of a Glow Discharge".[8] A reprint of this paper is included as Appendix C. This paper is a summary of four years of our work on the cathode region; it provides a detailed microscopic description of most of the important features of the cathode region. This paper used a fresh approach for addressing one of the key issues of the cathode region. The relative size of the ion current versus discharge current at the cathode fall-negative glow boundary has been controversial for more than 50 years.[9-12] Theory has not resolved the issue. It is very difficult to carry fully self-consistent non-equilibrium calculations across the cathode fall-negative glow boundary. This boundary is analogous to a shock front. Knowledge of the size of the ion current at the cathode fall-negative glow boundary provides an essential boundary condition for constructing a realistic self-consistent model of the cathode fall region.

Our research indicated that ions carry a negligible fraction of the discharge current at the cathode fall-negative glow boundary. We came to this conclusion by comparing an empirical current balance, or ratio of ion to electron current, at the cathode surface to state-of-the-art Monte Carlo simulations of electron avalanches in the cathode fall. We found that there is enough ionization in the cathode fall to account for all of the ions reaching the cathode. The Monte Carlo simulations were performed using the null-collision method developed by Boeuf and Morode.[13]

This major paper also includes our first result on the density and temperature of the low energy electrons in the negative glow. The development of electron diagnostics for use in the negative glow is identified as a task in the attached "Statement of Work". We used laser induced fluorescence to produce maps of the relative density of singlet and triplet He metastables.

Our maps cover the high field cathode fall region and low field negative glow region. Low energy electrons are confined to the low field negative glow region. A high density of low energy electrons produces a collisional coupling of the singlet and triplet He metastable populations. Singlet and triplet He metastable populations are not coupled by neutral atom collisions because of a spin selection rule. The observation of a severe suppression of the singlet metastable population in the negative glow provides direct spectroscopic information on the low energy electron gas in the negative glow. The suppression enables us to put limits on the electron temperature ($0.025$ eV $\leq k_B T_e \leq 0.25$ eV) and density ($n_e \geq 2 \times 10^{11}$ cm$^{-3}$) in the negative glow. The experimental observations actually provide a constraint on the electron temperature and density in the negative glow. A unique temperature and density was determined by combining the constraint with information from Monte Carlo simulations.

We recognized that it is desirable to determine the electron density and temperature without using the results of Monte Carlo simulations. More recently we developed a second laser diagnostic which complements the experimental work described in the preceeding paragraph. This diagnostic is reported in the reprint (Appendix D) entitled "Electron Temperature and Density Diagnostics in a Helium Glow Discharge", which was published in Physical Review Letters.[14] The diagnostic is based on collisional excitation transfer between low Rydberg levels. A measurement of the collisional transfer rate provides a second relation between the density and temperature of the low energy electrons in the negative glow. This Rydberg atom diagnostic is based on an endothermic process, and yields a relation in which $n_e$ decreases with increasing $T_e$. The diagnostic described in the preceeding paragraph is based on the exothermic reaction which depletes the singlet metastables. It yields a relation in which

$n_e$ increases with increasing $T_e$. The intersection of these two relations provides the density and temperature of the low energy electrons in the negative glow. These two laser diagnostics provide critical information on the negative glow region of cold cathode discharges. This was one of our major experimental challenges in the original Statement of Work.

### III. Progress on Theoretical Problems

The primary theoretical problem to be addressed in this research is the development of self-consistent nonequilibrium models for the cathode fall and negative glow regions. We published a paper entitled "A Framework for Modeling the Cathode Fall Illustrated with a Single Beam Model" during August 1988 in the Journal of Applied Physics.[15] This paper presents the appropriate mathematical structure for modeling the cathode region. The single beam approximation used for the electron distribution function is the simplest possible approximation. It produces good qualitative agreement in general, and produces good quantitative agreement for the near normal cathode fall.

We continued theoretical research on modeling the cathode region of glow discharges. Originally we planned to pursue fully self-consistent models based on what we have called a nonequilibrium fluid approach. In these calculations a model distribution function with spatially dependent parameters is substituted into the Boltzmann equation for electrons. Integral moments of the Boltzmann equation provide a set of coupled ordinary differential equations which are then solved to determine the spatial dependence of the parameters in the model distribution function. The single beam model is a primitive version of such a calculation. We initially suspected that kinetic theory approaches were likely to be too slow or too numerically intensive for self-consistent calculations. Our collaborator, Professor W. N. G. Hitchon, convinced us to pursue a full kinetic theory approach based on his "Convective Scheme". This approach has important advantages over other kinetic theory approaches. It is inherently stable because it is an integral rather than differential calculation. The Convective Scheme has a speed advantage because it is not limited by the Courant-Friedrichs-Lewy criterion. This criterion limits step size in the finite difference methods for solving differential equations. The

Convective Scheme is analogous to a Green's function method for solving differential equations.

The Convective Scheme has an enormous speed advantage over Monte Carlo methods, but it retains some of the attractive features of the Monte Carlo methods. Both the Convective Scheme and Monte Carlo methods are relatively intuitive and easy to code. A great deal of detail on collision processes (such as an anisotropic angular distribution) can be included in both types of calculations. The Convective Scheme can be described as a Monte Carlo calculation in which "clumps" of particles, rather than individual particles, are tracked. Much better statistics are achieved by dealing with large numbers of particles.

The speed of the Convective Scheme is adequate for fully self-consistent calculations. We applied the Convective Scheme in a self-consistent kinetic model of the cathode fall region.[16] A reprint of this work is included as Appendix E.

Our ultimate goal is to apply Convective Scheme models to transient discharges. During the last months of AFOSR 84-0328, we did succeed in using the Convective Scheme to produce a fully self-consistent kinetic calculation of a sinusoidal steady-state radio frequency discharge plasma.[17] This work is an intermediate step between dc and transient discharge. This model is probably the first self-consistent, electrode-to-electrode kinetic model of a discharge plasma. A reprint of this work is included as Appendix F.

## IV. References

1. P. Segur, M. Yousfi, J. P. Boeuf, E. Marode, A. J. Davies, and J. G. Evans in _Electrical Breakdown and Discharges in Gases_, edited by E. E. Kunhardt and L. H. Luessan (Plenum, NY, 1983), Part A, p. 331.

2. D. K. Doughty and J. E. Lawler, Appl. Phys. Lett. $\underline{42}$, 234 (1983).

3. D. K. Doughty and J. E. Lawler, Appl. Phys. Lett. $\underline{45}$, 611 (1984).

4. D. K. Doughty, S. Salih, and J. E. Lawler, Phys. Lett. $\underline{103A}$, 41 (1984).

5. D. A. Doughty, E. A. Den Hartog, and J. E. Lawler, Phys. Rev. Lett. $\underline{58}$, 2668 (1987).

6. D. K. Doughty, E. A. Den Hartog, and J. E. Lawler, Appl. Phys. Lett. $\underline{46}$, 352 (1985).

7. J. E. Lawler, Phys. Rev. A $\underline{32}$, 2977 (1985).

8. E. A. Den Hartog, D. A. Doughty, and J. E. Lawler, Phys. Rev. A $\underline{38}$, 2471 (1988).

9. M. J. Druyvesteyn and F. M. Penning, Rev. Mod. Phys. $\underline{12}$, 87 (1940).

10. W. H. Long, _Plasma Sheath Processes_, Technical Report AFAPL-TR-79-2038.

11. K. G. Emeleus, J. Phys. D: Appl. Phys. $\underline{14}$, 2179 (1981).

12. J. H. Ingold in _Gaseous Electronics_ ed. by M. N. Hirsh and H. J. Oskam (Academic, New York 1978) Vol. I, p. 24.

13. J. P. Boeuf and E. Marode, J. Phys. D $\underline{15}$, 2169 (1982).

14. E. A. Den Hartog, T. R. O'Brian, and J. E. Lawler, Phys. Rev. Lett. $\underline{62}$, 1500 (1989).

15. T. J. Sommerer, J. E. Lawler, and W. N. G. Hitchon, J. Appl. Phys. $\underline{64}$, 1775 (1988).

16. T. J. Sommerer, W. N. G. Hitchon, and J. E. Lawler, Phys. Rev. A $\underline{39}$, 6356 (1989).

17. T. J. Sommerer, W. N. G. Hitchon, and J. E. Lawler, Phys. Rev. Lett. $\underline{63}$, 2361 (1989).

V. Publications and Presentations During This Reporting Period

A. Publications

1. "Optogalvanic Measurements of Gas Temperature in the Cathode Fall", by D. K. Doughty, E. A. Den Hartog, and J. E. Lawler, Appl. Phys. Lett. 46, 352 (1985).

2. "Equilibration Distance of Ions in the Cathode Fall", by J. E. Lawler, Phys. Rev. A 32, 2977 (1985).

3. "Optogalvanic Diagnostics of the Cathode Fall", by J. E. Lawler, D. K. Doughty, E. Den Hartog, and E. Benck, in Digest of the Technical Papers 5th IEEE Pulsed Power Conference, ed. by P. J. Turchi and M. F. Rose, p. 371 (1986).

4. "Optogalvanic Effects in the Cathode Fall" by J. E. Lawler, D. K. Doughty, E. A. Den Hartog, and S. Salih, in Radiative Processes in Discharge Plasmas, edited by J. M. Proud and L. H. Luessen, NATO ASI Series (Plenum Press, New York 1986) Series B, Vol. 149, p. 525.

5. "Optogalvanic Detection of Rydberg Atom: A Powerful New Discharge Diagnostic", by J. E. Lawler, D. K. Doughty, and E. A. Den Hartog, in I CALEO '85 Technical Digest (Laser Institute of America, Toledo 1986).

6. "An Investigation of the Cathode Fall", by D. A. Doughty and J. E. Lawler, in Materials Research Society Symposium Proceedings Vol. 68, edited by J. W. Coburn, R. A. Gottscho, and D. W. Hess, p. 141.

7. "Current Balance at the Surface of a Cold Cathode", by D. A. Doughty, E. A. Den Hartog, and J. E. Lawler, Phys. Rev. Lett. 58, 2668 (1987).

8. "Studies of the Cathode Region Using Optogalvanic Effects", by J. E. Lawler and D. A. Doughty, in The Physics of Ionized Gases, edited by J. Puric and D. Belic, (World Scientific, Singapore 1987), p. 293.

9. "Current Balance at the Surface of a Cold Cathode", by J. E. Lawler, E. A. Den Hartog and D. A. Doughty in the Digest of Technical Papers of the 6th IEEE Pulsed Power Conference, edited by B. H. Bernstein and P. J. Turchi, p. 85 (1988).

10. "Laser Optogalvanic and Fluorescence Studies of the Cathode Region of a Glow Discharge", by E. A. Den Hartog, D. A. Doughty, and J. E. Lawler, Phys. Rev. A 38, 2471 (1988).

11. "A Framework for Modeling the Cathode Fall Illustrated with a Single Beam Model" by T. J. Sommerer, J. E. Lawler and W. N. G. Hitchon, J. Appl. Phys. 64, 1775 (1988).

12. "A Self-Consistent Kinetic Model of a Discharge Plasma", by W. N. G. Hitchon, T. J. Sommerer, and J. E. Lawler, to be published in the Digest of Technical Papers of the 7th IEEE Pulsed Power Conference.

13. "Laser Studies of the Cathode Region of Glow Discharges", by J. E. Lawler and E. A. Den Hartog, to be published in the Proceedings of the International Conference on Phenomena in Ionized Gases ICPIG 1989.

14. "Mapping and Modeling of the Cathode Fall and Negative Glow Regions", by J. E. Lawler, E. A. Den Hartog, W. N. G. Hitchon, T. R. O'Brian, and T. J. Sommerer, to be published in Proceedings of the NATO Advanced Research Workshop on the Physics and Application of High Power Hollow Electrode Glow Switches 1989.

15. "Optogalvanic Diagnostics for Electric Field, Particle Density, and Flux Density Measurements in Glow Discharge Plasmas", by J. E. Lawler and E. A. Den Hartog, in Proceedings of the 4th International Symposium on Laser Aided Plasma Diagnostics edited by M. Akazaki and K. Muraoka, p. 456 (1989).

16. "Electron Temperature and Density Diagnostics in a Helium Glow Discharge", by E. A. Den Hartog, T. R. O'Brian and J. E. Lawler, Phys. Rev. Lett. 62, 1500 (1989).

17. "A Self-Consistent Kinetic Model of the Cathode Fall of a Glow Discharge". by T. J. Sommerer, W. N. G. Hitchon, and J. E. Lawler, Phys. Rev. A 39, 6356 (1989).

18. "Electron Heating Mechanisms in Helium rf Glow Discharges: A Self-Consistent Kinetic Calculation", by T. J. Sommerer, W. N. G. Hitchon, and J. E. Lawler, Phys. Rev. Lett. 63, 2361 (1989).

B. Presentation and Interactions

1. J. E. Lawler presented on Invited Talk entitled, "Optogalvanic Diagnostics of the Cathode Fall" at the 5th IEEE Pulsed Power Conference in Arlington, VA, June 10-12, 1985.

2. J. E. Lawler presented an Invited Talk entitled, "Optogalvanic Effects in the Cathode Fall", at the NATO Advanced Study Institute on "Radiative Processes in Discharge Plasmas" at Atholl Palace Hotel, Pitlochry, Scotland, June 23 - July 5, 1985.

3. J. E. Lawler presented an Invited Talk entitled "Optogalvanic Detection of Rydberg Atoms: A Powerful New Discharge Diagnostic", at the Laser Institute of America - International Congress on the Application of Lasers and Electro-Optics, at San Francisco, CA, November 11-14, 1985.

4. J. E. Lawler participated in the U. S. C. Workshop on "Research Issues in Power Conditioning", held at the University of Southern California, Los Angeles, CA, December 2-3, 1985.

5. J. E. Lawler provided technical advice to Dr. Norman Chonacky of the Rome Air Development Center on certain laser and spectroscopy problems during 1985.

6. D. A. Doughty presented a talk entitled "An Investigation of the Cathode Fall", at the 1986 Materials Research Society Symposium on Plasma Processing, at Palo Alto, CA, April 15-18, 1986. D. A. Doughty won the prize for "Best Thesis Research" from the Materials Research Society at this meeting.

7. J. E. Lawler presented an Invited Talk entitled "Studies of the Cathode Fall Region Using Optogalvanic Effects", at the XIII Symposium on the Physics of Ionized Gases at Sibenick, Yugoslavia, September 1-5, 1986.

8. The Physics Department of the University of Wisconsin hosted the 39th Gaseous Electronics Conference of the American Physical Society in Madison, WI, October 7-10, 1986. J. E. Lawler served on the local committee for this conference. He presented an Invited Talk entitled "Spectroscopic Studies on the Cathode Fall Region".

9. J. E. Lawler presented a talk entitled "Current Balance at the Surface of a Cold Cathode", at the 6th IEEE Pulsed Power Conference in Crystal City, VA, June 29-July 1, 1987.

10. J. E. Lawler presented a talk entitled "Current Balance at the Surface of a Cold Cathode", at the 40th Gaseous Electronics Conference of the American Physical Society in Atlanta, GA, October 13-16, 1987.

11. E. A. Den Hartog presented a talk entitled "Electron Temperature and Density in the Negative Glow of a He Discharge" at the 41st Gaseous Electronics Conference of the American Physical Society in Minneapolis, MN, October 18-21, 1988.

12. T. J. Sommerer presented a talk entitled "A Framework for Modeling the Cathode Fall Illustrated with a Single Beam Model", at the 41st Gaseous Electronics Conference of the American Physical Society in Minneapolis, MN, October 18-21, 1988.

13. T. J. Sommerer presented a talk entitled "Convective Scheme Modeling of Swarm Experiments and the Cathode Fall", at the 41st Gaseous Electronics Conference of the American Physical Society in Minneapolis, MN, Oct. 18-21, 1988.

14. W. N. G. Hitchon presented a talk entitled "A Self Consistent Kinetic Model of the Cathode Fall of a Discharge Plasma", at the 7th IEEE Pulsed Power Conference in Montery, CA, June 12-14, 1989.

15. J. E. Lawler presented an Invited Talk entitled "Laser Studies of the Cathode Region of Glow Discharges", at the International Conference on Phenomena in Ionized Gases at Belgrade, Yugoslavia, July 10-14, 1989.

16. J. E. Lawler presented an Invited Talk entitled "Mapping and Modeling of the Cathode Fall and Negative Glow Regions", at the NATO Advance Research Workshop on the Physics and Applications of High Power Hollow Electrode Glow Switches in Lillehammar, Norway, July 17-21, 1989.

17. J. E. Lawler presented an Invited Talk entitled "Laser Optogalvanic and Fluorescence Spectroscopy in Glow Discharge Plasmas", at the 7th American Physical Society Topical Conference on Atomic Processes in Plasmas at Gaithersburg, MD, October 2-5, 1989.

18. W. N. G. Hitchon presented a long talk entitled "Kinetic Models of Glow Discharges" at the 42nd Gaseous Electronics Conference of the American Physical Society in Palo Alto, CA, October 17-20, 1989.

19. T. J. Sommerer presented a talk entitled "A Kinetic Discharge Model Applied to the RF Reference Cell", at the 42nd Gaseous Electronics Conference of the American Physical Society in Palo Alto, CA, October 17-20, 1989.

20. J. E. Lawler presented an Invited Talk entitled "Optogalvanic Diagnostics for Electric field, Particle Density, and Flux Density Measurements in Glow Discharge Plasmas", at the 4th International Symposium on Laser Aided Plasma Diagnostics in Fukuoka, Japan, November 20-23, 1989.

VI. Scientific personnel supported by this project and

degrees awarded during this reporting period.

1. J. E. Lawler is Principal Investigator.

2. D. A. Doughty completed all requirements for his Ph. D. in May, 1987. His thesis title is "Investigation of the D. C. Glow Discharge Using Optogalvanic Spectroscopy". The degree was awarded at the August 1987 commencement exercise. D. A. Doughty received awards from Sigma XI and the Materials Research Society for his thesis research.

3. E. A. Den Hartog completed all requirements for her Ph. D. in January 1989. Her thesis title is "Studies of the Cathode Region of the D. C. Glow Discharge". The degree was awarded at the May 1989 commencement exercise.

4. E. C. Benck completed all requirement for his Ph. D. in December 1989. His thesis title is "Optical Diagnostics in Hg Discharges". The degree was awarded at the May 1989 commencement exercise.

5. T. J. Sommerer is a graduate student. He has made excellent progress toward a Ph. D. thesis. He will finish his thesis work in 1990.

6. Visiting Professor R. E. Miers was supported during the summer of 1988. He assisted various students with their experiments.

7. Visiting Professor M. W. Wickliffe was supported during the summer of 1989. He assisted various students with their experiments.

8. T. R. O'Brian is a graduate student. He will complete his graduate studies on a different project.

APPENDIX A   (Pg. 20-23)

# Current Balance at the Surface of a Cold Cathode

D. A. Doughty, E. A. Den Hartog, and J. E. Lawler

*Department of Physics, University of Wisconsin, Madison, Wisconsin 53706*

(Received 9 February 1987)

Recent experimental and theoretical developments, including an electric field diagnostic based on optogalvanic detection of Rydberg atoms, an analytic treatment of ion transport in the cathode fall, and a null collision Monte Carlo technique, are combined to determine the current balance at the surface of a cold cathode in a He glow discharge. The ratio of the ion current to electron current is measured and calculated over a range of current densities from a near-normal to a highly abnormal glow discharge.

New experimental diagnostics and recent theoretical developments are leading to a more quantitative understanding of the cathode-fall region of the glow discharge. The development of detailed quantitative models has been hampered by the nonequilibrium nature of the cathode-fall region. The proximity of the boundary and the large spatial variation of the electric field give rise to an electron distribution function that is not in hydrodynamic equilibrium with the local electric field to gas density ratio $(E/N)$. Therefore, the large data base of electron transport parameters is not directly applicable when modeling the cathode fall. Although the cathode-fall region is the least understood part of a typical discharge, this region is very important from a practical and a fundamental viewpoint.

We measure the current balance at the cathode surface by utilizing an electric field diagnostic and a Boltzmann-equation analysis of ion transport. Spatially resolved electric fields can be measured with either laser-induced fluorescence[1] or optogalvanic detection of Rydberg atoms.[2,3] The latter technique is the most suitable for the discharge studied in this work. The spatial gradient of the electric field determines the space-charge density by Poisson's equation. This space-charge density is almost entirely due to ions since the electron density is negligible in the high electric fields of the cathode-fall region. The ion current density is simply the product of the ion charge density and the average ion velocity.

Analytic nonequilibrium solutions to the Boltzmann equation for ions were used to calculate the equilibration distance of ions in the cathode fall.[4] The calculations included the symmetric-charge-exchange term, a nonuniform field, and a distributed-ion-source term. The average ion velocity is the equilibrium drift velocity for ions more than six mean free paths from the cathode-fall–negative-glow boundary.[4] The cathode fall has a thickness of sixty mean free paths for symmetric charge exchange; thus the equilibrium drift velocity can be used to calculate the ion current density. The difference between the measured total current density and this ion current density is the electron current density. The ratio of the ion-to-electron current at the cathode surface can

be directly compared to a suitable calculation. We use a Monte Carlo code based on a null collision technique to simulate electron avalanches in the cathode fall.[5-7] The average number of ions produced per electron emitted from the cathode in these simulations compares favorably to the empirical ion-to-electron–current ratio.

This "electric field" approach is used to determine the current balance at a cold Al cathode in a 3.5-Torr He discharge over a range of discharge current densities from 0.190 to 1.50 mA/cm$^2$. The current-density range extends from a near-normal cathode-fall voltage of 173 V to a highly abnormal cathode-fall voltage of 600 V. We find that the ratio of ion current to electron current at the cathode is approximately 3.3 over the entire range.

The discharge is produced between flat circular Al electrodes 3.2 cm in diameter and separated by 0.62 cm. The discharge tube is made primarily of glass and stainless steel. Most of the large seals are made with knife-edge flanges on Cu gaskets. The only exceptions are the high-vacuum epoxy seals around the fused silica Brewster windows. A liquid-N$_2$ trapped diffusion pump evacuates the tube to $2 \times 10^{-8}$ Torr. When no liquid N$_2$ is in the trap an ion pump maintains the vacuum to prevent oil from backdiffusing into the system. The leak rate into the discharge tube is approximately $3 \times 10^{-4}$ Torr/d. For discharge operations ultrahigh-purity (0.99999) He is slowly flowed through the system. A capacitive manometer monitors the pressure, which is maintained at 3.5 Torr. The He first passes through a cataphoresis discharge to remove any residual contaminants before entering the main discharge tube. Emission spectra reveal only very weak Al and H impurity lines. In order to perform spatially resolved measurements without disturbing laser alignment the discharge is mounted on a precision translation stage. Optogalvanic effects are detected as a change in discharge current with a boxcar averager. The appropriate laser radiation is produced with a N$_2$-laser–pumped dye-laser system which has a bandwidth of 0.4 cm$^{-1}$. For electric field measurements the dye laser is frequency doubled. The second harmonic is polarized normal to the surface of the electrodes and is focused with a cylindrical lens to a strip 0.01 cm wide
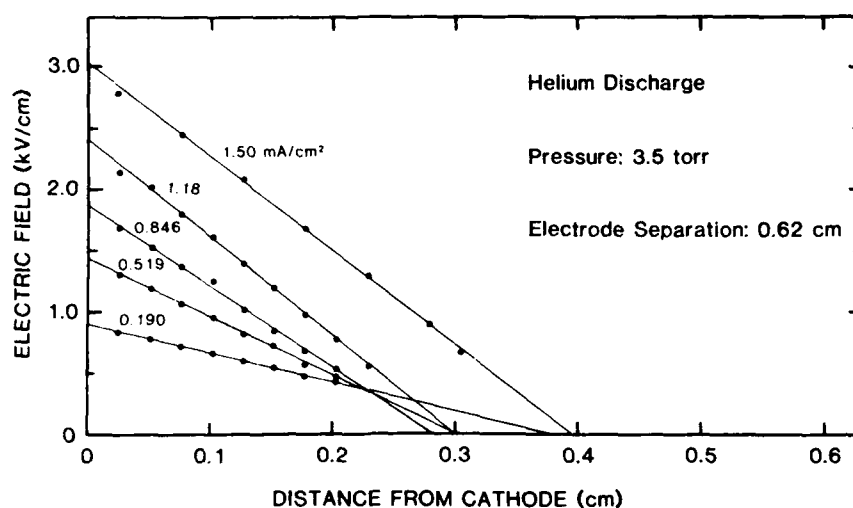
FIG. 1. Electric field as a function of distance from the cathode for the five currents studied. The anode corresponds to the right-hand side of the figure.

and 1 cm long parallel to the electrode surface. Schematics of the apparatus are presented in previous publications.[2,3]

The electric field in the cathode-fall region is mapped by the observing of atomic transitions from heavily populated metastable levels to Rydberg levels. Optogalvanic detection is essential because the fragile Rydberg atoms are collisionally ionized in the discharge long before they can fluoresce. These transitions exhibit a dramatic linear Stark effect because of the large size of Rydberg atoms and because of the small energy gap between states of opposite parity. To interpret Stark spectra a $n \times n$ ($n$ is the principal quantum number) Hamiltonian matrix is diagonalized yielding eigenvalues which are the perturbed energies of the states in the Stark manifold.[8] The eigenvectors can be related to the intensities of the various components in the Stark manifold. Stark spectra are obtained by scanning the frequency of the laser in a fixed spatial position. The width of the Stark manifold, the separation of individual components, or the relative intensities of the components can each be used to determine the field. The $2^1S$ to $11^1P$ transition in He at 321 nm is well suited for measuring fields found in low-pressure discharges. The width of the Stark manifold increases as $n^2$; thus the optimum $n$ is determined by the

magnitude of the fields being studied.

The electric field measurements are summarized in Fig. 1 and Table I for the five discharge current densities, $J_D$. Figure 1 is a plot of electric field as a function of distance away from the cathode. The solid lines are linear fits to the data. This linear behavior persists to very small fields.[9] Table I lists the electric fields at the cathode, $E^0$, and the zero-field positions, $d_c$, which are determined by linearly extrapolating the data. The boundary between the cathode-fall and negative-glow regions is confirmed by a change in magnitude and temporal characteristics of optogalvanic effects at a distance $d_c$ from the surface of the cathode. The excellent agreement between $V_{ef}$, a voltage determined by integrating the field data, and $V_{vm}$, a voltage measured with a digital voltmeter, indicates that the field measurements are on the average accurate to 1%.

The discharge electrodes are water cooled in order to minimize gas heating in the cathode fall. This cooling does not completely eliminate a temperature increase and subsequent density reduction in the abnormal glow. Symmetric charge exchange between positive ions and neutrals converts over half of the input power to heavy-particle translational motion in the cathode fall. The resulting temperature increase is measured from the

TABLE I. Experimentally determined parameters.

| $J_D$ (mA/cm$^2$) | $E^0$ (V/cm) | $d_c$ (cm) | $V_{vm}$ (V) | $V_{ef}$ (V) | $N$ ($10^{16}$ cm$^{-3}$) | $\rho+$ ($10^{-10}$ C/cm$^3$) | $U_+^0$ ($10^5$ cm/s) | $J_+^0$ (mA/cm$^2$) |
|---|---|---|---|---|---|---|---|---|
| 1.50 | 3017 | 0.396 | 600 | 597 | 8.01 | 6.74 | 16.5 | 1.11 |
| 1.18 | 2395 | 0.300 | 356 | 359 | 9.48 | 7.07 | 13.2 | 0.933 |
| 0.846 | 1870 | 0.282 | 261 | 264 | 10.3 | 5.88 | 10.9 | 0.641 |
| 0.519 | 1426 | 0.301 | 211 | 215 | 10.8 | 4.20 | 9.28 | 0.390 |
| 0.190 | 897 | 0.382 | 173 | 171 | 11.2 | 2.08 | 7.12 | 0.148 |

Doppler width of the $2^1S$ to $3^1P$ transition in He at 501.6 nm. An étalon reduces the dye-laser bandwidth to 300 MHz for the Doppler-width measurements which are made by optogalvanic detection. The 501.6-nm transition has a natural width of 92 MHz.[10] Pressure broadening at 3.5 Torr contributes another 146 MHz.[11] Stark broadening adds at most a few hundred megahertz. These contributions are all much smaller than the Doppler width of 3.66 GHz at room temperature. The column labeled $N$ in Table I is the resulting gas-density measurements. The uncertainty ranges from $\pm 3\%$ at low currents to $\pm 6\%$ at the high currents. The gas density is constant throughout the cathode-fall region to within the 3%–6% uncertainty of the measurements.

The ion current density at the surface of the cathode is the product of the ion density, $\rho_+$, and the ion drift velocity at the cathode surface, $U_+^0$. Poisson's equation combined with the electric field data gives the ion density. The uncertainty in $\rho_+$ is comparable to the uncertainty in the field measurements. To determine the drift velocity at low currents Helm's precise mobility data are used.[12] At the high currents the drift velocity is calculated with use of the equilibrium expression,

$$U_+^0 = (2eE^0/M\pi\sigma N)^{1/2}, \qquad (1)$$

where $e$ is the ion charge and $M$ the ion mass. The symmetric-charge-exchange cross section, $\sigma$, is taken from the calculations of Sinha, Lin, and Bardsley.[13] These calculations agree with Helm's experimentally derived cross sections. The uncertainty in $U_+^0$ is $\pm 4\%$ in all cases. The ion current density at the cathode surface, $J_+^0$, is listed in the last column of Table I.

A Monte Carlo code is used to study electron avalanches in the cathode-fall region. Empirical fields and gas densities from Table I are used in the simulations. The position and momentum of individual electrons are followed in a Monte Carlo simulation. The code is based on an adaptation of the null collision technique for nonuniform fields.[5-7] In this approach a null collision cross section is chosen in order to avoid any numerical integration of collision probabilities along an electron's trajectory. The distance between collisions is determined by a random number, and the type of collision is determined by a second random number. If a null collision occurs, the electrons motion is unaffected. We use a code which includes anisotropic elastic scattering, excitation to 24 levels, direct ionization, and other less important processes. We choose the same set of elastic and inelastic cross sections used by Boeuf and Marode.[7,14,15] The Monte Carlo code with these cross sections is tested with use of a uniform $E/N$ of 100 Td [1 Td (townsend) $= 10^{-17}$ V cm$^2$]. The simulation gives an equilibrium townsend coefficient that agrees with experiment. Figure 2 is a histogram of the ionization events per emitted electron as a function of distance
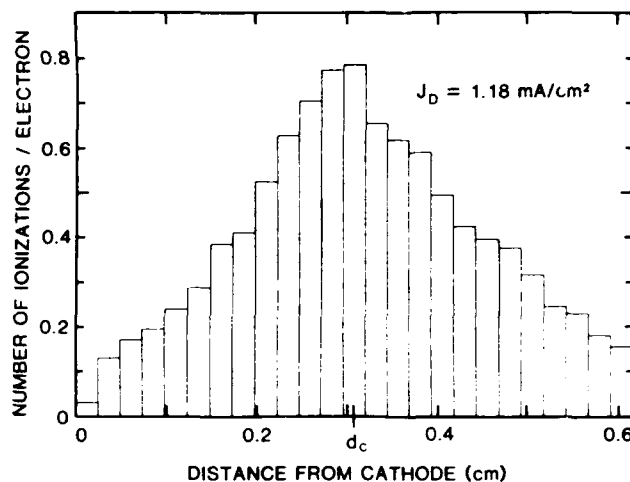


FIG. 2. Typical Monte Carlo histogram giving the total number of ionization events per electron released from the cathode as a function of distance from the cathode. Only those events between 0 and $d_c$ are counted when evaluating the average size of an avalanche.

from the cathode. This ionization peaks at the boundary between the cathode fall and the negative glow indicated by $d_c$. The nonequilibrium behavior of the electrons is evident from the large amount of ionization beyond $d_c$. If all the electrons in the negative glow were in equilibrium, they would produce very little ionization because the local field is small.

Although we have not been able to map the negative-glow field, we have evidence for a high density of low-energy electrons which indicates a very small ($< 10$ V/cm) field. We measure, using laser-induced fluorescence, a significant suppression of the $2^1S$ versus $2^3S$ metastable density in the negative-glow region. Our Monte Carlo simulations indicate only slight differences in the spatial dependence of the $2^1S$ and $2^3S$ production. The suppression is due to the reaction

$$\text{He}(2^1S) + e^- + \text{He}(2^3S) + e^- + 0.79 \text{ eV}. \qquad (2)$$
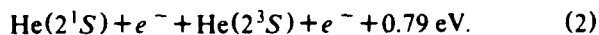
These observations indicate an electron temperature much less than 0.8 eV; otherwise the reaction would readily proceed in the opposite direction. Furthermore, an electron density of from $10^{12}$ to $10^{13}$ cm$^{-3}$ in the negative glow can be inferred from these observations, because the rate of reaction (2) must overwhelm $2^1S$ metastable diffusion.[16,17]

Only ionization produced in the region to the left of $d_c$ contributes to the ion current in the cathode fall. If the ions from the negative glow contributed to the cathode-fall current in a significant way then there must be a large ion current towards the cathode at $d_c$. Equation (1) indicates, however, a relatively small ion velocity because of the weak fields near the cathode-fall–negative-glow boundary. In fact Eq. (1) overestimates the average ion velocity near the negative glow.[4] Since the
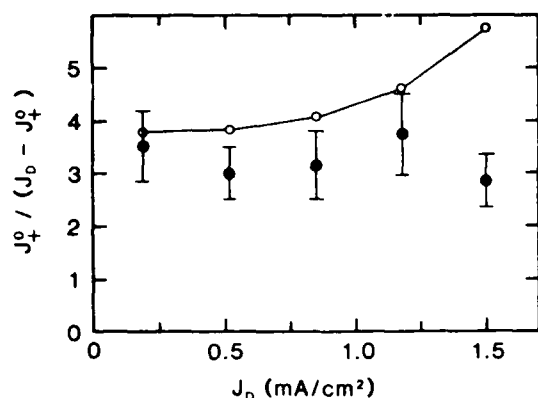
FIG. 3. Ratio of ion to electron current at the cathode, $J_+^0/(J_D - J_+^0)$, as a function of total discharge current density. The experimentally determined values are shown as solid points with a typical uncertainty of $\pm 20\%$. The Monte Carlo results are presented as open circles connected by a line.

charge densities for ions and electrons are nearly equivalent in the negative glow, electrons are carrying the bulk of the current in this region. Ions produced to the right of $d_c$ are lost through recombination and diffusion out of the discharge region.

The empirical ratio of $J_+^0$ to the electron current density at the cathode, $J_D - J_+^0$, is compared in Fig. 3 to the average number of ions produced in the cathode fall per emitted electron as calculated by use of the Monte Carlo simulation. The ratio is only weakly dependent on cathode-fall voltage due to the gas-density reduction from heating. The Monte Carlo simulations are strongly dependent on gas density. A 6% change in the gas density at high currents (the uncertainty) propagates in the simulation to a 20% change in the average avalanche size as that presented in Fig. 3. The imperfect agreement between theory and experiment at high discharge currents is due to the sensitivity of the Monte Carlo simulations to uncertainties in gas density and electron-impact cross sections ($\pm 25\%$). The good agreement at lower currents gives us confidence that we have determined this critical parameter.

The determination of the current balance at the cathode surface is a significant step toward a detailed quantitative model of the cathode-fall region. Yet to be understood is the relative importance of electron emission from the cathode due to ion, metastable, and uv photon bombardment. Ultimately, a direct Boltzmann equation or nonequilibrium fluid model should be coupled with Poisson's equation to predict both the cathode-fall voltage and the spatial dependence of the field. Such an approach should also be able to predict the existence and properties of the negative glow.

[1]C. A. Moore, G. P. Davis, and R. A. Gottscho, Phys. Rev. Lett. **52**, 538 (1984).

[2]D. K. Doughty and J. E. Lawler, Appl. Phys. Lett. **45**, 611 (1984).

[3]D. K. Doughty, S. Salih, and J. E. Lawler, Phys. Lett. **103A**, 41 (1984).

[4]J. E. Lawler, Phys. Rev. A **32**, 2977 (1985).

[5]H. R. Skullerud, J. Phys. D **1**, 1567 (1968).

[6]S. L. Lin and J. N. Bardsley, J. Chem. Phys. **66**, 435 (1977).

[7]J. P. Boeuf and E. Marode, J. Phys. D **15**, 2169 (1982).

[8]M. L. Zimmerman, M. G. Littman, M. M. Kash, and D. Kleppner, Phys. Rev. A **20**, 2251 (1979).

[9]B. N. Ganguly, J. Shoemaker, B. L. Preppernau, and A. Garscadden, J. Appl. Phys. (to be published).

[10]W. L. Wiese, M. W. Smith, and B. M. Glennon, in *Atomic Transition Probabilities, Volume I, Hydrogen Through Neon*, U.S. National Bureau of Standards, National Standard Reference Data Series—4 (U.S. GPO, Washington, D.C., 1966), p. 128.

[11]The pressure-broadening coefficient of $42.0 \pm 2.7$ MHz/Torr at 292 K for the 501.6-nm transition is from J. E. Lawler, Ph.D. thesis, University of Wisconsin, 1978 (unpublished).

[12]H. Helm, J. Phys. B **10**, 3683 (1977).

[13]S. Sinha, S. L. Lin, and J. N. Bardsley, J. Phys. B **12**, 1613 (1979).

[14]G. D. Alkhazov, Zh. Tekh. Fiz. **40**, 97 (1970) [Sov. Phys. Tech. Phys. **15**, 66 (1970)].

[15]R. W. LeBahn and J. Callaway, Phys. Rev. A **2**, 366 (1970).

[16]A. V. Phelps, Phys. Rev. **99**, 1307 (1955).

[17]W. C. Fon, K. A. Berrington, P. G. Burke, and A. E. Kingston, J. Phys. B **14**, 2921 (1981).

APPENDIX B   (Pg. 24-27)

# Equilibration distance of ions in the cathode fall

J. E. Lawler

*Department of Physics, University of Wisconsin, Madison, Wisconsin 53706*
(Received 29 April 1985)

The motion of atomic ions in a rare-gas cathode fall is limited by symmetric charge exchange. Nonequilibrium solutions of the Boltzmann equation for this problem are presented. The distance required for the average ion velocity to approach within 10% of the equilibrium drift velocity is calculated for constant and for linearly increasing fields, with a plane ionization source and with a uniform source. The equilibration distances range from two-thirds to six mean free paths. A rare-gas cathode fall is typically 50–100 mean free paths thick; hence the ion motion may be accurately described by the equilibrium drift velocity throughout most of the cathode fall.

The cathode fall region of glow discharges is the least understood region and yet the most important region for many discharge applications. The primary difficulty in modeling the cathode fall is the failure of the electron distribution function to be in hydrodynamic equilibrium with the local $E/N$ (electric field to gas density ratio). The lack of hydrodynamic equilibrium is caused by the large and rapidly changing $E/N$ and by the proximity of the boundary. New theoretical approaches and recently developed optogalvanic diagnostics should soon lead to a more quantitative understanding of the cathode fall.[1-3] Accurate spatially resolved electric field and gas density (temperature) measurements are used to map the cathode fall region of rare-gas discharges.[2,3] The space-charge density, which is dominated by the positive-ion density, is determined from the spatial derivative of the electric field. The ions are assumed to be in hydrodynamic equilibrium with local $E/N$, and thus the drift velocity of the ions is determined from known ion mobilities and the local $E/N$. The product of the ion density and the ion drift velocity determines the ion-current density. The difference between the total discharge-current density and the ion-current density is the electron-current density. The spatial derivative of the electron-current density provides a map of the ionization rate in the cathode fall. This simple analysis is dependent on the assumptions: (1) that singly charged atomic ions are the dominant species and (2) that the ions are in hydrodynamic equilibrium. The first assumption must be experimentally verified, but it is very likely correct for low pressures ($\sim 1.0$ Torr). Rare-gas molecular ions are likely to be dominant only at rather high pressures ($\gtrsim 100$ Torr). The distance required for the average velocity of atomic ions to approach within 10% of the equilibrium drift velocity is derived for four idealized cases in the following paragraphs. The equilibration distance for the ion velocity is two-thirds of a mean free path for a constant field with a plane ionization source, 4.5 mean free paths for a constant field with a uniform source, 1.7 mean free paths for a linearly increasing field with a plane source, and 5.7 mean free paths for a linearly increasing field with a uniform source. The latter two cases provide a lower and upper bound for the fraction of the cathode fall where the ion velocity is less than

the equilibrium drift velocity. A normal rare-gas cathode fall has a thickness of approximately 50 to 100 mean free paths for symmetric charge exchange. The average ion velocity can be approximated as the equilibrium drift velocity throughout most all of the cathode fall.

The electric field in the normal and abnormal cathode fall is very definitely a function of position, but for the purpose of this initial discussion it will be assumed that the field is constant and is in the $z$ direction. The mobility at high $E/N$ of atomic ions in their parent gas is largely determined by symmetric charge exchange. Little momentum is transferred in these charge-exchange collisions. The symmetric charge-exchange-collision cross section is only weakly energy dependent. Wannier presented an elegant expression for the collision term of the Boltzmann equation in the approximation that (1) no momentum is transferred in the charge-exchange collision and (2) the cross section is independent of energy.[4] The Boltzmann equation including this collision term is

$$\frac{\partial f}{\partial t} + \frac{eE}{M}\frac{\partial f}{\partial v_z} + \mathbf{v}\cdot\nabla f$$
$$= -N\sigma v f + N\sigma\delta(\mathbf{v})\int\int\int f v\, dv_z dv_x dv_y + P(z)\delta(\mathbf{v}),$$

$$(1)$$

where $e$ is the electric charge, $M$ is the ion mass, $\sigma$ is the charge-exchange cross section, and other symbols have their usual meanings. The last term which involves $P(z)$ is a source term which represents the production of "new" ions via electron impact ionization. Consider, as case 1, a plane source at the origin. The source function $P(z)$ is therefore $j\delta(z)$ where $j$ is a constant. The time-independent nonequilibrium solution in which the ions start from rest at $z=0$ is

$$f_1 = j\delta(v_x)\delta(v_y)\{\exp(-\sigma Nz)s(v_z)\delta(v_z^2/2 - az)$$
$$+ (\sigma N/a)[s(v_z) - s(v_z - \sqrt{2az}\,)]$$
$$\times \exp[-v_z^2 N\sigma/(2a)]\},\qquad (2)$$

where $a$ is the ion acceleration $eE/M$, and $s(v_z)$ is the step function of $v_z$. This solution for large $z$ approaches

Wannier's equilibrium solution.[4] The distribution function given in Eq. (2) is not normalized in the usual sense because it is a nonequilibrium distribution. The integral

$$\int \int \int f_1 \mathbf{v} \, dv_z dv_x dv_y$$

is the particle flux density $j\hat{z}$, which must be independent of position by conservation of particles. The integral

$$\int \int \int f_1 dv_z dv_x dv_y$$

is the particle density which is dependent on position because the ions are accelerating. The average velocity of the ions in the $z$ direction is

$$\langle v_z \rangle = \frac{\int \int \int f_1 v_z dv_z dv_x dv_y}{\int \int \int f_1 dv_z dv_x dv_y}$$

$$= \frac{1}{\exp(-\sigma Nz)/\sqrt{2az} + \sqrt{\pi \sigma N/(2a)}\,\text{erf}(\sqrt{\sigma Nz}\,)} \, , \quad (3)$$

where $\text{erf}(x)$ is the error function.[5] The average velocity has the small-$z$ limit of $\sqrt{2az}$ which is expected from kinematics, and it has the large-$z$ limit of $\sqrt{2a/(\sigma N\pi)}$, in agreement with Wannier's equilibrium drift velocity. The

average velocity reaches 90% of the equilibrium drift velocity in a distance $0.65/(\sigma N)$, or about two-thirds of a mean free path. Higher moments of the distribution function also approach their equilibrium values in short distances, but not as quickly as the average velocity.

The distribution function of Eq. (2) has been presented by several authors in discussion of ions in the cathode fall.[6–9] The distribution function has previously been misidentified as an energy distribution function; probably because $\int f_1 M v_z dv_z$ is position independent. The distribution function of Eq. (2) is here identified as a solution to the Boltzmann equation and, thus, is a velocity distribution function. An integral expression which can be used to derive a velocity distribution function for an arbitrary position-dependent field with a plane ionization source is given in Ref. 8. Nonequilibrium double-humped distribution functions for $Ar^+$ ions in Ar have been observed in a low-pressure drift-chamber experiment.[10]

A solution of the Boltzmann equation for a constant field with an arbitrary source function $P(z)$ is constructed using the plane-source solution as a Green's function. The distribution function for constant field with an arbitrary $P(z)$ is

$$f = \delta(v_x)\delta(v_y) \int_{-\infty}^{z} P(z_0)[\exp[-\sigma N(z-z_0)]s(v_z)\delta(v_z^2/2 - a(z-z_0))$$

$$+ (\sigma N/a)\{s(v_z) - s[v_z - \sqrt{2a(z-z_0)}]\}\exp[-v_z^2 N\sigma/(2a)]]dz_0 \, . \quad (4)$$

Consider, as case 2, a uniform source for non-negative $z$. The source function $P(z_0)$ in Eq. (4) is replaced by $rs(z_0)$. The particle flux density

$$\int \int \int f_2 \mathbf{v} \, dv_z dv_x dv_z$$

is equal to $rz\hat{z}$; it grows linearly with distance from the origin. The average velocity of the ions in the $z$ direction is

$$\langle v_z \rangle = \frac{\int \int \int f_2 v_z dv_z dv_x dv_y}{\int \int \int f_2 dv_z dv_x dv_y} = \frac{z}{\sqrt{\pi/(2aN\sigma)}[\text{erf}(\sqrt{\sigma Nz}\,)(\sigma Nz + 1/2) + \sqrt{\sigma Nz/\pi}\exp(-\sigma Nz)]} \, . \quad (5)$$

The average velocity in case 2 approaches the equilibrium drift velocity of $\sqrt{2a/(\sigma N\pi)}$, but approaches more slowly than in case 1. The slower convergence is due to the production of new ions at rest via electron impact ionization at all $z \geq 0$. The distance required for the average ion velocity to reach 90% of the equilibrium drift velocity is 4.5 mean free paths in case 2.

Experimental studies of the electric field in the cathode fall indicate that the field increases with distance from the cathode-fall—negative-glow boundary. The field reaches a maximum at or near the cathode surface. The spatial dependence of the field has long been approximated as directly proportional to $z$, the distance from the cathode-fall—negative-glow boundary. Recent accurate electric

field measurements using optogalvanic detection of Rydberg atoms support this simple spatial dependence of the field.[11] The Boltzmann equation with a linearly increasing field is

$$\frac{\partial f}{\partial t} + kz\frac{\partial f}{\partial v_z} + \mathbf{v}\cdot\nabla f$$

$$= -N\sigma v f + N\sigma\delta(\mathbf{v})\int \int \int f v \, dv_z dv_x dv_y + P(z)\delta(\mathbf{v}) \, , \quad (6)$$

where $kz$ is the ion acceleration. The source function $P(z)$ for case 3 is a plane source $j\delta(z - z_0)$ where $z_0 > 0$. The distribution function for $z \geq z_0$ is

$$f_3 = j\delta(v_x)\delta(v_y)[\exp[-\sigma N(z-z_0)]s(v_z)2\delta(v_z^2 - kz^2 + kz_0^2) + (\sigma N/\sqrt{k})\{s(v_z) - s[v_z - (kz^2 - kz_0^2)^{1/2}]\}$$

$$\times \exp[\sigma Nz\{[1-v_z^2/(kz^2)]^{1/2} - 1\}]/(kz^2 - v_z^2)^{1/2}] \, . \quad (7)$$

This distribution function for large $z$ approaches Wannier's equilibrium distribution function[4]

$$f_{eq} = j\delta(v_x)\delta(v_y)[\sigma N/(kz)]s(v_z)\exp[-v_z^2\sigma N/(2kz)] \, . \quad (8)$$

We need to specify $z_0$ in order to compute an equilibration distance for the average velocity. If $z_0 \gg (\sigma N)^{-1}$, then the field changes only slightly in a mean free path and the equilibration distance will be that of the constant field problem. The interesting case is for $z_0$ near zero. The average velocity in the $z$ direction for this case is

$$\langle v_z \rangle = \frac{\int \int \int f_3 v_z dv_z dv_x dv_y}{\int \int \int f_3 dv_z dv_x dv_y} = \frac{1}{\exp(-\sigma Nz)/(\sqrt{k}z) + \pi \sigma N \exp(-\sigma Nz)[I_0(\sigma Nz) + L_0(\sigma Nz)]/(2\sqrt{k})}, \tag{9}$$

where $I_0(z)$ is a modified Bessel function of order 0 and $L_0(z)$ is a modified Struve function of order 0 as defined and tabulated in Refs. 12 and 13. The average velocity for this case reaches 90% of the equilibrium drift velocity $\sqrt{2kz}/(\pi \sigma N)$ in 1.7 mean free paths.

The plane-source distribution function for the linearly increasing field can be used as a Green's function to construct an ion distribution function for an arbitrary source function $P(z)$. The distribution function for a linearly increasing field with an arbitrary source function is

$$f = \delta(v_x)\delta(v_y) \int_0^z P(z_0)[\exp[-\sigma N(z-z_0)]s(v_z)2\delta(v_z^2 - kz^2 + kz_0^2) + (\sigma N/\sqrt{k})\{s(v_z) - s[v_z - (kz^2 - kz_0^2)^{1/2}]\}$$

$$\times \exp(\sigma Nz\{[1 - v_z^2/(kz^2)]^{1/2} - 1\})/(kz^2 - v_z^2)^{1/2}]dz_0 . \tag{10}$$

If the source function of the cathode fall is known, then it is possible to calculate a fairly realistic distribution function and equilibration distance for the ions. Unfortunately, it is the source function we are proposing to map from accurate field and gas density (temperature) measurements by assuming that the ions are equilibrated. This seems to suggest that the Boltzmann equation for ions, the Boltzmann equation for electrons, and Poisson's equation must be solved simultaneously. Fortunately, a simultaneous self-consistent solution of these three equations is not necessary. The source function $P(z)$ is a decreasing function of $z$ throughout the cathode fall. An electron avalanche starts from one electron emitted at the cathode and grows as $z$ decreases. Thus we can compute an upper limit for the equilibration distance of the ions in the cathode fall by using a uniform source function for positive $z$. This is case 4. The average ion velocity for a linearly increasing field with a uniform source of ions at all positive $z$ is

$$\langle v_z \rangle = \frac{\int \int \int f_4 v_z dv_z dv_x dv_y}{\int \int \int f_4 dv_z dv_x dv_y} = \frac{z}{\exp(-\sigma Nz)\pi\{I_0(\sigma Nz) + L_0(\sigma Nz) + \sigma Nz[I_1(\sigma Nz) + L_1(\sigma Nz) + 2/\pi]\}/(2\sqrt{k})} \tag{11}$$

where $I_1(z)$ and $L_1(z)$ are modified Bessel and modified Struve functions of order 1. The distance required for the average velocity to reach 90% of the equilibrium drift velocity $\sqrt{2kz}/(\pi \sigma N)$ is 5.7 mean free paths.

A normal rare-gas cathode fall is 50 to 100 mean free paths thick.[4,14] The ratio of 50 or 100 is independent of pressure because the product in Torr cm of pressure and thickness is constant for a normal cathode fall. The assertion that the ion velocity in a rare-gas cathode fall can be approximated by the equilibrium drift velocity is justified. The approximation fails within the first 6 mean free paths of the cathode-fall—negative-glow boundary. The approximation should be reliable for positions more than 6 mean free paths from the cathode-fall—negative-glow boundary. The collision term of the Boltzmann equation used in the preceding calculations is valid only for high field, but this should lead to an overestimate of the equilibration distance. Recent nonhydrodynamic calculations of electron kinetics suggest that the source function is fairly uniform near the cathode-fall—negative-glow boundary.[15]

It should be emphasized that the short equilibration distance is unique to the ions because of the symmetric charge exchange. The electrons in the cathode fall are not in hydrodynamic equilibrium. The nonequilibrium distribution of the electrons is a topic of high current interest for theoretical and experimental researchers.

[1] See, for example, B. M. Penetrante and J. N. Bardsley, Bull Am. Phys. Soc. **30**, 143 (1985); T. J. Moratz and L. C. Pitchford, ibid. **30**, 143 (1985); L. C. Pitchford and J. Ingold, ibid. **30**, 143 (1985).

[2] D. K. Doughty and J. E. Lawler, Appl. Phys. Lett. **45**, 611 (1984).

[3] D. K. Doughty, E. A. Den Hartog, and J. E. Lawler, Appl. Phys. Lett. **46**, 352 (1985).

[4] G. H. Wannier, Statistical Physics (Wiley, New York, 1966), p. 462.

[5] W. Gautschi, in Handbook of Mathematical Functions, edited by M. Abramowitz and I. A. Stegun (Dover, New York, 1964), pp. 295 and 310.

[6] W. D. Davies and T. A. Vanderslice, Phys. Rev. **131**, 219

(1963).

[7]Y. Chouan and D. Collobert, J. Phys. (Paris) **43**, 279 (1982).

[8]I. Abril, A. Gras-Marti, and A. Valles-Abarca, Phys. Rev. A **28**, 3677 (1983).

[9]I. Abril, A. Gras-Marti, and A. Valles-Abarca, J. Phys. D **17**, 1841 (1984).

[10]H. Mase, T. Tanabe, K. Taneko, and G. Miyamoto, J. Phys. D **12**, L123 (1979).

[11]D. K. Doughty, S. Salih, and J. E. Lawler, Phys. Lett. **103A**, 41 (1984).

[12]F. W. J. Olver, in *Handbook of Mathematical Functions*, edit-ed by M. Abramowitz and I. A. Stegun (Dover, New York, 1964), pp. 376 and 416.

[13]M. Abramowitz, in *Handbook of Mathematical Functions*, edited by M. Abramowitz and I. A. Stegun (Dover, New York, 1964), pp. 498 and 501.

[14]S. C. Brown, *Basic Data of Plasma Physics* (Wiley, New York, 1954), p. 281.

[15]P. Segur, M. Yousfi, J. P. Boeuf, E. Marode, A. J. Davies, and J. G. Evans, in *Electrical Breakdown and Discharges in Gases*, edited by E. E. Kunhardt and L. H. Luessen (Plenum, New York, 1983), Part A, p. 331.

APPENDIX C    (Pg. 28-48)

# Laser optogalvanic and fluorescence studies of the cathode region of a glow discharge

E. A. Den Hartog, D. A. Doughty, and J. E. Lawler

*Department of Physics, University of Wisconsin, Madison, Wisconsin 53706*

(Received 15 December 1987; revised manuscript received 4 April 1988)

Various laser diagnostics are used to study the cathode-fall and negative-glow regions of a He glow discharge with a cold Al cathode. The electric field and absolute metastable densities are mapped and the gas temperature is measured over a range of current densities from a near-normal (173 V) to a highly abnormal (600 V) cathode fall. These measurements are analyzed to yield the current balance at the cathode surface, the ionization rate in the cathode-fall region, and the meta-stable production rate in the cathode-fall and negative-glow regions. The experimental results compare favorably with the results of Monte Carlo simulations. The density and temperature of the low-energy electron gas in the negative glow is determined by combining information from the experiments and Monte Carlo simulations.

## I. INTRODUCTION

There has in recent years been a very substantial effort toward the development of a quantitative microscopic understanding of the cathode region of glow discharges.[1-6] This region is of great practical interest because of its importance in plasma processing and in pulsed power devices. Plasma processing includes applications of glow discharges in ion etching, thin-film deposition, and plasma treating of surfaces. The stability of pulsed gas discharge lasers and other pulsed power devices is largely determined by the stability of the cathode-fall region.

The cathode region is also of great fundamental interest. The hydrodynamic approximation, which is often very useful in the central region of a discharge, fails in the cathode region. If the local $E/N$ (electric field to gas density ratio) determines the velocity dependence of the electron distribution function, then the electrons are in hydrodynamic equilibrium.[7] The lack of hydrodynamic equilibrium in the cathode-fall region is caused by the large and rapidly changing $E/N$, and by the proximity of the electrode. The cathode region includes both the cathode-fall and negative-glow regions. The negative glow has a high density of low-energy electrons and very small electric fields. It also is a nonhydrodynamic region because of a low density of high-energy "beam" electrons injected from the cathode-fall region. Unfortunately the extensive data base of electron transport coefficients such as drift velocities, diffusion coefficients, and Townsend coefficients is not directly applicable in modeling the cathode region.[8] These coefficients are generally measured in drift tube experiments in which considerable effort is devoted to ensuring that the hydrodynamic approximation holds.

Nonequilibrium regions are receiving increased attention from theorist and experimentalist.[9-12] Because of their nonequilibrium nature, electrons in the cathode-fall region are often modeled using either a full Boltzmann equation analysis or a Monte Carlo simulation. A somewhat less realistic but much faster approach is based on a model distribution function with position-dependent parameters.[13] The spatial dependences of the parameters such as electron density, average velocity, and average energy, are determined by solving moments of the Boltzmann equation which are coupled ordinary differential equations. These approaches might in general be called nonequilibrium fluid models. Single-beam and multiple-beam models are examples of this general approach.[14,15] This approach is attractive because it is usually easier and faster to solve moments of the Boltzmann equation which are coupled ordinary differential equations than it is to solve the full Boltzmann equation which is a partial differentio-integral equation. The nonequilibrium fluid approach can in principle be made quite realistic if one is sufficiently clever in the design of a model distribution function for the electrons.

A more complete solution will require a calculation of self-consistent space-charge electric fields. This will involve coupling Poisson's equation and one (or more) moment equation(s) for ions to the moment equations for electrons. Consider a model which includes three moments of the Boltzmann equation for electrons, Poisson's equation, and a single continuity equation for ions. This model requires the simultaneous solution of five coupled first-order differential equations. Four natural boundary conditions include specifying the electron distribution function at the cathode and specifying an electron emission coefficient for ion bombardment of the cathode. The "missing" condition is unfortunately not a boundary condition but rather an extremum condition. The physically correct solution will maximize the current at fixed voltage or minimize the voltage at fixed current.

The problem described in the preceding paragraph is obviously quite difficult. It is also incomplete because of the important role played by metastable atoms, and uv or vacuum ultraviolet (vuv) photons in releasing electrons from the cathode. Appropriate balance equations for these neutral particles must also be included in the problem.

A complete solution to the cathode-fall problem is beyond the scope of this paper. This paper describes ex-

tensive experimental results from recently developed laser optogalvanic diagnostics, and more traditional laser-induced fluorescence and laser absorption diagnostics.[16] These experimental results include electric field maps, gas temperature (density) measurements, and absolute metastable density maps in a He glow discharge over a range of current densities from a near-normal cathode fall of 173 V to a highly abnormal cathode fall of 600 V. These experimental results are analyzed in detail to provide information on electron-impact ionization and excitation in the cathode-fall and negative-glow regions. Monte Carlo simulations of electron avalanches in the cathode region are compared to the experimental results. The Monte Carlo code is based on the Boeuf-Marode variation of the null collision technique for nonuniform fields.[17] The agreement of the Monte Carlo results and the experimentally derived ionization and excitation rates is generally good. Finally, the experimental results are combined with Monte Carlo simulations to infer the density and temperature of the low-energy electron gas in the negative glow. This unexpected information is largely based on observation of a suppression of the $2\,^1S$ metastable density in the negative glow due to metastable spin conversion by low-energy electron collisions.

The results of this paper can be viewed in several ways: (1) as a test of our understanding of the key physical processes in the cathode region, (2) as a set of benchmark experiments for further modeling of the cathode region, or (3) as a starting point for more ambitious experiments to study electron emission from the cathode. We plan to make in situ determinations of the relative importance of, and coefficients for, electron emission due to ion, metasta-

ble atom, and uv or vuv photon bombardment of the cathode.

The structure of this paper is as follows. Section II is a description of the experimental apparatus. Sections III and IV are, respectively, a presentation of the electric field and gas density measurements, and an analysis of this data to yield information on ionization in the cathode-fall region. The field maps and gas density measurements are combined with an analytic treatment of ion transport in the cathode-fall region to determine the current balance, or ratio of ion to electron current at the surface of the cathode. This ratio is found to be 3.3 and is independent of the total discharge current. Sections V and VI are respectively, a presentation of the metastable density maps and an analysis of metastable diffusion and kinetics in the cathode-fall and negative-glow regions. The analysis of the data yields $2\,^1S$ and $2\,^3S$ metastable production rates and a rate for $2\,^1S$ metastable quenching due to low-energy electron collisions in the negative glow. Sections VII and VIII are, respectively, a discussion of the Monte Carlo code including electron-impact cross sections and a comparison of the Monte Carlo results with the experimental results. Section IX is an analysis of the density and temperature of the low-energy electrons in the negative glow. Finally, Sec. X includes a summary, some conclusions, as well as speculations on future work.

## II. EXPERIMENTAL APPARATUS

Figure 1 is a schematic of the experimental apparatus. The discharge used in these studies is produced between
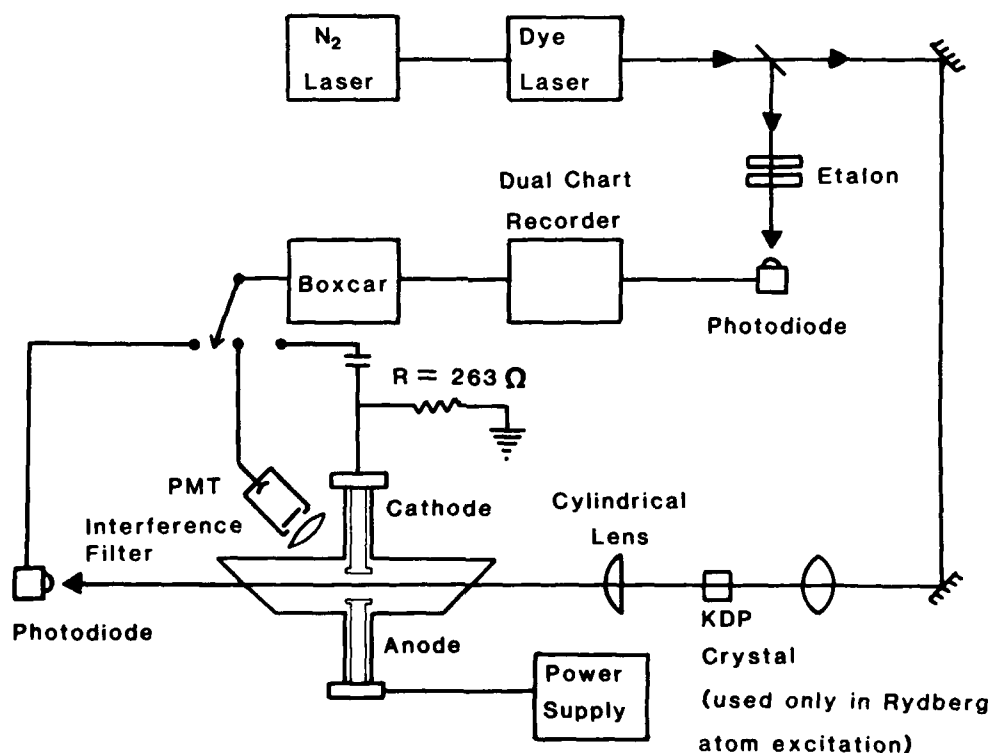


FIG. 1. Schematic of the experimental apparatus showing all three detection methods: optogalvanic, fluorescence, and absorption detection.

LASER OPTOGALVANIC AND FLUORESCENCE STUDIES OF . . .

flat circular Al electrodes 3.2 cm in diameter and separated by 0.62 cm. The electrodes are water cooled to minimize gas heating. The discharge tube is made primarily of glass and stainless steel. Most of the large seals are made with knife edge flanges on Cu gaskets. The only exceptions are the high-vacuum epoxy seals around the fused silica brewster windows. A liquid-$N_2$ trapped diffusion pump evacuates the tube to $2 \times 10^{-8}$ Torr. When no liquid $N_2$ is in the trap an ion pump maintains the vacuum to prevent oil from backdiffusing into the system. The leak rate into the sealed discharge tube is approximately $3 \times 10^{-4}$ Torr/day. For discharge operation ultrahigh-purity (0.999 999) He is slowly flowed through the system. A capacitive manometer monitors the pressure which is maintained at 3.5 Torr. The He first passes through a cataphoresis discharge to remove any residual contaminants before entering the main discharge tube. Emission spectra reveal only weak Al and H impurity lines. Although He is much less effective at sputtering than heavy inert gases, some sputtering of the Al cathode does occur. We suspect that the slow erosion of the cathode gives rise to both the weak Al and H impurity lines. Many metals absorb hydrogen. The surface of the Al cathode is cleaned *in situ* by running an Ar discharge. Argon is very effective at sputtering most metals including Al. A carefully prepared cathode provides discharge *V-I* characteristics which are stable to a few percent over a period of a month.

Experiments are carried out over a range of discharge current densities from 0.190 to 1.50 mA/cm$^2$. The low current density corresponds to a near-normal cathode-fall voltage of 173 V and the high current density corresponds to a highly abnormal cathode-fall voltage of 600 V. The discharge current is spread uniformly across the surface of the electrodes. The absence of significant fringing was verified by segmenting the 3.2-cm-diam cathode into a 1.6-cm-diam disk and a close-fitting annulus with an outside diameter of 3.2 cm. Each part of the cathode was maintained at the same potential during operation and the average current density on each was measured. The current density was found to be uniform across the cathode. This measurement is one of the justifications for using one-dimensional models of the cathode-fall region. The segmented cathode was replaced by a solid cathode after the current-density measurements.

The laser used is a $N_2$ laser pumped dye laser. Several different configurations for the dye laser are used, depending on the specific experiment. The dye laser bandwidth is 0.3 cm$^{-1}$ without an étalon. An étalon is used to reduce the bandwidth to 0.01 cm$^{-1}$ (300 MHz) for some measurements. The dye laser with frequency doubling is tunable over a wavelength range 200–700 nm.

Figure 1 shows all three detection schemes used in these experiments. Optogalvanic detection, fluorescence detection, and absorption detection each has unique advantages which are discussed in subsequent sections. In order to perform spatially resolved measurements without disturbing laser alignment the discharge is mounted on a precision translation stage. Good spatial resolution is achieved, when necessary, by passing the laser beam through a narrow slit and imaging the slit into the discharge region.

## III. ELECTRIC FIELD AND GAS DENSITY MEASUREMENTS

Space-charge electric fields in gas discharges have traditionally been measured using electron beam deflection. A laser-induced fluorescence technique for field measurements was recently developed by Moore, Davis, and Gottscho.[18] A laser technique based on optogalvanic detection of Rydberg atoms was recently developed by Doughty, Salih, and Lawler.[16,19] Both laser techniques have a number of important advantages over the traditional electron beam deflection technique.[20] The laser techniques are useful at higher pressures and discharge current densities. It is easier to use a spectroscopic technique in a high-purity discharge system. The laser techniques are truly nonperturbing when performed with a nanosecond pulsed laser because the field is measured when the atoms or molecules absorb the laser light, and any perturbation to the discharge fields occurs on a longer-time scale. Lasers have the potential for making measurements with a few microns spatial resolution and nanosecond temporal resolution. The technique based on Rydberg atoms has broad applicability because all atoms and molecules have Rydberg levels. This technique also has a wide dynamic range because one can choose an appropriate principal quantum number. The Rydberg atom technique has been used to measure fields as small as $10 \pm 1$ V/cm.[21]

The technique based on optogalvanic detection of Rydberg atoms excited with a single laser is used in this investigation.[16] A technique involving intersecting laser beams for pinpoint field measurements has also been demonstrated.[19] The discharge studied in this experiment is sufficiently one dimensional that the simpler single laser technique is adequate. In addition to the advantages described in the preceding paragraph, a Rydberg atom technique offers an advantage in ease of interpretation. The experimental Stark spectra are analyzed by comparing to theoretical Stark maps. Straightforward, *ab initio* calculations of these Stark maps to 1% accuracy are possible for many atoms. An excellent procedure for calculating the Stark maps is described in detail by Zimmerman, Littman, Kash, and Kleppner.[22] The procedure used in this work is a simplified version of that described by Zimmerman *et al.* The main simplification is that we use corrected hydrogenic radial matrix elements instead of performing a numerical integration for radial matrix elements.

A Rydberg atom is an atom with one of its electrons excited to a high-lying energy level characterized by a large principal quantum number $n$. As $n$ increases, many atomic properties tend towards those of hydrogen. The energy of Rydberg states is given by the empirical formula,

$$W_{nl} = W_{ion} - \frac{R_0}{(n - \delta_l)^2} , \tag{1}$$

where $W_{\text{ion}}$ is the ionization potential, $R_0$ is the Rydberg constant, $l$ is the angular momentum quantum number, and $\delta_l$ is the quantum defect. This expression describes hydrogenic energy levels for $\delta_l = 0$. The quantum defect reflects the degree of interaction of the outer valence electron with the core electrons.

Mixing of states with different principal quantum numbers occurs if both the field and principal quantum number are sufficiently large. This is an undesirable complication if one is studying a discharge and simply using Rydberg atoms as a probe. It can usually be avoided by choosing an appropriate, somewhat lower principal number for very high fields. In heavy atoms with large quantum defects it may be necessary to include states, which are nearby at zero field, but have different principal quantum numbers. In He all quantum defects are less than 0.5.

The energy perturbations are calculated by diagonalizing an $(n-m)$ by $(n-m)$ Hamiltonian matrix, where $m$ is the component of angular momentum along the field axis. The basis set is made of eigenfunctions of the unperturbed Hamiltonian. The diagonal matrix elements are the unperturbed energies of the levels as given in Eq. (1). The quantum defect $\delta_l$ can be deduced from Moore's tables of energy levels.[23] The off-diagonal elements vanish except those connecting states for which $l$ differs by 1. These matrix elements are approximately the hydrogenic matrix elements given by the expression

$$\langle n \ l \ m \mid e\mathbf{E}\cdot\mathbf{r} \mid n \ l-1 \ m \rangle$$

$$= (\tfrac{3}{2})eEa_0 n \left| \frac{(n^2-l^2)(l^2-m^2)}{4l^2-1} \right|^{1/2} . \quad (2)$$

where $e$ is the unit charge and $a_0$ is the Bohr radius. The

dipole matrix elements above must be corrected to account for core penetration effects. A correction factor of order 1 has been tabulated as a function of quantum defect by Edmonds et al.[24]

Figure 2 presents the results of applying the procedure outlined above to the $n=11$, $m=0$, singlet levels of He. The diagonal elements are determined from the splittings of the $11\,^1S$, $11\,^1P$, $11\,^1D$, $11\,^1F$, and $11\,^1G$ levels, whereas the $H$, $I$, $K$, $L$, $M$, and $N$ levels are approximated as being degenerate with the $11\,^1G$ level.[23] A 5% correction is applied to the $S$-$P$ matrix elements to account for core penetration.[24] Corrections to the other elements are generally less than 1%. Figure 2(a) is a plot of the energies of the $m=0$ states for the $n=11$ levels as a function of applied electric field. The energies are the eigenvalues of the diagonalized Hamiltonian. Only ten components appear in this figure since the $11\,^1S$ level has a large quantum defect and is 23 cm$^{-1}$ below this pattern. This level does not mix strongly with the other $n=11$ levels at the fields indicated in the figure. For fields above 200 V/cm the pattern clearly reflects a linear Stark effect.

Figure 2(b) is a plot of the expected intensity of selected Stark components from Fig. 2(a) as a function of electric field. Suppose transitions between a low-lying non-Rydberg $^1S$ level and the $n=11$ Rydberg states are driven. With no external electric field, only the $^1S \rightarrow 11\,^1P$ transition will be observed. The effect of the field is to mix a fraction of the $11\,^1P$ state into each $n=11$ state. This fraction is determined by squaring the appropriate element from an eigenvector of the diagonalized Hamiltonian. The fraction is a relative linestrength for a transition to that component of the Stark manifold. The relative linestrengths of the components labeled 1, 3, and 8 are plotted in Fig. 2(b). Such information is useful
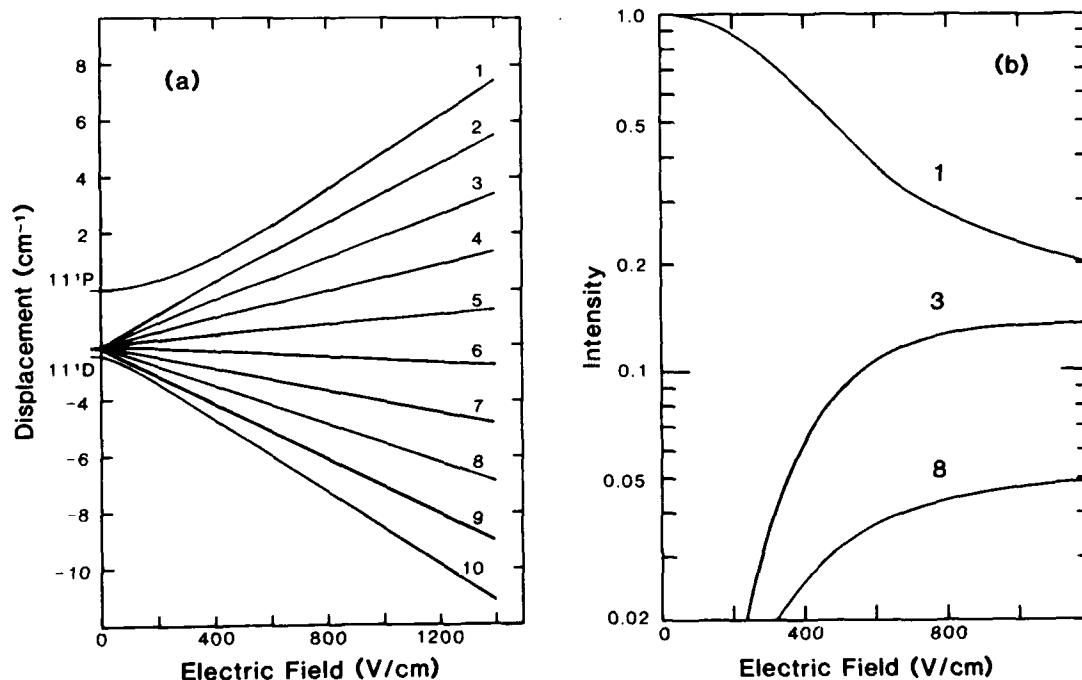


FIG. 2. (a) Theoretical Stark map for the $n=11$ singlet $m=0$ levels of He. (b) Theoretical intensities of selected Stark components as a function of electric field.

in determining electric fields in the case where the splittings between individual components are small.

The narrow bandwidth, high power dye laser is ideal for exciting atoms from a well-populated lower level to a specific Rydberg level. Since the oscillator strength decreases as $1/n^3$ it is very difficult to directly detect the weak absorption. Laser-induced fluorescence from these atoms is also difficult to detect, because in the 1–10 Torr pressure regime the Rydberg atoms do not survive long enough to radiate. They are collisionally ionized via collisions with ground-state atoms. Associative ionization,

$$\text{He}^{*}(nl > 3s) + \text{He}(1\ ^1S_0) \rightarrow \text{He}_2^{-} + e^{-} ,\qquad (3)$$
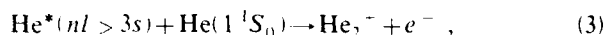
is likely important for Rydberg levels below the ionization limit by more than thermal energies. The absorption of laser radiation produces excess ionization in the discharge and thus produces an optogalvanic effect. An optogalvanic effect is detectable as a perturbation of the discharge current and can in general be either positive (increased current) or negative. Absorption of radiation may in some cases cause a reduction of ionization in the discharge and a decrease in discharge current.[25] Optogalvanic spectroscopy is uniquely suited to the detection of Rydberg atoms in a discharge environment.

The cathode-fall region is particularly well suited to optogalvanic detection. If an extra ion-electron pair is introduced into the cathode-fall region the electron is accelerated by the field, thus producing additional ionization. This amplification can result in optogalvanic effects in the cathode-fall region that are 100 times more sensitive than optogalvanic effects in the positive column.[26]

If the lower level from which the transition is driven is metastable, the ionization process results in the destruction of the metastable atom. The destruction of atoms in these levels can produce a negative optogalvanic effect since metastables diffusing to the cathode have a large probability of releasing electrons from the cathode. It would seem that this negative optogalvanic effect might cancel the positive optogalvanic effect which is due to the extra electron produced by associative ionization. The time scales for the two signals, however, are vastly different. The diffusion time of the metastables to the cathode can be several hundred microseconds, whereas associative ionization produces a signal in less than 1 $\mu$sec. When produced by a pulsed laser the positive portion of the transient optogalvanic signal is well isolated and can be easily monitored with a boxcar averager.

The critical consideration in measuring discharge electric fields is choosing an appropriate transition to produce the Rydberg atoms. For noble gases in general and He in particular, transitions from the ground state to upper levels are inaccessible with present dye lasers. These gases, however, have metastable levels which are well populated in the discharge. In He, both $2\ ^1S$ and $2\ ^3S$ levels are metastable. The $2\ ^1S$ to $11\ ^1P$ transition at 321 nm is the most suitable under the conditions of this experiment. Although the $2\ ^3S$ level has a higher population than the $2\ ^1S$, the $n\ ^3P$ levels have a much higher quantum defect than the $n\ ^1P$'s (0.068 and −0.012, respectively).[23] The larger quantum defect necessitates exciting to a level with a larger $n$ to observe a linear Stark

effect for a given field. The oscillator strength goes as $1/n^3$ while the number of components increases as $n$, so the amount of signal in each component drops as $1/n^4$.

Radiation from the dye laser is frequency doubled using a potassium dihydrogen phosphate crystal. The frequency doubled beam is polarized normal to the surface of the cathode so that only $\Delta m = 0$ transitions are excited. This results in only $m = 0$ Rydberg states because the lower level is a $^1S$. The beam is focused in the center of the discharge to a strip approximately 0.01 cm wide and 1 cm long parallel to the surface of the electrodes. As the laser is scanned through the Stark manifold, the current is monitored across a 263 $\Omega$ resistor between the cathode and ground. The optogalvanic signal is processed using a boxcar averager, the output of which is plotted on one channel of a two-channel chart recorder. Figure 3 includes representative Stark spectra for a range of distances from the cathode. The splittings of adjacent components or the width of the entire Stark manifold are compared to the Stark map of Fig. 2(a) to determine the local electric field. A relative frequency calibration is obtained by use of an etalon with an accurately determined spacer. Interference fringes are generated and recorded simultaneously with the spectrum.
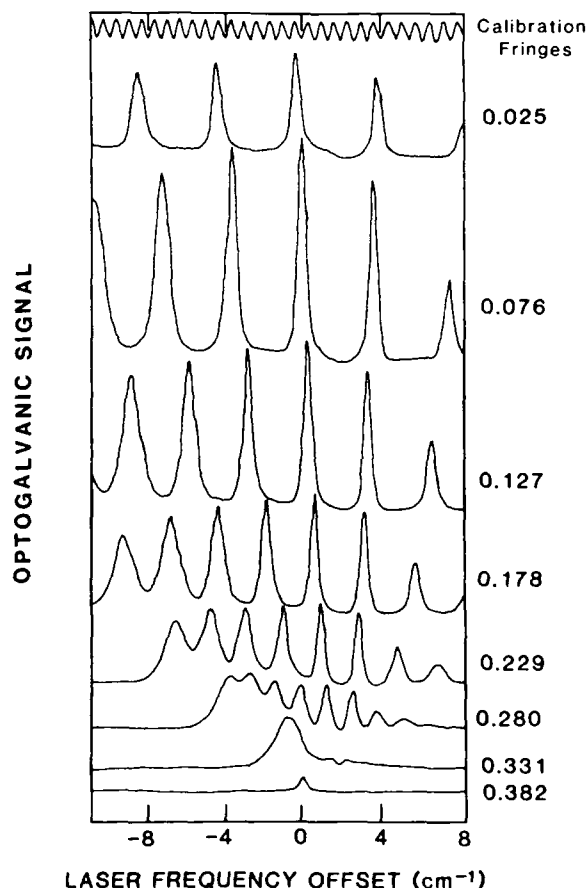


FIG. 3. Optogalvanic Stark spectra in the 3.50-Torr He discharge operating at 1.50 mA/cm². The distance from the cathode in centimeters at which each spectra is taken is indicated at the right.

The relative linestrength of Stark components or groups of components is also useful in field measurements.[16] This approach works best at low fields where the linestrengths are strongly dependent on field as indicated in Fig. 2(b). The relative linestrengths are equal at high field. In order to determine an electric field from relative linestrengths one must (1) avoid saturation of experimental spectra and (2) establish that the optogalvanic effect is equally efficient on all components. This second condition can be argued on fairly general grounds. Collisions with ground-state atoms rapidly mix the populations of the zero-field $n=11$ levels. The cross section for $l$ mixing of $n=11$ Na atoms by collision with ground-state He atoms is $1.85 \times 10^3$ Å$^2$.[27] It is reasonable to assume that an $n=11$ He atom behaves similarly to an $n=11$ Na atom, thus the $l$ mixing rate of approximately $4 \times 10^9$ sec$^{-1}$ at 3.5 Torr is expected. This mixing rate completely overwhelms radiative decay from the $11\,^1P$ level at a vacuum rate of $1.4 \times 10^7$ sec$^{-1}$.[28] Radiation trapping further strengthens the argument by lowering the effective radiative decay rate. A comparison of relative linestrengths must be based on integrated linestrengths because the spectral widths of the Stark components vary across the manifold. The outer components are broadened by the local electric field gradient. The laser probes some finite volume containing a range of field magnitudes. The spectral position of the outer components is most dependent on the field, and hence their widths is proportional to the field gradient and the volume probed by the laser.

The results of field measurements as a function of position made at five different current densities in 3.5 Torr of He are plotted in Fig. 4. These measurements are based on the splittings of adjacent components and the width of the Stark manifold. The solid lines are linear-least-square fits to the data. The linear decrease in field magnitude with distance from the cathode is in agreement with the

classic picture of the cathode-fall region. Close inspection reveals only a very slight negative curvature. This linear behavior persists to quite small fields near the cathode-fall–negative-glow boundary where the field extrapolates to zero. Direct measurements to rather low fields have been reported by Ganguly et al.[29] The position of the boundary between the cathode-fall and negative-glow regions can also be confirmed by a qualitative and quantitative change in optogalvanic effects. The excellent agreement between the voltage measured using a digital voltmeter and the voltage determined by integrating the electric field across the cathode-fall region indicates that the field measurements are on average accurate to 1%.

It is essential to determine both the electric field and the $E/N$ throughout the cathode-fall region. We found that significant gas heating and a corresponding gas density reduction occurs in the abnormal cathode-fall region, even with the water-cooled electrodes in our experiment. Ions carry most of the current in the cathode-fall region. The motion of atomic or molecular ions in their parent gas (i.e., He$^+$ in He or N$_2^+$ in N$_2$) is limited by symmetric charge exchange

$$\text{He}^+(\text{fast}) + \text{He}(\text{slow}) \rightarrow \text{He}(\text{fast}) + \text{He}^+(\text{slow}) \,. \qquad (4)$$
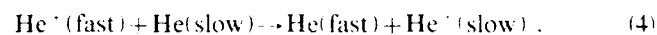
This reaction has a large resonant cross section which is only weakly dependent on energy. It results in a short equilibration distance for ions as discussed in Sec. IV, and a very efficient conversion of electrical energy to heavy-particle translational motion and to heat. Examination of the typical $Nd_c$ products (gas density times cathode-fall thickness) suggests that many of the energetic neutrals scatter before reaching the cathode.

To complement the field measurements in Fig. 4, the gas temperature is measured in the cathode-fall region for each of the five current densities of the study. The tem-
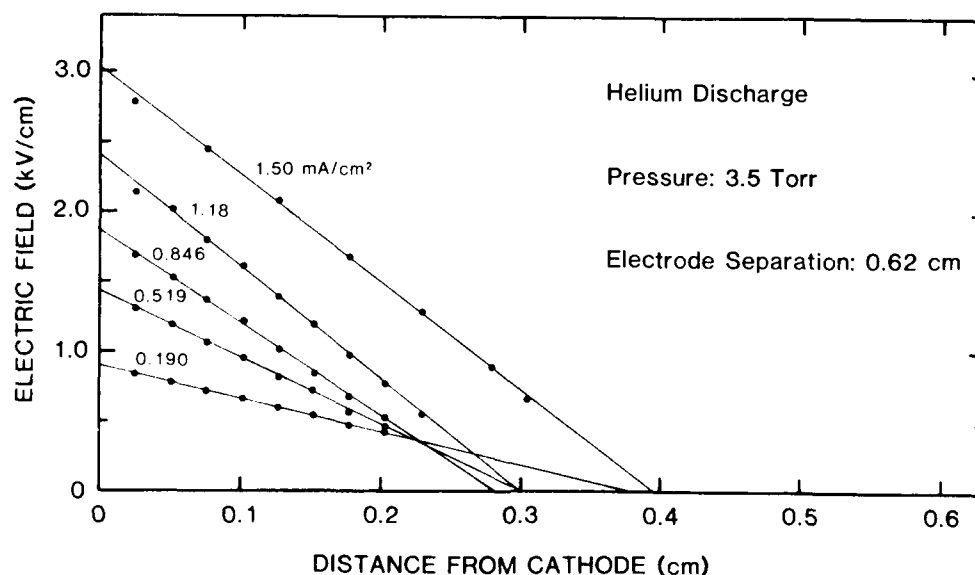


FIG. 4. Electric field as a function of distance from the cathode for five current densities, all at 3.50 Torr. The lines are linear-least-squares fits to the data. The anode corresponds to the right-hand side of the figure.

perature is found to be constant within an error bar throughout the cathode-fall region.

Doppler profiles are obtained by scanning a nonsaturating pulsed dye laser through the transition of interest and detecting the resulting optogalvanic signal with a boxcar averager. The beam was focused to a width of 0.06 cm within the cathode-fall region. The transition is the $2\,^1S$ to $3\,^1P$ transition of He at 501.6 nm. The dye laser bandwidth is reduced to 300 MHz by introducing an etalon. Other contributions to the observed line shape include a natural width of 92 MHz,[28] pressure broadening at 3.5 Torr of 146 MHz,[30] and Stark broadening on the order of 100 MHz. These contributions are small compared to the Doppler width of 3.66 GHz at 293 K.

The temperature was determined by measuring the full width at half maximum intensity of the line profile. Since the temperature increase is proportional to the power dissipated in the discharge and the Doppler width is proportional to the square root of the temperature, the square of the measured width was plotted as a function of discharge power. If the broadening mechanisms, apart from Doppler broadening, are negligible, the resulting extrapolation should indicate a zero-power Doppler width which corresponds to ambient gas temperature. The difference between the width calculated at ambient temperature and that indicated by the zero-power extrapolation gives the residual width, which was then subtracted from the measured widths. This correction is less than the size of the error bar. The temperature at each current density was then determined from the width.

Figure 5 is the resulting experimentally derived gas density as a function of discharge power measured at a constant pressure of 3.50 Torr. At the highest power studied, the density is 30% lower than what would be expected assuming ambient temperature. Each data point is determined from ten Doppler width measurements. These density measurements are combined with the field measurements of Fig. 4 to derive important parameters of the cathode-fall region in Sec. IV of this paper.

## IV. CURRENT BALANCE AT THE CATHODE SURFACE

The current balance at the surface of the cathode is the ratio of the ion current to electron current, which is determined from measurements of the electric field and gas density in the cathode-fall region and the total discharge current density $J_D$. The ion current density at the cathode, $J^0_+$, is the product of the ion charge density $\rho_+$ and the average ion velocity at the cathode surface, $\langle v_z \rangle^0$. Poisson's equation determines the space-energy density in the cathode-fall region from the spatial gradient of the electric field. High fields in the cathode-fall region result in very high electron velocities and a negligible electron density; the space charge is almost entirely due to the ions.

Ion motion in the cathode-fall region is limited by the symmetric charge exchange reaction of Eq. (4). The cold gas or high-field approximation is applicable throughout
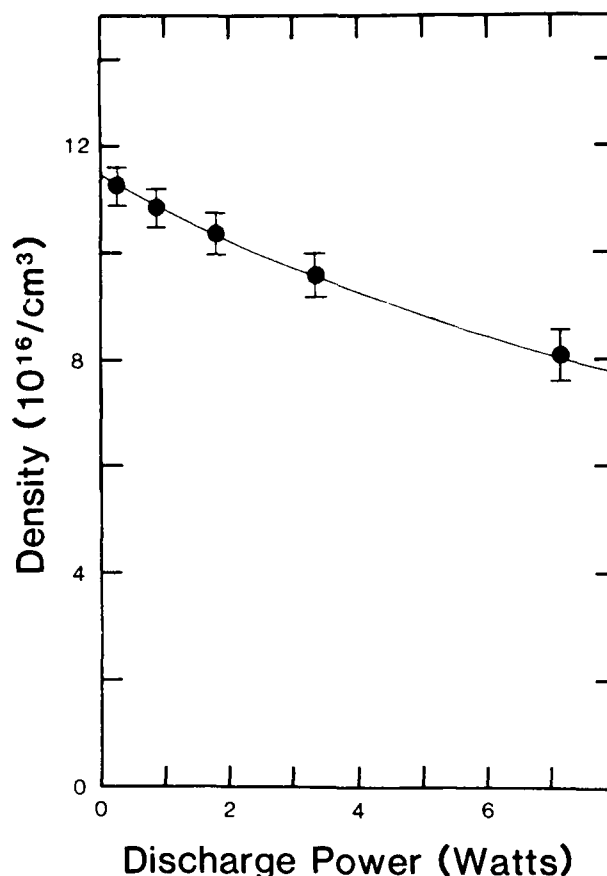


FIG. 5. Experimentally derived gas density as a function of discharge power measured at a constant pressure of 3.50 Torr.

most of the cathode-fall region. In this approximation the ion is assumed to start from rest after each charge exchange. It is thus reasonable to argue that the equilibration distance of the ions should be comparable to the mean free path for symmetric charge exchange. Each charge exchange collision wipes out all memory of the ion's history. Although the above argument is appealing, two aspects of the cathode-fall region complicate the picture. There is a significant field gradient, and new ions are produced throughout the cathode-fall region by electron-impact ionization.

These complications have both been included in an analytic treatment of ion transport in the cathode-fall region.[31] These solutions to the Boltzmann equation for ions will be summarized here. It is convenient to reverse coordinate systems when discussing ions. In most of this paper, parameters are measured and plotted as a function of distance from the cathode. For this discussion of ion transport we choose an origin at the boundary between the cathode-fall and negative-glow regions, and we let the positive z axis point toward the cathode. This temporary change in coordinate systems makes the field, ion velocity, and ion flux density positive. The time-independent Boltzmann equation is

$$\frac{eE}{m_-}\frac{\partial f}{\partial v_z}+\mathbf{v}\cdot\nabla f$$

$$=N\sigma vf+N\sigma\delta(\mathbf{v})\iiint f v\,dv_z dv_x dv_y$$

$$+P(z)\delta(\mathbf{v})\,,\tag{5}$$

where $e$ is a unit charge, $m_-$ is the ion mass, $\sigma$ is the charge exchange cross section, and $P(z)$ is the electron-impact ionization rate per unit volume. The charge exchange cross section, although weakly energy dependent, is here approximated as independent of energy. The first and second terms on the right-hand side of Eq. (5) are Wannier's elegant expression for the collision term due to symmetric charge exchange.[32] The third term is a source term due to electron-impact ionization. This source term and the electric field should come from a self-consistent description of the cathode-fall region which is beyond the

scope of this work. We therefore use a field which increases linearly with distance from the cathode-fall–negative-glow boundary and replace the ion acceleration $eE/m_-$ by $kz$. The electron-impact ionization rate per unit volume, $P(z)$, is known to peak near the cathode-fall–negative-glow boundary from Monte Carlo simulations by Beouf and Marode, and others.[17] Section VII of this paper describes a determination of $P(z)$ from Monte Carlo simulation of electron avalanches in the cathode region. A lower limit for the equilibration distance is calculated by assuming that $P(z)$ describes a plane source at the cathode-fall–negative-glow boundary. An upper limit for the equilibration distance is calculated by assuming $P(z)$ describes a uniform source for positive $z$. Both limits are derived from the solution to the problem where $P(z)$ is a plane source $j\delta(z-z_0)$ and where $z_0 > 0$. The distribution function at any positive $z$ for this source is

$$f_G=j\delta(v_x)\delta(v_y)s(v_z)\{(\exp[-\sigma N(z-z_0)])2\delta(v_z^2-kz^2+kz_0^2)$$

$$+(\sigma N/\sqrt{k})[1-s(v_z^2-kz^2+kz_0^2)]\exp\}\sigma Nz[(1-v_z^2/kz^2)^{1/2}-1]\}/(kz^2-v_z^2)^{1/2})\,.\tag{6}$$

where $s(v_z)$ represents a step function. The integral $\iiint f_G v\,dv_z dv_x dv_y$ is the ion flux density $j\hat{z}$ for all $z$ greater than $z_0$. The flux density must be independent of position by conservation of particles. The integral

$$\iiint f_G\,dv_z dv_x dv_y$$

is the ion density which is dependent on position because the ions are accelerating. The distribution function of Eq. (6) for large $z$ approaches Wannier's equilibrium distribution function[32]

$$f_{eq}=j\delta(v_x)\delta(v_y)(\sigma N/kz)s(v_z)\exp(-v_z^2\sigma N/2kz)\,.\tag{7}$$

The lower limit for the equilibration distance of ions in the cathode-fall region is determined by letting $z_0$ approach zero. This limit corresponds to a plane source of ionization at the cathode-fall–negative-glow boundary. The average velocity in the $z$ direction for the case where $z_0$ approaches zero is

$$\langle v_z\rangle=\frac{\iiint f_G v_z dv_z dv_x dv_y}{\iiint f_G dv_z dv_x dv_y}=\frac{1}{\exp(-\sigma Nz)/\sqrt{k}z+\pi\sigma N\exp(-\sigma Nz)[I_0(\sigma Nz)+L_0(\sigma Nz)]/2\sqrt{k}}\,,\tag{8}$$

where $I_0(z)$ is a modified Bessel function of order 0 and $L_0(z)$ is a modified Struve function of order 0 as defined and tabulated in Abramowitz and Stegun.[33,34] The average velocity for this case reaches 90% of the equilibrium drift velocity $\sqrt{2kz/\pi\sigma N}$ in 1.7 mean free paths. If $z_0 >> (\sigma N)^{-1}$ then the field changes only slightly in a mean free path and the equilibration distance will be that of the constant field problem, $0.65/\sigma N$, or two-thirds of a mean free path.[31]

The flux density, average velocity, and ion density are plotted in Fig. 6 for the distribution function of Eq. (6) with $z_0 \sim 0$. The flux density, plotted in Fig. 6(a), must be independent of $z$ because the source is localized at $z_0$ near the origin and the system is in steady state. The average velocity, plotted in Fig. 6(b), is a steadily increasing function of $z$ because the field increases linearly with $z$. Figure 6(c), which is a plot of the ratio of the average veloci-

ty to the local equilibrium drift velocity $\sqrt{2kz/\pi\sigma N}$, clearly shows that the nonhydrodynamic behavior is confined to within a few mean free paths of the source near the origin. The equilibration distance of 1.7 mean free paths required for the average velocity to reach 90% of the local equilibrium drift velocity is read directly from Fig. 6(c). A low average velocity near the origin implies a large ion density because their product is the constant flux density. The ion density is plotted in Fig. 6(d).

Equation (6) for $f_G$ is very slightly different from $f_3$ as defined in Eq. (7) of Ref. 31. The changes make $f_G$ defined (zero) for positive $z$ less than $z_0$. Thus $f_G$ corresponds more closely to Arfken's definition of a one-dimensional Green's function.[35] The distribution function at any positive $z$ for a linearly increasing field with arbitrary $P(z)$ is

$$f = \delta(v_x)\delta(v_y)s(v_z)$$

$$\cdot \int_0^\infty P(z_0)\{\exp[-\sigma N(z - z_0)]2\delta(v_z^2 + kz^2 - kz_0^2)$$

$$+ (\sigma N/\sqrt{k})[1 - s(v_z^2 - kz^2 + kz_0^2)]\exp\{\sigma Nz[(1 - v_z^2/kz^2)^{1/2} - 1]\}/(kz^2 - v_z^2)^{1/2})dz_0 \;. \tag{9}$$

This integral determines a realistic ion distribution function if a Monte Carlo simulation of electron avalanches is used to determine $P(z)$, the electron-impact ionization rate per unit volume. A flux density evaluated directly from an exact distribution function includes drift, diffusion, and all higher-order terms of a density gradient expansion. An exact solution may be particularly valuable in modeling an abrupt cathode-fall negative-glow boundary. The objective here is to prove that the average ion velocity is the equilibrium drift velocity in most of the cathode-fall region. The true source function as determined in Monte Carlo simulations peaks near the cathode-fall–negative-glow boundary, and thus is a decreasing function of $z$ throughout the cathode-fall region. The upper limit on the equilibration distance is determined by using a uniform ionization rate per unit volume for all positive $z$. The average ion velocity for a linearly increasing field with a uniform source of ions or all positive $z$ is

$$\langle v_z \rangle = \frac{\int\int\int f v_z\, dv_z\, dv_x\, dv_y}{\int\int\int f\, dv_z\, dv_x\, dv_y}$$

$$= \frac{z}{\exp(-\sigma Nz/\pi)I_0(\sigma Nz) + L_0(\sigma Nz) + \sigma Nz[I_1(\sigma Nz) + L_1(\sigma Nz) + 2/\pi]\}/(2\sqrt{k})} \;, \tag{10}$$

where $I_1(z)$ and $L_1(z)$ are modified Bessel and modified Struve functions of order 1.[33,34] The distance required for the average velocity to reach 90% of the equilibrium drift velocity $\sqrt{2kz/\pi\sigma N}$ is 5.7 mean free paths.

The ratio of the thickness of the cathode-fall region $d_c$ to the mean free path for symmetric charge exchange $\sigma N^{-1}$ is typically 50 to 100 for a rare-gas cathode fall. A change in discharge current or pressure changes $Nd_c$ only slightly, thus the observation

$$\sigma Nd_c > 5.7 \tag{11}$$

justifies using an equilibrium ion drift velocity in nearly all of the cathode-fall region. The approximation fails only within the first six mean free paths from the cathode-fall–negative-glow boundary. The preceding proof that the ions are in hydrodynamic equilibrium enables us to complete the determination of the current balance at the surface of the cathode.

The drift velocity at the cathode surface for low currents is determined from Helm's precise mobility data.[36] At the high current densities the drift velocity is calculated using the equilibrium expression

$$\langle v_z \rangle^0 = [2eE^0/(m_+\pi\sigma N)]^{1/2} \;, \tag{12}$$

where $E^0$ is the field at the cathode surface. The symmetric charge exchange cross section $\sigma$ is taken from the calculation of Sinha, Lin, and Bardsley.[37] These calculations agree with Helm's experimentally derived cross sections. The slight energy dependence of $\sigma$ does not weaken the proof of equilibration, but it is important to use a value of $\sigma$ that corresponds to the average ion energy at the cathode surface. The average ion energy at the cathode from the equilibrium distribution function of Eq. (7) is

$$\langle m_+ v_z^2/2 \rangle^0 = eE^0/2N\sigma \;. \tag{13}$$

A self-consistent average ion energy and symmetric charge exchange cross section are conveniently determined from a graphical analysis using a plot of $\sigma$ versus ion energy. The intersection of the $\sigma$ versus ion energy

TABLE I. Summary of the analysis of the electric field and gas density measurements to determine the current balance at the cathode surface. The dimensionless ratio $J^0_+/(J_D - J^0_+)$ is the number of ions produced in the cathode-fall region per (net) electron emitted from the cathode.

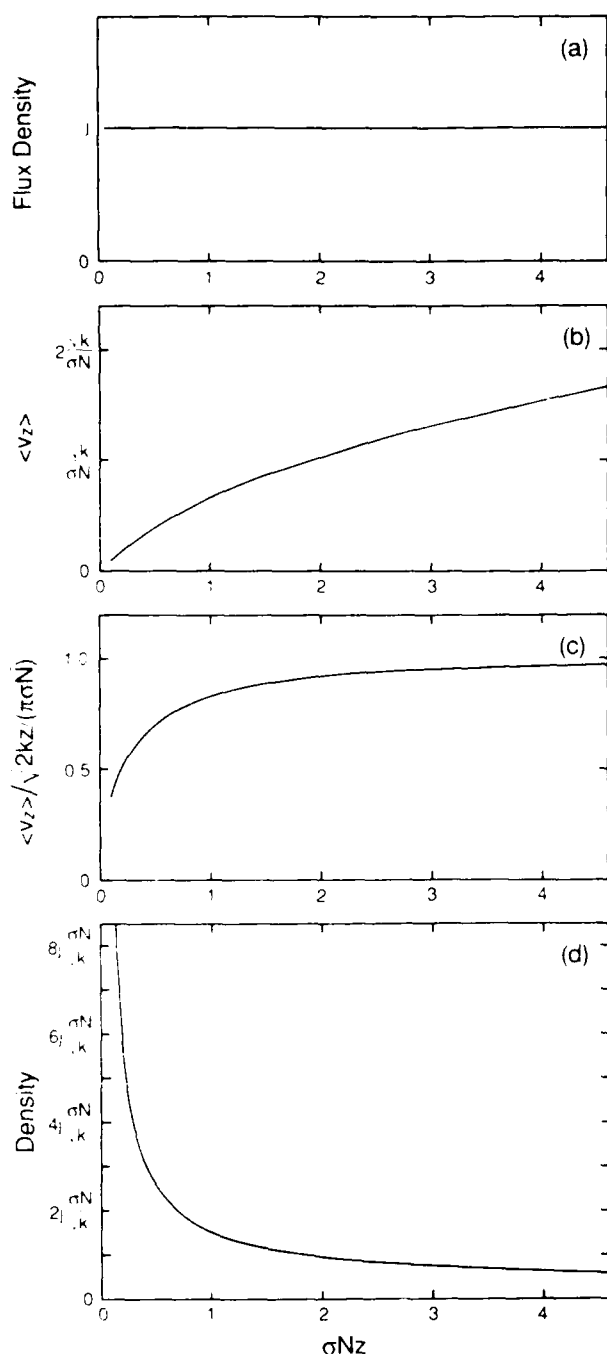| | $J_D$ (mA/cm²) | | | | |
|---|---|---|---|---|---|
| | 0.190 | 0.519 | 0.846 | 1.18 | 1.50 |
| $E^0$ (kV/cm) | 0.897 | 1.426 | 1.870 | 2.395 | 3.017 |
| $d$ (cm) | 0.382 | 0.301 | 0.282 | 0.300 | 0.396 |
| $V_{cf}$ (kV) | 0.173 | 0.211 | 0.261 | 0.356 | 0.600 |
| $V_c$ (kV) | 0.171 | 0.215 | 0.264 | 0.359 | 0.597 |
| $N \cdot 10^{18}$ cm⁻³ | 11.2 | 10.8 | 10.3 | 9.48 | 8.01 |
| $\rho \cdot 10^{-10}$ C/cm³ | 2.08 | 4.20 | 5.88 | 7.07 | 6.74 |
| $\langle m_+ v_z^2/2 \rangle^0$ (eV) | 1.66 | 2.82 | 3.89 | 5.71 | 8.92 |
| $\sigma \cdot 10^{-16}$ cm² | | | 23.3 | 22.1 | 21.1 |
| $\langle v_z \rangle^0 \cdot 10^5$ cm/sec | 7.12 | 9.28 | 10.9 | 13.2 | 16.5 |
| $J^0_+$ (mA/cm²) | 0.148 | 0.390 | 0.641 | 0.933 | 1.11 |
| $J^0_+/(J_D - J^0_+)$ | 3.52 | 3.02 | 3.13 | 3.78 | 2.85 |

FIG. 6. Integrals of the Eq. (6) distribution function vs the number of mean free paths from the source at $z_0$ near the origin: (a) flux density, (b) average velocity, (c) ratio of average velocity to local equilibrium drift velocity, (d) density.

plot with a hyperbola defined by Eq. (13) and an empirical $E^0/N$ determines the self-consistent average ion energy and symmetric charge exchange cross section. The uncertainty in $\langle v_z \rangle^0$ is $\pm 4\%$ in all cases.

Table I summarizes the analysis of the electric field and gas density measurements to determine the current balance at the cathode surface. The excellent agreement between $V_{vm}$, a voltage determined with a digital voltmeter, and $V_{ef}$, a voltage determined from integrating the field

data, indicates that the field measurements are on the average accurate to 1%. The uncertainty in the ion charge density $\rho_+$ is comparable to the uncertainty in the field measurements. The electron current density at the cathode surface is $J_D - J_+^0$ where $J_D$ is the discharge current density. The electron current density has, of course, a larger fractional uncertainty than the ion current density. The dimensionless ratio $J_+^0 / (J_D - J_+^0)$ is the current balance or ratio of the ion current to electron current at the cathode surface. This ratio is of particular interest because it is the number of ions produced in the cathode-fall region per (net) electron emitted from the cathode.

## V. METASTABLE DENSITY MEASUREMENTS

The spatial dependence of $2\,^1S$ and $2\,^3S$ He metastable densities is mapped along the axis of the discharge for each of the five current densities. The experiment has two parts: (1) laser-induced fluorescence is used to create spatial maps of relative metastable densities and (2) absorption measurements are used to put an absolute scale on the density maps. The absolute density of metastables is modeled in Sec. VI to derive metastable production rates for comparison to Monte Carlo simulations. From the spatial distribution of metastables, and specifically from the suppression of $2\,^1S$ metastables in the negative glow, valuable information is gained about the low-energy electrons in the negative glow.

Laser-induced fluorescence is the best detection method for producing relative maps of the metastable density. Although optogalvanic detection offers superior sensitivity near the cathode surface, its sensitivity is position dependent. The laser-induced fluorescence measurements are made using a pulsed $N_2$ laser pumped dye laser tuned to either the 501.6-nm transition for mapping the $2\,^1S$ density or the 388.9-nm transition for mapping the $2\,^3S$ density. The beam passes through a 250-$\mu$m slit which was imaged 1:1 into the center of the discharge using a 13-cm-focal-length cylindrical lens. The laser polarization is along the axis of the discharge. Fluorescence is collected in a direction mutually perpendicular to the laser axis and the axis of the discharge. The fluorescence collection system includes a lens and slit combination to isolate the central portion of the laser-discharge interaction region. This eliminates possible distortion of the spatial map due to metastable populations in the fringes. The lens is masked to cut down on fluorescence scattered from electrodes which can also distort the map.

Excitation transfer among the $n = 3$ levels due to collisions with ground-state atoms allows the monitoring of fluorescence at a wavelength different from that of the laser.[38] Interference filters are used to isolate 667.8-nm $(3\,^1D - 2\,^1P)$ radiation when the laser is tuned to 501.6- and 706.5-nm $(3\,^3S - 2\,^3P)$ radiation when the laser is tuned to 388.9 nm. In this way scattered laser light is eliminated from the signal. The fluorescence is detected with a photomultiplier. The signal is averaged over $\sim 1000$ laser pulses. The entire fluorescence collection system is mounted on the translation stage so it remains fixed with respect to the discharge.

The laser absorption measurements for determining an absolute scale for the metastable densities are made using the same transitions as the laser-induced fluorescence studies. Although absorption detection is far less sensitive than optogalvanic or fluorescence detection, it does provide a convenient absolute scale. An étalon is introduced to reduce the laser bandwidth to 500 MHz and thereby simplify analysis of the absorption data. The beam passes through a 500-$\mu$m slit which is imaged 1:1 into the discharge. Absorption measurements are made at the peak of the spatial density at two current densities. The intensity of the laser is substantially reduced to avoid saturation of the transition. The transmitted laser light is monitored with a photodiode detector. The signal from the detector is processed with a boxcar averager and plotted on a strip-chart recorder as the laser is scanned through the transition. Metastable densities are determined from the integral over frequency of the natural log of the transmittance. Each density is an average of ten measurements.

Figures 7 and 8 show the results of the metastable density measurements. The density maps have an uncertainty of ~20% in the center of the discharge rising to ~30% near the electrodes.
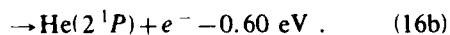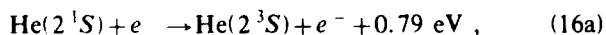
## VI. METASTABLE TRANSPORT AND KINETICS

The metastable maps of Sec. V are analyzed in this section. The transport and kinetics of $2\,^1S$ and $2\,^3S$ metastables in the discharge are modeled using a pair of balance equations which are coupled differential equations,

$$D_s \frac{\partial^2 M_s}{\partial z^2} - \beta M_s^2 - \beta M_s M_t - \gamma M_s N - \kappa n_e M_s + P_s = 0 ,$$

(14)

$$D_t \frac{\partial^2 M_t}{\partial z^2} - \beta M_t^2 - \beta M_s M_t + \kappa n_e M_s + P_t = 0 ,$$

(15)

where $M_{s,t}$ is the metastable density, $N$ is the density of ground-state atoms, $n_e$ is the density of low-energy electrons, $D$ is the diffusion coefficient, $P$ is the production rate per unit volume, $\gamma$ is the rate constant for singlet metastable destruction due to collisions with ground-state atoms, $\beta$ is the rate constant for destruction of metastables due to metastable-metastable collisions, $\kappa$ is the effective rate constant for destruction of singlet metastables due to low-energy electron collisions, and $s$ and $t$ subscripts indicate singlet and triplet metastables, respectively. The first three terms in each equation are loss terms arising from diffusion and collisions between metastables. There is an additional loss term in the singlet equation due to collisions with ground-state He atoms. The marked suppression of singlet metastables in the negative glow is due to low-energy electron collisions, i.e. the reactions

$$\mathrm{He}(2\,^1S)+e \rightarrow \mathrm{He}(2\,^3S)+e^- +0.79 \text{ eV} ,$$  (16a)

$$\rightarrow \mathrm{He}(2\,^1P)+e^- -0.60 \text{ eV} .$$  (16b)

These reactions both have large cross sections. Exo-

thermic reaction (16a) is a spin exchange, $s$-wave process with a large cross section for low-energy electrons. Endothermic reaction (16b) corresponds to a very strong optically allowed transition; it has a large cross section peaking at electron energies roughly three times thresh-
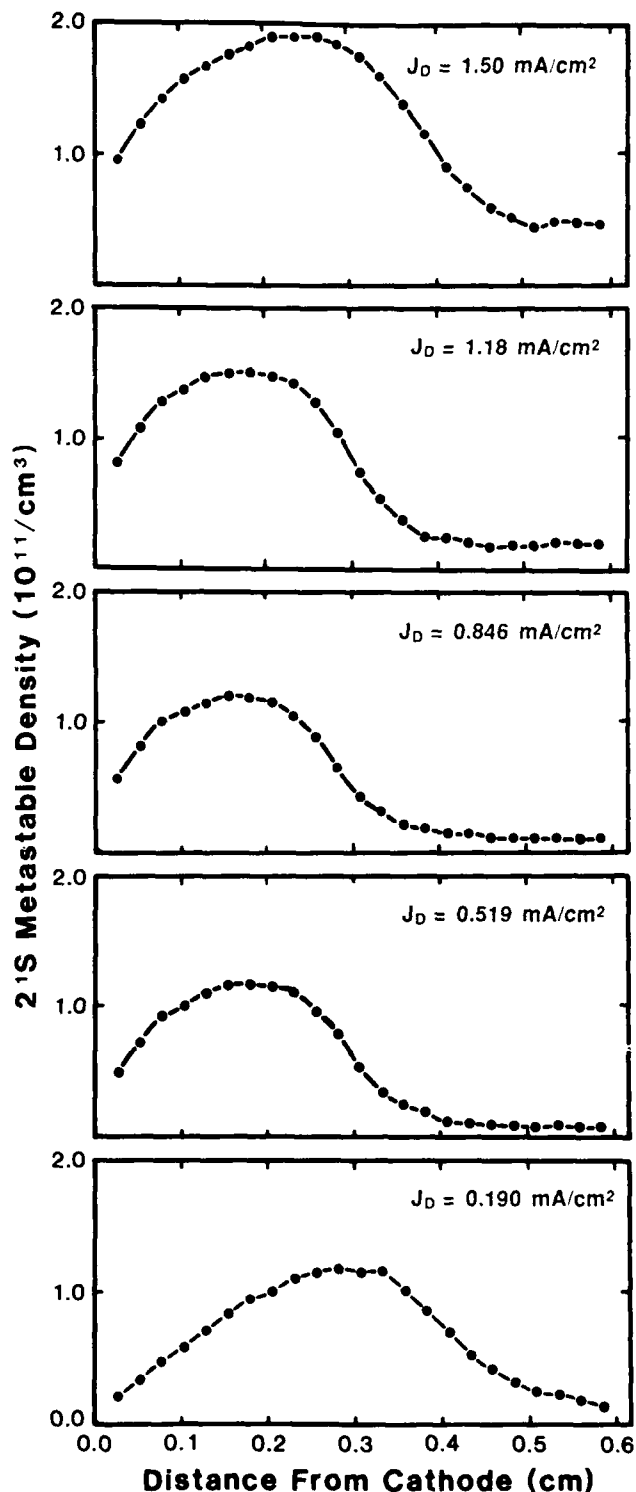


FIG. 7. Helium $2\,^1S$ metastable density as a function of distance from the cathode for five discharge current densities at 3.50 Torr.

old energy. Reaction (16a) dominates the $2\,^1S$ quenching, because (16b) must compete with the $2\,^1P \rightarrow 2\,^1S$ radiative decay. The metastable spin conversion reaction (16a) is included as the fifth loss term in the singlet equation and a corresponding gain in the triplet equation.

Low-energy electrons are confined to the negative-glow region due to the high fields in the cathode-fall region. The spatial dependence of the low-energy electron density $n_e$ is therefore that of a step function; it is zero in the cathode-fall region, rising sharply at the negative-glow boundary to some constant value. The spatial dependence of the production terms is assumed to be a fundamental diffusion mode except at the highest and lowest currents where the fundamental mode is skewed slightly to maintain the peak at the cathode-fall–negative-glow boundary. The assumption that the production peaks at the boundary is borne out by Monte Carlo simulations discussed later in this paper. Values for $DN$, $\gamma$, and $\beta$ are taken from Phelps.[39] The temperature dependence of $D$ is taken from Buckingham and Dalgarno,[40] that of $\gamma$ is taken from Allison, Browne, and Dalgarno.[41]

The key quantities which are determined in this modeling are the integrated production rates, $\int P_s dz$ and $\int P_t dz$, and the product of the rate constant for metastable spin conversion with the low-energy electron density, $\kappa n_e$. Values for these key quantities are assumed, the coupled equations are solved for $M_s(z)$ and $M_t(z)$, and a comparison is made to the empirical metastable density maps. Diffusion modes up to tenth order are included in the solutions because of the spatial asymmetry introduced by metastable spin conversion. After the comparison with the empirical metastable maps, the values for $\int P_s dz$, $\int P_t dz$, and $\kappa n_e$ are adjusted and the processes iterated until a good fit to the empirical metastable maps is achieved. The value for $\kappa n_e$ determined in this fashion should be considered an effective rate of metastable spin conversion because it must be modified to include the reverse reaction. The reverse reaction is not negligible if the relative singlet versus triplet metastable density approaches thermal equilibrium with the low-energy electron gas in the negative glow.

Figures 9 and 10 show both the measured and calculated $2\,^1S$ and $2\,^3S$ densities, respectively, for one of the current densities. Table II summarizes for all current densities the parameters used in the model such as $D_s$, $D_t$, $\gamma$, and $\beta$ and the key quantities $\int P_s dz$, $\int P_t dz$, and $\kappa n_e$. The dimensionless ratios

$$e \int P_s dz / (J_D - J^0_+) , \quad e \int P_t dz / (J_D - J^0_+) ,$$

where $J_D - J^0_+$ is the empirical electron current density at the cathode, are of particular interest. These dimensionless ratios are the average number of singlet and triplet metastables produced per (net) electron emitted from the cathode.

## VII. MONTE CARLO SIMULATIONS

Monte Carlo simulations are used in this work to study electron avalanches in the cathode-fall and negative-glow regions. There is no need for Monte Carlo simulations of ion transport in the cathode-fall region because we have the exact analytic solutions to the Boltzmann equation for ions as presented in Sec. IV. The Monte Carlo simulations are used to determine the number of ions and metastable atoms produced per (net) electron emitted from the cathode. The number of ions produced in the
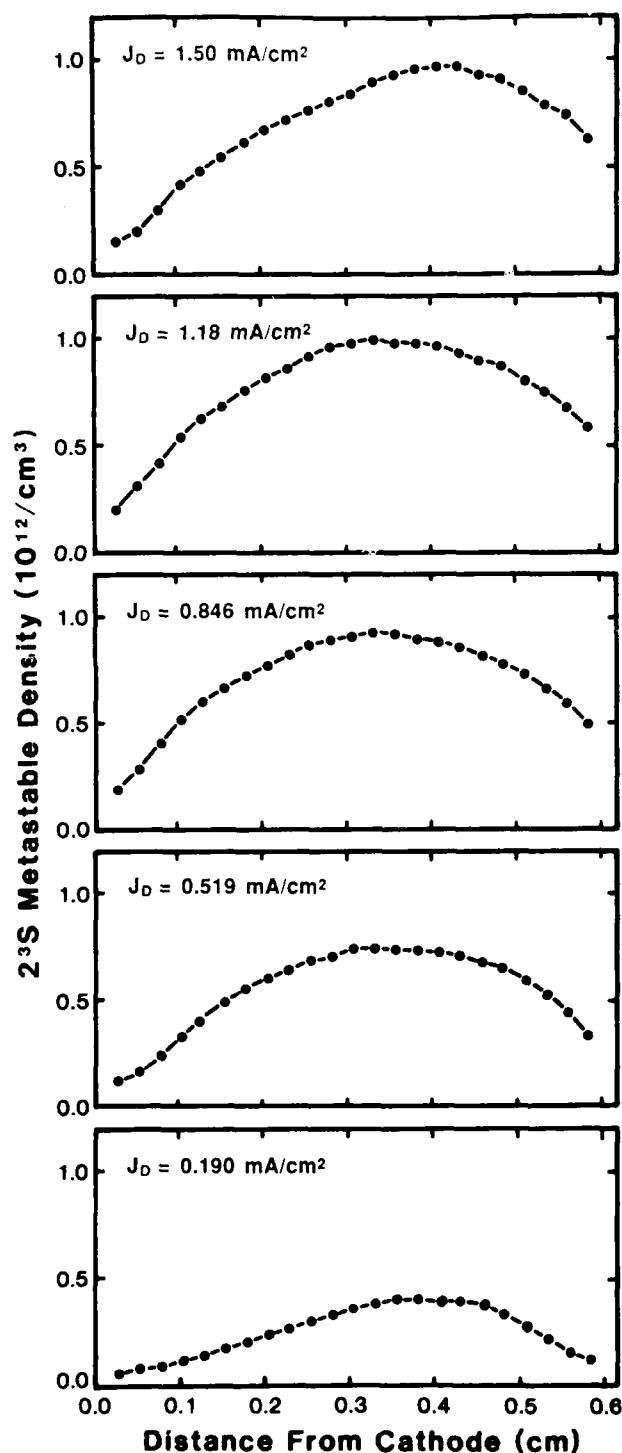


FIG. 8. Helium $2\,^1S$ metastable density as a function of distance from the cathode for five discharge current densities at 3.50 Torr.
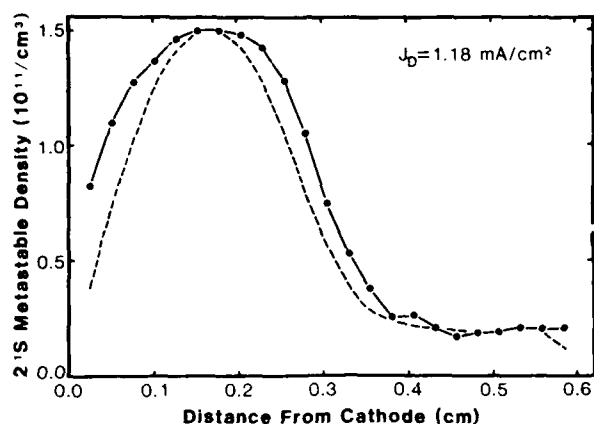
FIG. 9.  Helium $2\,^1S$ metastable density for $J_D = 1.18$ mA/cm$^2$. The points are the experimental data and the dashed curve is the calculated fit to the data.

cathode-fall region per emitted electron is directly comparable to the empirical current balance of Sec. IV. The number of metastables produced is comparable to the results of Sec. VI.

The Monte Carlo simulations include the empirical field distributions and gas densities for the cathode-fall region as given in Sec. III. A uniform field of 1.0 or 10.0 V/cm is assumed for the negative-glow region. We believe that there is actually a reversal of the field direction at the boundary between the cathode-fall and negative-glow regions. The reversal would produce a potential-energy well which holds the low-energy electron gas of the negative glow. The reversal would also result in a backdiffusion (or drift) toward the anode of ions produced in the negative glow. Unfortunately it is difficult to include a field reversal in the Monte Carlo simulations. However, the actual magnitude and direction of the weak field in the negative-glow region has very little effect on
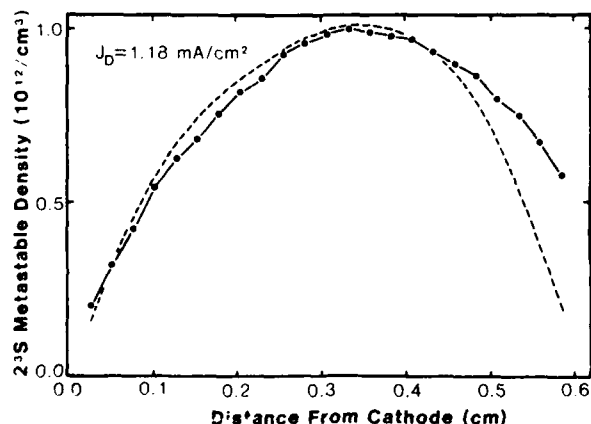


FIG. 10.  Helium $2\,^3S$ metastable density for $J_D = 1.18$ mA/cm$^2$. The points are the experimental data and the dashed curve is the calculated fit to the data.

excitation and ionization in the negative glow which is produced by high-energy beam electrons from the cathode-fall region.

The Monte Carlo simulations are three dimensional in the sense that they include angular scattering, but they do not include edge effects due to fringing of the discharge. One-dimensional infinite plane parallel geometry is assumed. Null collision techniques eliminate most of the time-consuming numerical integration in Monte Carlo simulations. The null collision technique used in this investigation was developed by Boeuf and Marode for nonuniform fields.[17] An interested reader will find more detail on the Monte Carlo technique in Ref. 17. The simulations include anisotropic elastic scattering, excitation to 22 levels, direct ionization, and other less important processes.

Total and differential elastic scattering cross sections are taken from the calculations of LaBahn and Callaway.[2] The analytic expressions given by Alkhazov for excitation cross sections are used in the simulations.[43] Excitation of $n = 2$ to 5 singlet and triplet $s$ and $p$ levels is included in the simulation. Excitation of the $n = 3$ to 5 singlet and triplet $d$ levels is also included. Although some experimental or theoretical information on differential excitation cross sections for electrons on He is available, it is rather limited. Thus we use an isotropic scattering approximation for excitation.

A fraction of the atoms excited to the $3p$ levels and above are associatively ionized. An accurate determination of the fraction requires accurate associative ionization cross sections, cross sections for excitation transfer due to ground-state atom collisions, and radiative decay rates. On the basis of what information is available we estimate that 25% of the atoms in the $3p$ levels and above are associatively ionized at 3.5 Torr.[28,38] The electrons released in associative ionization contribute to the avalanche; they are assumed to have an initial kinetic energy of 1.0 eV and an isotropic angular distribution. The remaining 75% of the atoms excited to the $3p$ and higher triplet levels, and all of the atoms excited to the $3\,^3S$ and $2\,^3P$ levels are assumed to radiate to the $2\,^3S$ metastable level. This cascade contribution is combined with direct excitation of the $2\,^3S$ level to determine the total production rate for $2\,^3S$ metastables. The total production rate for $2\,^1S$ metastables includes direct excitation and a cascade contribution of 19% of the excitation to the $3p$ and higher singlet levels. The total production rate for the $2\,^1P$ resonant level includes direct excitation and a cascade contribution of all of the $3\,^1S$ excitation and 56% of the excitation to the $3p$ and higher singlet levels. These assumptions are based on a significant $l$ mixing of $3p$ and higher level populations due to collision with ground-state atoms.

In a vacuum nearly all of the atoms excited to the $2\,^1P$ resonant level decay to the ground state via vuv emission. Radiation trapping reduces the effective decay rate to $1.3 \times 10^6$ sec$^{-1}$, which is comparable to the vacuum decay rate of $1.98 \times 10^6$ sec$^{-1}$ for the $2\,^1P \rightarrow 2\,^1S$ infrared branch at 2 $\mu$m.[28] However, the $2\,^1P \rightarrow 2\,^1S$ branch is also trapped in the cathode-fall region of our discharge experiments, thus we do not include any of the $2\,^1P$ exci-

TABLE II. Summary for all current densities of parameters used in the model as well as the key quantities $\int P_s dz$, $\int P_t dz$, and $\kappa n_c$. The dimensionless ratios $e \int P_s dz/(J_D - J^0_c)$ and $e \int P_t dz/(J_D - J^0_c)$ are the average number of singlet and triplet metastables produced per (net) electron emitted from the cathode.

| | $J_D$ (mA/cm²) | | | | |
| | 0.190 | 0.519 | 0.846 | 1.18 | 1.50 |
|---|---|---|---|---|---|
| $N$ ($10^{16}$ cm⁻³) | 11.2 | 10.8 | 10.3 | 9.48 | 8.01 |
| $D_s$ (cm²/sec) | 127 | 140 | 152 | 173 | 236 |
| $D_t$ (cm²/sec) | 136 | 150 | 163 | 185 | 253 |
| $\gamma$ ($10^{-15}$ cm³/sec) | 6.0 | 6.5 | 6.9 | 7.8 | 9.9 |
| $\beta$ ($10^{-9}$ cm³/sec) | 3.5 | 3.5 | 3.5 | 3.5 | 3.5 |
| $\int P_s dz$ ($10^{15}$ cm⁻²sec⁻¹) | 0.454 | 0.664 | 0.830 | 1.05 | 1.38 |
| $\int P_t dz$ ($10^{15}$ cm⁻²sec⁻¹) | 0.711 | 1.86 | 2.77 | 3.56 | 4.34 |
| $e \int P_s dz/(J_D - J^0_c)$ | 1.73 | 0.824 | 0.648 | 0.680 | 0.566 |
| $e \int P_t dz/(J_D - J^0_c)$ | 2.71 | 2.31 | 2.16 | 2.31 | 1.78 |
| $\kappa n_c$ ($10^4$ sec⁻¹) | 1.5 | 8.5 | 7.0 | 5.5 | 3.0 |

tation in calculating a total production rate for $2\,^1S$ metastables. This approximation is not completely satisfactory because the $2\,^1P \rightarrow 2\,^1S$ branch is not highly trapped in the negative glow where the $2\,^1S$ density is suppressed by low-energy electron collision. The $2\,^1P$ level is feeding population to the $2\,^1S$ level through a collisional-radiative coupling, and the $2\,^1S$ level is feeding population to the $2\,^3S$ through a collisional coupling. The net result is that the Monte Carlo simulation produces a metastable production rate which is somewhat lower than the empirical rate.

The analytic expression by Alkhazov for the total ionization cross section is used in the simulation.[43] We also use Alkhazov's analytic expression for the differential cross section with respect to energy.[43] Simulations are performed using two different angular distributions for ionizing collisions.

The first simulations assumed isotropic angular distributions for both outgoing electrons in an ionizing collision. Some of the results based on the isotropic angular distribution or ionizing collisions were presented in a recent Letter.[44] The first simulations predicted a current balance in good agreement with experiment in a near-normal cathode-fall region, but predicted too much ionization in a highly abnormal cathode-fall region. The $E/N$ reaches 3000 Td (townsend) in the abnormal cathode-fall region, thus the inelastic processes are resulting in forward peaked angular scattering distributions. Numerical solutions of the Boltzmann equation for electrons have traditionally assumed isotropic angular distributions for inelastic collisions. Recent work by Phelps and Pitchford explores the effect of anisotropic inelastic scattering at very high $E/N$ in $N_2$.[45]

Our second simulations use the assumptions used by Boeuf and Marode: (1) the incident, scattered, and ejected electron velocities are coplanar, and (2) the scattered and ejected electron velocities are perpendicular with zero net transverse momentum.[17] The justification for these assumptions is not strong, but it does represent a reasonable attempt to introduce anisotropic scattering in ionizing collisions.

The details of the electron interactions with the cathode and anode must be specified. The kinetic energy of electrons emitted from the cathode is assumed to be 5.0 eV and they are assumed to have a random angular distribution in the forward direction. The use of a more realistic energy distribution for electrons emitted at the cathode does not affect ionization or excitation in the Monte Carlo simulations. Some electrons are reflected back to the cathode by elastic scattering from He atoms before they suffer an inelastic collision. Electrons do not have sufficient total energy to reach the cathode after an inelastic collision. The percentage of the gross electron emission which is backscattered to the cathode varies from 19% at the lowest current density (a near-normal cathode fall) to 3.6% at the highest current density (a highly abnormal cathode fall). All Monte Carlo results are presented in terms of net electron emission from the cathode. The Monte Carlo simulation assumes no reflection from the anode; each electron is absorbed immediately when it reaches the anode. This approximation will cause the Monte Carlo simulation to predict excitation and ionization rates in the negative glow which are lower than those in experiment. The discordance is significant only in the case of the highly abnormal glow discharge at 1.50 mA/cm².

Figure 11 includes Monte Carlo histograms giving the number of ionization and excitation events per (net) electron emitted from the cathode as a function of distance from the cathode. The results of Fig. 11 are based on the anisotropic angular distribution for ionizing collisions. These histograms are for field distributions and gas densities corresponding to 0.519 mA/cm². The spatial dependences of the ionization and excitation rates are all described by a roughly symmetric function which peaks near the cathode-fall–negative-glow boundary. The simulations show that the beam electrons in He penetrate beyond the cathode-fall–negative-glow boundary by a distance comparable to $d_c$, the thickness of the high-field cathode-fall region. The penetration distance will scale as the inverse of the gas density in a fashion similar to $d_c$. The $2\,^3S$ metastable excitation has the most asymmetric
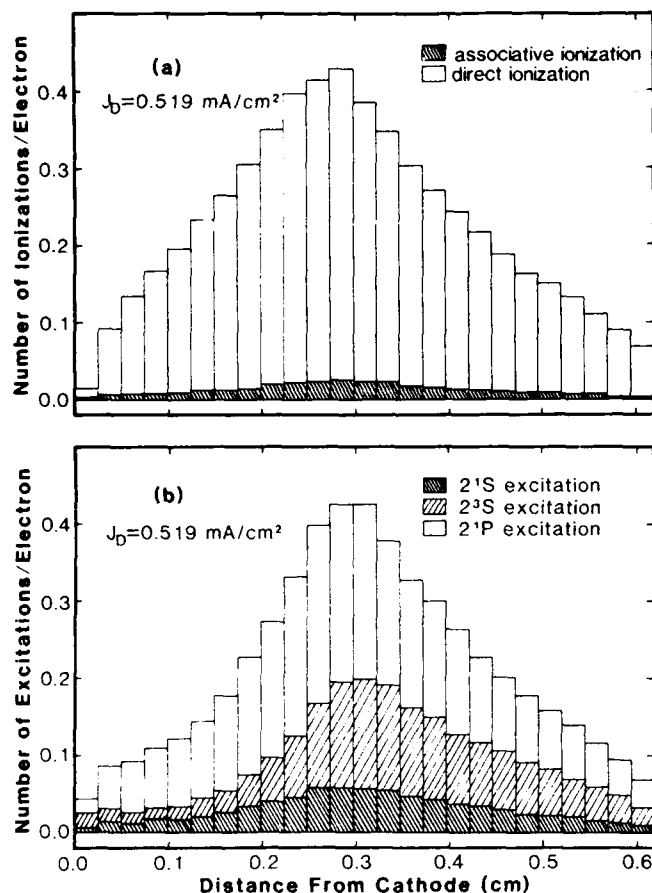
FIG. 11. Monte Carlo histograms showing the number of (a) ionization events and (b) excitation events per (net) electron emitted from the cathode as a function of distance from the cathode. The histogram for total excitation is subdivided into $2\,^1S$, $2\,^3S$, and $2\,^1P$ excitation. The histogram for total ionization is subdivided into associative and direct ionization.

spatial dependence; it is stronger in the negative-glow than in the cathode-fall region. This is explained by the sharp peak just above threshold in the energy dependence of triplet excitation cross sections. The asymmetry in the

empirical maps of the $2\,^3S$ metastable density is due in part to the spatial dependence of triplet excitation. The spatial dependences of excitation and ionization at other discharge current densities are similar. The results of Monte Carlo simulations for all five current densities are presented in Tables III and IV. The Table III results are based on the isotropic angular distribution for ionizing collisions, and those of Table IV are based on the anisotropic angular distribution for ionizing collisions.

The absolute accuracy of the Monte Carlo simulations must be estimated in order to compare the simulations to experiment. Statistical uncertainty is not large because several thousand complete avalanches were simulated for each of the five discharge currents. Alkhazov's analytic expressions for the He cross sections are based on theoretical and experimental work by many groups.[43] He estimates that the uncertainty is ±25% at low energy, and ±5% at high energy where a Born approximation is reliable. We believe his uncertainties are reasonable and we estimate that the Monte Carlo results have an uncertainty of ±25%.

## VIII. COMPARISON OF EXPERIMENTAL RESULTS AND MONTE CARLO SIMULATIONS

The first comparison of experimental results to Monte Carlo simulations involves the current balance at the cathode. This dimensionless quantity is the ratio of ion to electron current at the cathode. Figure 12 is a plot of the ratio versus total discharge current density. The experimental measurements are points with uncertainties which are discussed in Sec. IV. The dashed line is the same ratio determined from Monte Carlo simulations using the isotropic angular distribution for ionizing collisions. The calculations represented by the dashed line were included in a recent Letter.[44] The solid line is the ratio as determined from Monte Carlo simulations using the anisotropic angular distribution for ionizing collisions. All Monte Carlo simulations include the same anisotropic elastic scattering. Clearly the assumption of isotropic inelastic scattering is beginning to fail in the highly abnormal cathode-fall region where $E/N$ reaches 3000 Td.

TABLE III. Results of Monte Carlo simulations of electron avalanches based on the isotropic angular distribution for ionizing collisions. All results are per (net) electron emitted from the cathode. The ionization in the cathode-fall region includes direct plus associative ionization occurring between the surface of the cathode and a distance $d_c$ from the cathode. Other quantities include all events between the cathode and anode.

| | $J_D$ (mA/cm$^2$) | | | | |
| --- | --- | --- | --- | --- | --- |
| | 0.190 | 0.519 | 0.846 | 1.18 | 1.50 |
| $E^0$ (kV/cm) | 0.897 | 1.426 | 1.870 | 2.395 | 3.017 |
| $d_c$ (cm) | 0.382 | 0.301 | 0.282 | 0.300 | 0.396 |
| $N$ ($10^{16}$ cm$^{-3}$) | 11.2 | 10.8 | 10.3 | 9.48 | 8.01 |
| $2\,^1S$ production | 0.88 | 0.88 | 0.99 | 1.06 | 0.96 |
| $2\,^3S$ production | 2.05 | 1.92 | 2.04 | 2.04 | 1.62 |
| $2\,^1P$ production | 3.06 | 3.37 | 3.91 | 4.50 | 4.51 |
| Associative ionization | 0.36 | 0.38 | 0.42 | 0.47 | 0.49 |
| Direct ionization | 4.70 | 5.98 | 7.31 | 9.02 | 9.84 |
| Ionization in the cathode-fall region | 3.89 | 3.77 | 4.06 | 4.52 | 5.71 |

TABLE IV. Results of Monte Carlo simulations of electron avalanches based on the anisotropic angular distribution for ionizing collisions. The quantity $\langle T_{an} \rangle$ is the average kinetic energy of electrons hitting the anode. Other quantities are per (net) electron emitted from the cathode.

| | $J_D$ (mA/cm$^2$) | | | | |
| | 0.190 | 0.519 | 0.846 | 1.18 | 1.50 |
|---|---|---|---|---|---|
| $E^n$ (kV/cm) | 0.897 | 1.426 | 1.870 | 2.395 | 3.017 |
| $d_c$ (cm) | 0.382 | 0.301 | 0.282 | 0.300 | 0.396 |
| $N$ ($10^{16}$ cm$^{-3}$) | 11.2 | 10.8 | 10.3 | 9.48 | 8.01 |
| $2\,^1S$ production | 0.77 | 0.75 | 0.75 | 0.74 | 0.53 |
| $2\,^3S$ production | 1.79 | 1.58 | 1.52 | 1.40 | 0.83 |
| $2\,^1P$ production | 2.82 | 2.98 | 3.14 | 3.28 | 2.51 |
| Associative ionization | 0.29 | 0.31 | 0.32 | 0.34 | 0.25 |
| Direct ionization | 4.37 | 5.37 | 6.13 | 6.88 | 5.86 |
| $\langle T_{an} \rangle$ (eV) | 14.0 | 16.7 | 21.8 | 36.5 | 106.5 |
| Ionization in the cathode-fall region | 3.40 | 3.10 | 2.97 | 3.11 | 3.24 |

The current balance from the Monte Carlo simulations includes direct electron-impact ionization and associative ionization due to collisions between highly excited and ground-state He atoms. Ionization from collisions between pairs of metastable atoms is not included, but it is a small ( $\leq 10\%$ ) contribution to the current balance from the Monte Carlo simulations.

The key issue in interpreting the Monte Carlo results is whether or not one should include any of the ionization produced in the negative glow when computing the ratio of the ion to electron current at the cathode. We maintained in a recent Letter, and we continue to maintain, that essentially none of the ionization produced in the negative glow contributes to the ion current at the cathode.[44] The ratio of the ion to electron current at the cathode is computed by summing ionization in spatial bins of a Monte Carlo histogram such as that of Fig. 11.
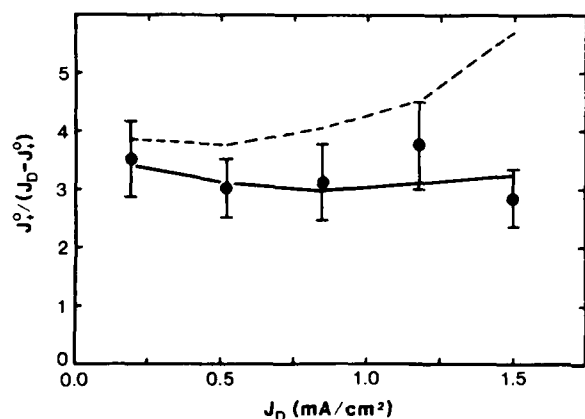


FIG. 12. Ratio of ion current to electron current at the cathode surface $J^0_+/(J_D - J^0_+)$ as a function of discharge current density. The points are the empirically derived values; the dashed line is the Monte Carlo results assuming the isotropic scattering for ionizing collisions; the solid line is the Monte Carlo results incorporating the anisotropic scattering for ionizing collisions.

The sum includes spatial bins from the cathode to a distance $d_c$ from the cathode where the cathode-fall–negative-glow boundary occurs. The inclusion of ions produced in the negative glow results in a serious discordance between the current balance determined from the Monte Carlo simulations and the empirical current balance.

The issue of the ion current at the cathode-fall–negative-glow boundary was already old and (in)famous when Druyvesteyn and Penning wrote their 1940 review.[46] They did not take a position on the problem in their review. Many experimental and theoretical studies addressed this problem in more recent decades. Long, for example, has a detailed discussion.[2] He argues convincingly for a field reversal in the negative glow, but does not specify the location of the field reversal. He does not take a definite position on the ion current at the cathode-fall–negative-glow boundary. Emeleus devotes an entire section of his 1981 review to the cathode-fall–negative-glow boundary or Glimmsaum, as he calls it.[6] He also fails to take a definite position on the importance of the ion current at the boundary.[6] The strongest position was taken by Little and von Engel.[47] Our arguments, which involve the empirical current balance and Monte Carlo simulations, are not the same as the arguments of Little and von Engels. Our position agrees with that of Little and von Engel. The ion current is a negligible fraction of the discharge current at the cathode-fall–negative-glow boundary. The loss mechanism needed to balance ion production in the negative glow will be discussed in Sec. IX.

The current balance, typically 3.3, is lower than we first expected. It is also surprisingly independent of total discharge current. The greater electric field and thickness in the cathode-fall region at high current are offset by a gas density reduction due to heating. The net result is that on average an electron produces the same amount of ionization in the cathode-fall region at low and high discharge currents. A current balance of 3.3 may be typical of only He.

The second comparison involves the number of metastable atoms produced in the cathode-fall and negative-

glow regions per (net) electron emitted from the cathode. The experimental measurements are plotted as points in Fig. 13. The empirical metastable production in units of $cm^{-2}sec^{-1}$ is divided by the empirical electron flux density at the cathode $(J_D - J_+^0)/e$. The error bars reflect only uncertainties in the metastable density measurements as discussed in Sec. V. The solid line of Fig. 13 is the result of Monte Carlo simulations using the anisotropic angular distribution for ionizing collisions. The
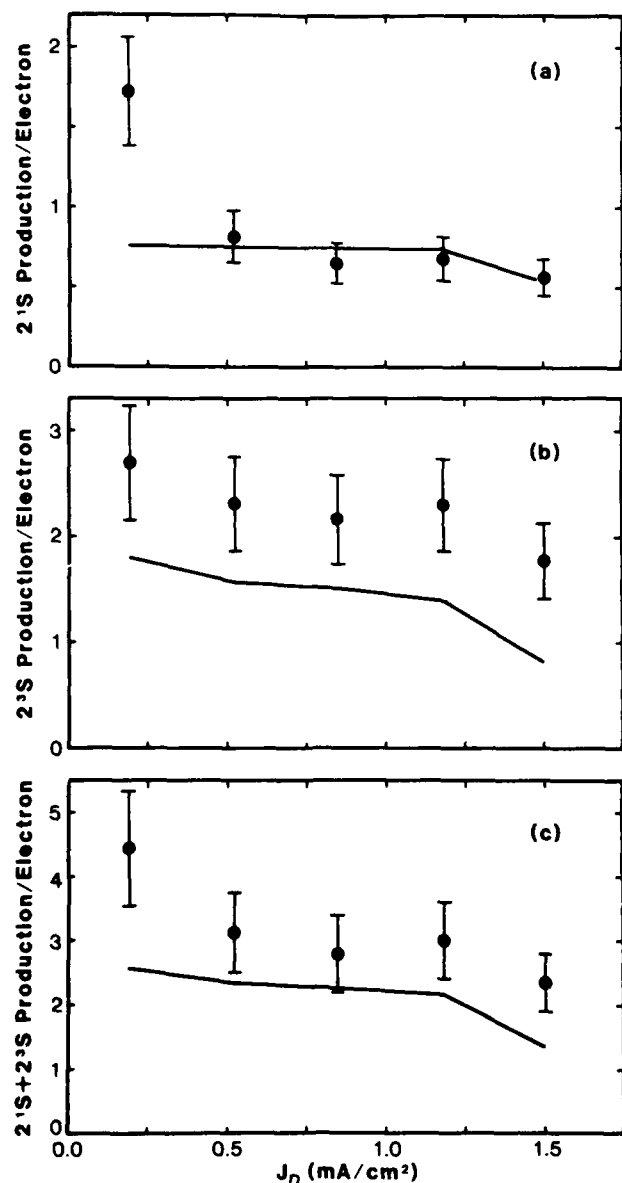


FIG. 13. (a) Helium $2\,^1S$ production, (b) helium $2\,^3S$ production, and (c) total metastable production as a function of discharge current density. The production values presented are spatially integrated production per (net) electron released from the cathode. The points are empirical results with error bars reflecting only the uncertainty of the metastable density measurements. The solid lines are Monte Carlo results using the anisotropic angular distributions for ionizing collision.

$2\,^1S$ production plotted in Fig. 13(a) shows excellent agreement between experiment and the Monte Carlo simulations except at $0.190$ mA/$cm^2$. The discordance in the near-normal glow discharge at $0.190$ mA/$cm^2$ is in part due to the neglect of the $2\,^1P \rightarrow 2\,^1S$ cascade contribution in Monte Carlo determinations of $2\,^1S$ production. At low current densities the $2\,^1P \rightarrow 2\,^1S$ radiation is not completely trapped. The experimental $2\,^3S$ production plotted in Fig. 13(b) is somewhat higher than that predicted by the Monte Carlo simulations. The total $2\,^1S$ and $2\,^3S$ metastable production plotted in Fig. 13(c) is also somewhat higher than that predicted by the Monte Carlo simulations. At least two effects are responsible. The experimental $2\,^3S$ production and the total metastable production are enhanced by a collisional-radiative coupling in the negative glow of the $2\,^1P$ population to the $2\,^1S$ and indirectly to the $2\,^3S$. Some of the $2\,^1P$ production results in metastable production. The disagreement in the highly abnormal glow discharge of $1.50$ mA/$cm^2$ is in part due to the assumption of no electron reflection from the anode. The Monte Carlo results summarized in Table IV show a very high average kinetic energy ($> 100$ eV) for electrons hitting the anode in the highly abnormal glow discharge. Some of these electrons should be reflected at the anode. The reflection from the anode will increase excitation and ionization in the negative glow and improve agreement on metastable production between the experiment and Monte Carlo simulations. The reflection will not significantly change the current balance because few of the reflected electrons will return to the cathode-fall region and produce ionization.

The agreement, although imperfect, between simulation and experiment on metastable production provides additional evidence that the current balance of 3.3 is correct. If most of the ions produced in the negative glow drifted to the cathode, then the current balance would be $\sim 6$. The resulting lower electron current at the cathode would change the analysis of the experimental metastable production per electron. The empirical metastable production per electron would double, and would be in serious discordance with the Monte Carlo simulations.

Figure 13(c) shows typically three metastable atoms produced per net electron emitted from the cathode. This number can be used to estimate the importance of metastable bombardment in electron emission from a cold cathode. If 50% of the metastables diffuse back to the cathode, and if the electron emission coefficient is 0.5, then the metastables could be responsible for 75% of the electron emission from the cathode.[48]

Little and von Engel recognized that neutral particles were playing an important role in emission from a cold cathode.[47] They mention metastables but emphasize uv and vuv photons.[47] Recent measurements indicate that metastables can have electron emission coefficients in excess of 0.5.[48] Photoelectron emission coefficients are rarely as large.

Neutral particles play a major role in electron emission from a cold cathode. It is for this reason that a current balance of 3.3 does not imply an emission coefficient of 0.3 for ion bombardment.

## IX. NEGATIVE GLOW

The considerable and detailed experimental and theoretical information on the He discharge described in this work enables us to analyze the negative glow. The negative-glow region starts a distance $d_c$ from the cathode where the cathode-fall field extrapolates to zero. It extends to the anode in our discharge cell. The separation of the electrodes was chosen so that no positive column would form. The negative-glow region is characterized by extremely small electric fields and a high density $n_c$ of low-energy electrons at temperature $T_c$. These low-energy electrons are *not* described in the Monte Carlo simulations. Results from the Monte Carlo simulations such as $\langle T_{an} \rangle$, the average energy of electrons striking the anode, are for the high-energy beam electrons. The low-energy electrons are most probably trapped in a potential-energy well. Monte Carlo simulations are not well suited for describing trapped particles.

The analysis of each empirical singlet metastable map as described in Sec. VI produced an effective rate $\kappa n_e$ for metastable spin conversion due to low-energy electrons in the negative glow. This process was discovered by Phelps and the rate constant $\kappa_m$ was measured for room-temperature ($k_B T_c = 0.025$ eV) electrons.[39] The dependence of this rate constant on electron temperature is $(T_c)^{-1/2}$ because the cross section scales roughly as the inverse of the electron energy.[49] Although we do not *a priori* know the temperature of the low-energy electrons in the negative glow, it is relatively easy to put some limits on it. Surely the temperature of the low-energy electrons must be greater than gas temperature. An upper limit on the electron temperature is determined by noting that the exothermic metastable spin conversion reaction depletes the singlets, but only until the relative singlet versus triplet metastable density comes into thermal equilibrium with the low-energy electron gas. Thus the empirical ratio $M_s/M_t$ in the negative glow must be greater than or equal to

$$\tfrac{1}{3}\exp(-0.79/k_B T_e) .$$

These limits on $T_e$ and knowledge of $\kappa n_e$ determine a range of possible electron temperatures and a corresponding electron density for each temperature as given by the expression

$$\kappa n_c = n_c [\kappa_m \sqrt{0.025 \text{ eV}/k_B T_c}$$
$$-(M_t/3M_s)\kappa_m \sqrt{0.025 \text{ eV}/k_B T_c}$$
$$\times \exp(-0.79 \text{ eV}/k_B T_c)] . \qquad (17)$$

This expression is represented by the thick solid lines of Fig. 14. The lower limit for the electron temperature provides a lower limit for the electron density of $2 \times 10^{11}$ cm$^{-3}$ at intermediate current densities.

Any electron temperature and density consistent with the suppression of the singlet metastables correspond to a short, $\sim 3 \times 10^{-4}$ cm, Debye length for the negative glow. The Debye length is an electrostatic shielding length for the negative glow. A short Debye length indicates a very abrupt transition between the cathode-fall region and the
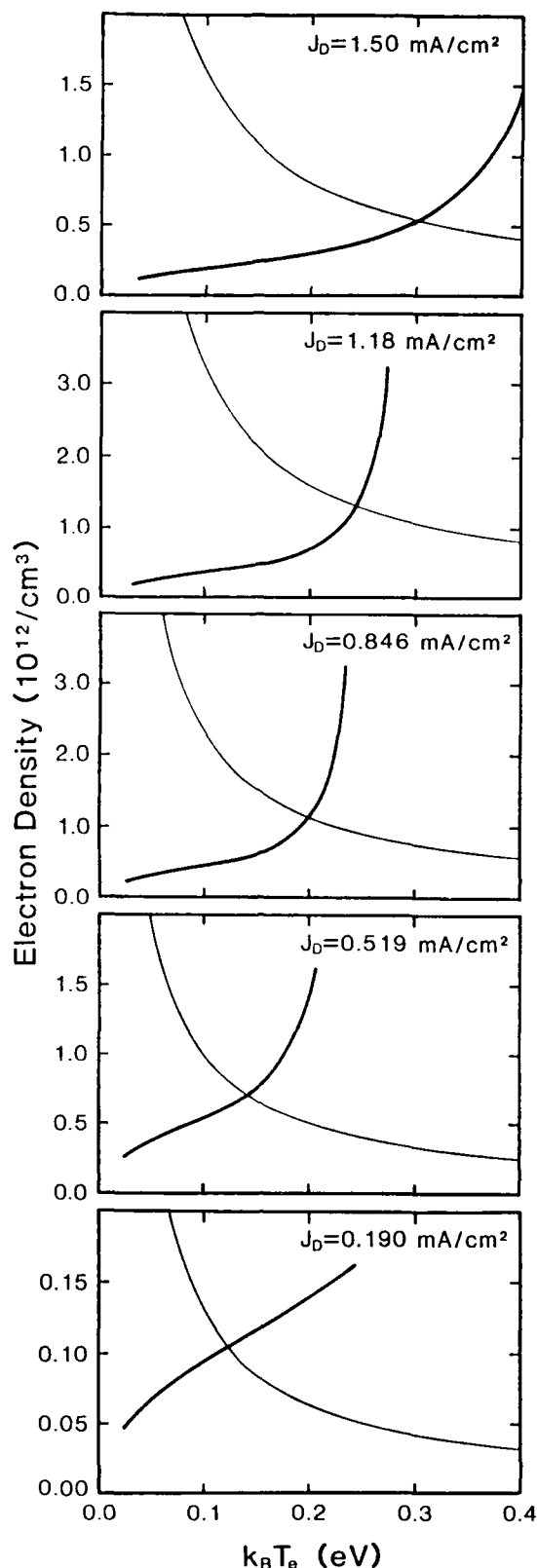


FIG. 14. Negative-glow electron density vs electron temperature for five discharge current densities. The thick line is the relationship from the analysis of the metastable maps. The thin solid line is from the ambipolarlike diffusion of the electron-ion pairs in the negative glow. The intersection of the two lines determines the density and temperature of the low-energy electrons in the negative glow.

negative glow.

The requirement that ion production in the negative glow be balanced by a loss mechanism provides an additional constraint on the low-energy electrons. Two loss mechanisms are possible: recombination or a backdiffusion (drift) of ions to the anode. We do observe $He_2$ molecular emission bands from the negative glow. These bands are conclusive evidence that some recombination occurs. The recombination rate constant for He is known to be very strongly dependent on the electron temperature.[50] If the electron temperature is near the gas temperature, then recombination could be quite important. Such a low electron temperature in the negative glow seems unlikely.

We suggest that ions in the negative glow drift to the anode in a process analogous to ambipolar diffusion. We note that this mechanism requires a field reversal near the cathode-fall–negative-glow boundary or the point where the cathode field extrapolates to zero. If the field reversal is assumed to be close to the anode then most of the ions produced in the negative glow would drift across the cathode-fall–negative-glow boundary. A large ion current at the boundary causes serious discordances between experiment and simulation in the current balance and the metastable production. The analogy to ambipolar diffusion is not perfect because the electron flux density on the anode must be larger than the ion flux density on the anode by $J_D/e$. The loss rate of low-energy electrons should be approximately

$$\mu_+ k_B T_e (\pi/2d_{ng})^2/e ,$$

where $\mu_+$ is the low-field ion mobility and $d_{ng}$ is the thickness of the negative glow. The factor of $\frac{1}{2}$ is due to the fact that the negative glow is asymmetric; the low-energy electrons cannot diffuse against the cathode field. The rate in the negative glow of ionization per unit volume $\langle P \rangle$ can be determined from the Monte Carlo simulations of Table IV. The rate $\langle P \rangle$ is a spatially averaged quantity

$$\left| \int_{d_c}^{d_c + d_{ng}} P \, dz \right| / d_{ng} .$$

Inclusion of some electron reflection from the anode will increase $\langle P \rangle$, but at most by a factor of 2 and only in the highly abnormal glow discharge at 1.50 mA/cm². This model provides a second relation between the density $n_e$ and temperature $T_e$ of the low-energy electrons in the negative glow

$$\langle P \rangle = n_e \mu_+ k_B T_e (\pi/2d_{ng})^2/e . \qquad (18)$$

This expression is represented by the thin solid lines of Fig. 14. The intersection of the thin and thick lines determines the density and temperature of the low-energy electrons in the negative glow.

The occurrence of the intersection on the steep portion of the plots of Eq. (17) is an indication that the metastable spin conversion reaction (16a) is proceeding to equilibrium. The relative density of the singlet and triplet metastable is in Boltzmann equilibrium with the low-energy, high-density electrons in the negative glow. Un-

der such conditions the empirical ratio of singlet to triplet metastables is providing the temperature of the negative-glow electrons. The accuracy of this determination of the electron temperature in the negative glow is not easy to assess.

The electron temperature $(k_B T_e \sim 0.25$ eV) is quite reasonable, but the density $(n_e \sim 10^{12}$ cm$^{-3})$ seems high. The alternate loss mechanism, recombination, could produce a lower electron density but only if the electron temperature is much lower. The suppression of the singlet metastables, which is quite dramatic at intermediate currents, provides a lower limit for the electron density $(n_e \geq 2 \times 10^{11}$ cm$^{-3})$ and upper limit for the electron temperature $(k_B T_e \leq 0.3$ eV).

## X. SUMMARY, CONCLUSIONS, AND FUTURE WORK

Various laser diagnostics are used to study the cathode-fall and negative-glow regions of a He glow discharge. The water-cooled Al cathode is operated over a range of current densities from a near-normal cathode fall of 173 V to a highly abnormal cathode fall of 600 V. Optogalvanic detection of Rydberg atoms is used to map the electric field in the cathode-fall region. The Doppler width of a transition between non-Rydberg levels is used to measure the gas temperature. The gas density is significantly reduced in the abnormal glow discharge due to ion charge exchange heating. Electric field maps and gas density measurements are combined with an analytic treatment of ion transport in the cathode-fall region to determine the current balance or ratio of ion to electron current at the cathode. This current balance is 3.3 and is nearly independent of total discharge current. The densities of He $2\,^1S$ and $2\,^3S$ metastables are mapped using laser-induced fluorescence and laser absorption spectroscopy for absolute calibration. An analysis of the metastable maps provides absolute metastable production rates in the cathode-fall and negative-glow regions and provides a constraint on the density and temperature of the low-energy electrons in the negative glow. The constraint arises from our observation of a suppression of the $2\,^1S$ metastable density in the negative glow. This suppression is due to metastable spin conversion by low-energy electron collisions in the negative glow.

The empirical current balance at the cathode surface and the metastable production rates are compared to theoretical results from Monte Carlo simulations of electron avalanches. A Monte Carlo code, based on the null collision technique for nonuniform fields as developed by Boeuf and Marode, is used to simulate electron avalanches. The agreement between the empirical current balance and the result of Monte Carlo simulations is good. The inclusion of an anisotropic angular distribution for ionizing collisions results in excellent agreement, even in the highly abnormal cathode-fall region where $E/N$ reaches 3000 Td. The agreement between the empirical metastable production rates and the results of Monte Carlo simulations is good.

The high density of low-energy electrons in the negative glow suggests a simple model for the negative glow and suggests the existence of field reversal at the bound-

ary between the cathode-fall and negative-glow regions. The empirical constraint on the density and temperature of the low-energy electrons in the negative glow is combined with an ionization rate predicted by Monte Carlo simulations to determine the density and temperature of the low-energy electrons.

The agreement of the empirical results and results from Monte Carlo simulations lead us to conclude that excitation and ionization, as embodied in the current balance, are quantitatively understood in the cold cathode He discharge. The agreement indicates that the vast majority of ions striking the cathode are produced in the cathode-fall region. The discharge current is carried almost entirely by beam electrons at the cathode-fall negative-glow boundary.

A quantitative microscopic picture of the cathode-fall and negative-glow regions is emerging, but major challenges remain. A major experimental challenge is to measure the relative importance of, and coefficients for, electron emission from the cathode due to ion, metastable atom, and vuv photon bombardment. The measurements should be done *in situ* with a relatively nonperturbing

spectroscopic diagnostic. We believe that the spatial and temporal characteristics of carefully chosen optogalvanic effects will provide this information on electron emission. A convincing and fully self-consistent analysis of the optogalvanic effect will likely be difficult. Another experimental challenge is to perform independent measurements of the density and temperature of the low-energy electrons in the negative-glow region. Again, it should be possible to make the measurements with a relatively nonperturbing spectroscopic diagnostic. On the theoretical side there are many challenges. The ultimate goal is to develop relatively simple, efficient models which provide fully self-consistent fields. The models must also have good microscopic detail and absolute accuracy.

## ACKNOWLEDGMENTS

[1]P. Segur, M. Yousfi, J. P. Boeuf, E. Marode, A. J. Davies, and J. G. Evans, in *Electrical Breakdown and Discharges in Gases*, Vol. 89A of *NATO Advanced Study Institute, Series B: Physics*, edited by E. E. Kunhardt and L. H. Luessen (Plenum, New York, 1983), p. 331.

[2]W. H. Long, Northrup Research and Technology Center, Technical Report No. AFAPL-TR-79-2038, 1978. (Available as Doc. No. ADA 070 819 from the National Technical Information Service, Springfield, VA 22161.)

[3]J. E. Lawler, D. K. Doughty, E. A. Den Hartog, and S. Salih, in *Radiative Processes in Discharge Plasmas*, Vol. 149 of *NATO Advanced Study Institute, Series B: Physics*, edited by J. M. Proud and L. H. Luessen (Plenum, New York, 1986), p. 525.

[4]M. Ohuchi and T. Kubota, J. Phys. D **16**, 1705 (1983).

[5]P. Bayle, J. Vacquie, and M. Bayle, Phys. Rev. A **34**, 360 (1986); **34**, 372 (1986).

[6]K. G. Emeleus, J. Phys. D **14**, 2179 (1981).

[7]K. Kumar, Phys. Rep. **112**, 319 (1984).

[8]J. Dutton, J. Phys. Chem. Ref. Data **4**, 577 (1975).

[9]T. J. Moratz, L. C. Pitchford, and J. N. Bardsley, J. Appl. Phys. **61**, 2146 (1987).

[10]K. Kitamori, H. Tagashira, and Y. Sakai, J. Phys. D **11**, 283 (1978).

[11]E. J. Lauer, S. S. Yu, and D. M. Cox, Phys. Rev. A **23**, 2250 (1981).

[12]M. A. Folkard and S. C. Haydon, Aust. J. Phys. **24**, 527 (1971).

[13]J. H. Ingold, in *Gaseous Electronics*, edited by M. N. Hirsch and H. J. Oskam (Academic, New York, 1978), Vol. I, p. 24.

[14]K. G. Muller, Z. Phys. **169**, 432 (1962).

[15]L. Friedland, J. Phys. D **7**, 2246 (1974).

[16]D. K. Doughty and J. E. Lawler, Appl. Phys. Lett. **45**, 611 (1984).

[17]J. P. Boeuf and E. Marode, J. Phys. D **15**, 2169 (1982).

[18]C. A. Moore, G. P. Davis, and R. A. Gottscho, Phys. Rev. Lett. **52**, 538 (1984).

[19]D. K. Doughty, S. Salih, and J. E. Lawler, Phys. Lett. **103A**, 41 (1984).

[20]R. Warren, Phys. Rev. **98**, 1650 (1955).

[21]B. N. Ganguly and A. Garscadden, Appl. Phys. Lett. **46**, 540 (1985).

[22]M. L. Zimmerman, M. G. Littman, M. M. Kash, and D. Kleppner, Phys. Rev. A **20**, 2251 (1979).

[23]C. E. Moore, *Atomic Energy Levels*, Natl. Bur. Stand. Ref. Data Ser., Natl. Bur. Stand. (U.S.) Circ. No. 35 (U.S. GPO, Washington, D.C., 1971).

[24]A. R. Edmonds, J. Picart, N. Tran Minh, and R. Pullen, J. Phys. B **12**, 2781 (1979).

[25]D. K. Doughty and J. E. Lawler, Phys. Rev. A **28**, 773 (1983).

[26]D. K. Doughty and J. E. Lawler, Appl. Phys. Lett. **42**, 234 (1983).

[27]T. F. Gallagher, S. A. Edelstein, and R. M. Hill, Phys. Rev. A **15**, 1945 (1977).

[28]W. L. Wiese, M. W. Smith, and B. M. Glennon, *Atomic Transition Probablities*, Natl. Bur. Stand. Ref. Data Ser., Natl. Bur. Stand. (U.S.) Circ. No. 4 (U.S. GPO, Washington, D.C., 1966), Vol. I.

[29]B. N. Ganguly, J. R. Shoemaker, B. L. Preppernau, and A. Garscadden, J. Appl. Phys. **61**, 2778 (1987).

[30]The pressure-broadening coefficient of 42.0 ± 2.7 MHz/Torr at 292 K for the 501.6-nm transition is from J. E. Lawler, Ph.D. thesis, University of Wisconsin, 1978.

[31]J. E. Lawler, Phys. Rev. A **32**, 2977 (1985).

[32]G. H. Wannier, *Statistical Physics* (Wiley, New York, 1966), p. 402.

[33]F. W. J. Olver, in *Handbook of Mathematical Functions*, edited by M. Abramowitz and I. A. Stegun (Dover, New York, 1964), pp. 376 and 416.

[34]M. Abramowitz, in *Handbook of Mathematical Functions*, edited by M. Abramowitz and I. A. Stegun (Dover, New York, 1964), pp. 498 and 501.

[35]G. Arfken, *Mathematical Methods for Physicists* (Academic, New York, 1985), p. 897.

[36]H. Helm, J. Phys. B **10**, 3683 (1977).

[37]S. Sinha, S. L. Lin, and J. N. Bardsley, J. Phys. B **12**, 1613 (1979).

[38]H. F. Wellenstein and W. W. Robertson, J. Chem. Phys. **56**, 1072 (1972); **56**, 1077 (1972).

[39]A. V. Phelps, Phys. Rev. **99**, 1307 (1955).

[40]R. A. Buckingham and A. Dalgarno, Proc. R. Soc. London, Ser. A **213**, 506 (1952).

[41]D. C. Allison, J. C. Browne, and A. Dalgarno, Proc. Phys. Soc. London **89**, 41 (1966).

[42]R. W. LaBahn and J. Callaway, Phys. Rev. A **2**, 366 (1970); Phys. Rev. **180**, 91 (1969); **188**, 520 (1969).

[43]G. D. Alkhazov, Zh. Tekh. Fiz. **40**, 97 (1970) [Sov. Phys.— Tech. Phys. **15**, 66 (1970)].

[44]D. A. Doughty, E. A. Den Hartog, and J. E. Lawler, Phys. Rev. Lett. **58**, 2668 (1987).

[45]A. V. Phelps and L. C. Pitchford, Phys. Rev. A **31**, 2932 (1985).

[46]M. J. Druyvesteyn and F. M. Penning, Rev. Mod. Phys. **12**, 87 (1940).

[47]P. F. Little and A. von Engel, Proc. R. Soc. London, Ser. A **224**, 209 (1954).

[48]R. D. Rundel, F. B. Dunning, J. S. Howard, J. P. Riola, and R. F. Stebbings, Rev. Sci. Instrum. **44**, 60 (1973).

[49]W. C. Fon, K. A. Berrington, P. G. Burke, and A. E. Kingston, J. Phys. B **14**, 2921 (1981).

[50]R. Deloche, P. Monchicourt, M. Cheret, and F. Lambert, Phys. Rev. A **13**, 1140 (1976).

APPENDIX D    (Pg. 49-52)

PHYSICAL REVIEW LETTERS

# Electron Temperature and Density Diagnostics in a Helium Glow Discharge

E. A. Den Hartog, T. R. O'Brian, and J. E. Lawler

*Physics Department, University of Wisconsin, Madison, Wisconsin 53706*

(Received 1 December 1988)

Two laser-based diagnostics are used to determine the density $(n_e)$ and temperature $(T_e)$ of low-energy electrons confined in the negative glow of a dc helium glow discharge. Each diagnostic yields an independent relation between $n_e$ and $T_e$. From the intersection of these relations we find that $n_e = 5 \times 10^{11}$ cm$^{-3}$ and $k_B T_e = 0.12$ eV for an abnormal cathode fall of 261 V in 3.50-Torr helium.

The negative-glow region of a dc glow discharge is characterized by a weak electric field and a high density of charged particles. This plasma is sustained by a low density of high-energy "beam" electrons which stream through the negative glow from the cathode fall region, causing excitation and ionization. The bulk of the electrons in the negative glow are low energy ($< 1.0$ eV) and are held in the negative glow by a weak potential-energy well.[1] It is a common method to treat the electron energy distribution function as the sum of a Maxwellian describing the high density of low-energy electrons and a weak high-energy tail.[2]

In this Letter we describe a pair of laser-based diagnostics which together yield $n_e$ and $T_e$ for the low-energy electrons in the negative glow. Each diagnostic provides an independent relation between $n_e$ and $T_e$. The first diagnostic, based on the endothermic electron collisional transfer between low Rydberg levels, yields a relation in which $n_e$ decreases with increasing $T_e$. The second diagnostic, which has been reported previously,[1] is based on the spin conversion of helium metastables,

$$\text{He}\,(2\,^1S) + e^- \rightarrow \text{He}\,(2\,^3S) + e^- + 0.79\,\text{eV}. \quad (1)$$
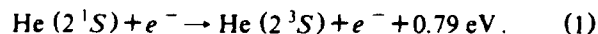
This diagnostic is based on an exothermic process and yields a relation in which $n_e$ increases with increasing $T_e$. The intersection of these two relations yields the density and temperature of the low-energy electrons in the negative glow.

In the Rydberg-atom experiment a low Rydberg level is selectively populated with a laser. The electron collisional transfer rate from the level populated with the laser to a higher-lying Rydberg level is determined by measuring the ratio of the laser-induced fluorescence (LIF) signals from the two levels. Although high Rydberg levels do not survive sufficiently long to fluoresce in a typical discharge, low Rydberg levels do fluoresce. This rate can be written as the product of $n_e$ and a rate coefficient which depends on $T_e$, thus determining a relationship between $n_e$ and $T_e$.

A detailed description of the apparatus appears elsewhere.[1] The discharge used in this study is produced between flat circular aluminum electrodes 3.2 cm in diameter and separated by 0.62 cm. The electrodes are water

cooled to minimize gas heating. For discharge operation ultrahigh-purity (0.999 999) helium is slowly flowed through the system. A capacitive manometer monitors the pressure which is maintained at 3.50 Torr. The measurements reported in this Letter were made with a discharge current density of 0.846 mA/cm$^2$ corresponding to an abnormal cathode fall of 261 V.

The laser used is a pulsed, N$_2$-laser-pumped, narrow-band (0.2 cm$^{-1}$) dye laser, which is tunable over a wavelength range 360–700 nm. Frequency-doubling crystals are used to extend this range so that Rydberg levels may be excited out of the $2\,^3S$ metastable level. A cylindrical lens is used to focus the frequency-doubled light between the electrodes giving a spatial resolution of $\sim 0.2$ mm. Spatial maps are made by translating the discharge on a precision translation stage.

Laser-induced fluorescence is collected in a direction mutually perpendicular to both the laser axis and the discharge axis. A lens is used to focus the fluorescence onto the 0.25-mm slits of a compact (0.2 m) monochromator which is used to isolate the desired fluorescence. The light is detected with a photomultiplier tube. The photomultiplier signal is amplified 100× and recorded with a Transiac 2001S digitizer with a 4100 averaging memory interfaced with an IBM PC.

Rydberg levels with the same principal quantum number "$n$" but different "$l$" are highly coupled by neutral collisions at 3.5 Torr. Excitation of the $np$ level is effectively excitation of the entire $n$ manifold with the populations of the various orbital angular-momentum levels being proportional to their degeneracy. The collisional transfer rate between two Rydberg manifolds is determined by measuring the ratio of their LIF signals when the lower-lying manifold is populated with the laser. Three such collisional transfer rates are studied. When the laser is tuned to the $2\,^3S$-$5\,^3P$ transition, fluorescence from $5\,^3D$-$2\,^3P$ and $6\,^3D$-$2\,^3P$ transitions is mapped, yielding the $n = 5$ to 6 collisional transfer rate. When the laser is tuned to the $2\,^3S$-$6\,^3P$ transition, fluorescence from the $6\,^3D$-$2\,^3P$, $7\,^3D$-$2\,^3P$, and $8\,^3D$-$2\,^3P$ transitions is mapped yielding both the $n = 6$ to 7 and $n = 6$ to 8 collisional transfer rates. Figure 1 shows a map of the ratio of LIF from $n = 7$ to that from $n = 6$,
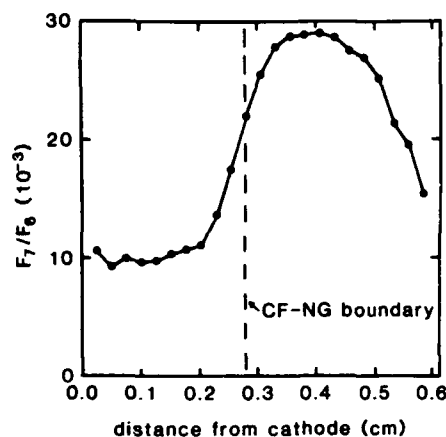
FIG. 1. Ratio of LIF signal from $n=7$ to that from $n=6$ vs distance from the cathode.
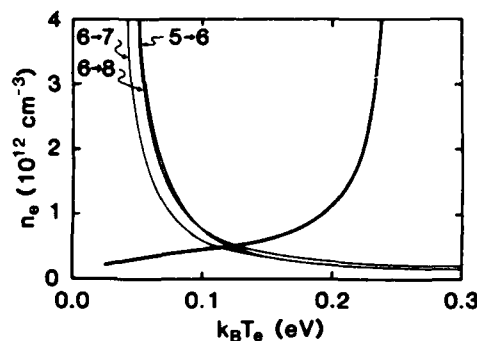


FIG. 2. Electron density vs electron temperature for the low-energy electrons in the negative glow. The three light lines arise from the Rydberg-atom diagnostic. The bold line arises from the metastable analysis.

when $n=6$ is populated with the laser. The position at which the cathode-fall field extrapolates to zero is indicated on the plot by a vertical dashed line. This is the cathode-fall–negative-glow (CF-NG) boundary. The enhancement of $n=7$ fluorescence to the right of this boundary is due to low-energy electron collisions in the negative glow.

The short duration (3 nsec) laser pulse produces an initial excess population $N_n(0)$ in the manifold having principal quantum number $n$. The decay is described by a single exponential because of the weak coupling between adjacent manifolds. The decay rate, $\tau_n^{-1}$, includes both collisional and radiative processes. Under the same conditions the population $N_{n'}(t)$ of a higher-lying manifold $n'$ is described by the rate equation

$$dN_{n'}(t)/dt = -N_{n'}(t)/\tau_{n'} + R_{nn'}N_n(t),$$

where $\tau_{n'}^{-1}$ is the depopulation rate of the $n'$ manifold and $R_{nn'}$ is the rate for collisional transfer from manifold $n$ to $n'$, including both neutral and electron collisions. The solution to this equation is

$$N_{n'}(t) = \frac{R_{nn'}N_n(0)}{\tau_{n'}^{-1} - \tau_n^{-1}} (e^{-t/\tau_n} - e^{-t/\tau_{n'}}).$$

The ratio of time-integrated fluorescence from the $n'$

TABLE I. Measured quantities $\tau_{n'}$ and $R_{nn'}$ for the three collisional transfer processes studied. The last column is the excitation transfer rate due to low-energy electron collisions in the negative glow.

| $n \to n'$ | $\tau_{n'}$ $(10^{-9}$ sec) | $(R_{nn'})_{cf}$ $(10^5$ sec$^{-1})$ | $(R_{nn'})_{ng} - (R_{nn'})_{cf}$ $(10^5$ sec$^{-1})$ |
|---|---|---|---|
| $5 \to 6$ | 29.1 | 2.0 | 3.5 |
| $6 \to 7$ | 30.8 | 6.0 | 11.1 |
| $6 \to 8$ | 33.9 | 1.2 | 4.6 |

manifold to that from the $n$ manifold is

$$\frac{F_{n'}}{F_n} = \frac{A_{n'd-2p}\int N_{n'}(t)dt/(n')^2}{A_{nd-2p}\int N_n(t)dt/n^2},$$

where $A$ is a transition probability for a $d \to 2p$ transition and the observed fluorescence transitions are optically thin. After substituting and carrying out the integrals, $F_{n'}/F_n$ is given by

$$\frac{F_{n'}}{F_n} = \frac{n^2 A_{n'd-2p} R_{nn'}\tau_{n'}}{n'^2 A_{nd-2p}}.$$

This relation expresses the collisional transfer rate in terms of the measured ratio of fluorescence.

The manifold lifetime $\tau_{n'}$ is measured in situ. This is done by driving the $2\,^3S$-$n'\,^3P$ transition with the laser and collecting $n'\,^3D$-$2\,^3P$ fluorescence as described for the fluorescence mapping. The fluorescence decay is time resolved using a PAR 162/163 scanning boxcar integrator and plotted. Table I shows the results of measurements of $\tau_{n'}$ and the measured $R_{nn'}$ for the three different $n \to n'$ excitation transfers being studied. Because of the spatial asymmetry, the values of $R_{nn'}$ are quoted separately for the cathode fall and for the difference between the peak negative-glow signal and cathode fall. The electron density is negligible in the cathode fall and so $(R_{nn'})_{cf}$ is interpreted as the collisional transfer rate due to neutral collisions. The neutral transfer rate will be uniform throughout the discharge because the neutral density is uniform. The excitation transfer rate attributable to low-energy electrons in the negative glow is the difference between the rate in the negative glow and that in the cathode fall: $(R_{nn'})_{ng} - (R_{nn'})_{cf}$.

The measured electron collisional transfer rate can be expressed as the product of a temperature-dependent rate coefficient and the electron density $n_e$. We use the analytical formula given by Vriens and Smeets[3] for the rate coefficient. The resulting relations between electron density and temperature are shown as the thin lines in Fig. 2 for each of the collisional transfer rates measured.

The metastable-atom diagnostic is carried out under the same discharge conditions as the Rydberg-atom diagnostic. The $2\,^1S$ and $2\,^3S$ metastable densities are measured as functions of axial position in the discharge. The diagnostic is based on the observed suppression of $2\,^1S$ metastables in the negative glow due to the metastable spin conversion reaction of Eq. (1). An analysis of metastable transport and kinetics in the discharge yields a net rate for the above reaction. From this rate a second relation between $n_e$ and $T_e$ is determined.

The metastable density measurements are made in two steps: (1) LIF is used to make maps of relative metastable densities, and (2) absorption measurements are made to put absolute scales on the density maps. The $2\,^1S$ metastables are mapped by driving the $2\,^1S$-$3\,^1P$ transition at 501.6 nm with the laser and observing $3\,^1D$-$2\,^1P$ fluorescence at 667.8 nm. The $2\,^3S$ metastables are mapped by driving the $2\,^3S$-$3\,^3P$ transition at 388.9 nm with the laser and observing $3\,^3S$-$2\,^3P$ fluorescence at 706.5 nm. These laser transitions do not require frequency doubling. The collimated laser is incident on a 0.25-mm slit which is imaged 1:1 into the discharge. Fluorescence collection and signal processing is much the same as for the Rydberg-atom experiment with the substitution of interference filters for the monochromator as a spectral filter.

The laser absorption measurements, needed for determining an absolute scale for the density maps, are made using the same laser transitions as the LIF measurements. The laser bandwidth is reduced to 500 MHz by introduction of an etalon. Absorption measurements are made at the peak of the spatial profile with 0.50-mm resolution. Saturation of the transition is avoided by reducing the laser power with neutral density filters. The transmitted laser intensity is monitored with a photodiode detector. The photodiode signal is processed with a boxcar averager and plotted on a strip-chart recorder as the laser frequency is scanned through the transition. Metastable densities are determined from the integral over frequency of the natural log of the transmittance. Ten absorption measurements are averaged to determine each density. The results of the metastable density measurements are shown as points in Fig. 3.

The metastable maps are analyzed to determine the net rate of metastable spin conversion. The transport and kinetics of $2\,^1S$ and $2\,^3S$ metastables in the discharge are modeled using a pair of balance equations which are coupled differential equations,

$$D_s \frac{\partial^2 M_s}{\partial z^2} - \beta M_s^2 - \beta M_s M_t - \gamma M_s N - \kappa n_e M_s + P_s = 0,$$

$$D_t \frac{\partial^2 M_t}{\partial z^2} - \beta M_t^2 - \beta M_s M_t + \kappa n_e M_s + P_t = 0,$$

where $M_{s,t}$ is the metastable density, $N$ is the density of ground-state atoms, $n_e$ is the density of low-energy electrons, $D$ is the diffusion coefficient, $P$ is the production
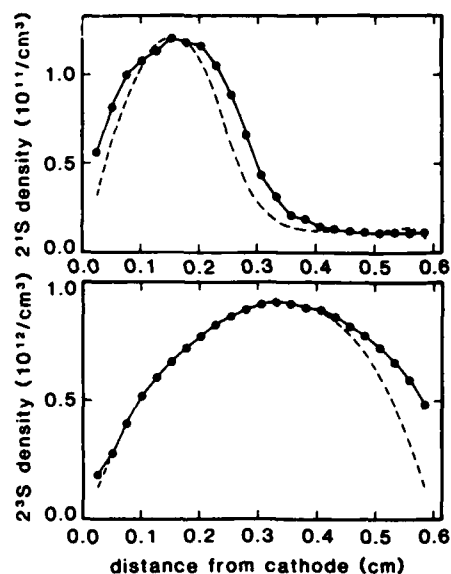


FIG. 3. $2\,^1S$ and $2\,^3S$ metastable densities vs distance from the cathode. The points are experimental measurements. The dashed curves are calculated densities using the fitting process described in the text.

rate per unit volume, $\gamma$ is the rate constant for singlet metastable destruction due to collisions with ground-state atoms, $\beta$ is the rate constant for the destruction of metastables due to metastable-metastable collisions, $\kappa$ is the rate constant for net destruction of singlet metastables due to low-energy electron collisions, and $s$ and $t$ subscripts indicate singlet and triplet metastables, respectively.[1] The first three loss terms in each equation are loss terms arising from diffusion and collisions between metastables. There is an additional loss term in the singlet equation arising from collisions with ground-state atoms. The fifth loss term in the singlet equation is due to the metastable spin conversion reaction (1) and a corresponding gain term is included in the triplet equation. Values of $DN$, $\gamma$, and $\beta$ are taken from Phelps.[4] The temperature dependence of $D$ is taken from Buckingham and Dalgarno[5] and that of $\gamma$ is taken from Allision, Browne, and Dalgarno.[6]

The coupled equations are solved numerically for $M_s(z)$ and $M_t(z)$ and compared with the experimental results. In the calculation the spatial dependence of $n_e$ is assumed to be a step function: zero in the cathode fall and uniform in the negative glow. The spatial dependence of the production terms is determined in Monte Carlo simulations to approximate a fundamental diffusion mode. Diffusion modes up to tenth order are included in the solutions to describe the spatial asymmetry of the $2\,^1S$ metastables. The values of $P_s$, $P_t$, and $\kappa n_e$ are varied until a good fit to the experimental metastable maps is obtained. The dashed curves of Fig. 3 are the calculated metastable densities determined in this manner. By this method, $\kappa n_e$ is found to be $7.0 \times 10^4$ sec$^{-1}$.

The rate constant $\kappa_m$ for metastable spin conversion by room-temperature electrons was measured by Phelps.[4] The temperature dependence of the rate constant is $(T_e)^{-1/2}$ because the cross section scales as the inverse of the electron energy.[7] The $\kappa n_e$ determined from the metastable analysis must be considered an effective rate for metastable spin conversion since it accounts for both forward and reverse contributions of reaction (1). Setting $\kappa n_e$ equal to the expression for the forward rate minus the reverse rate we obtain

$$\kappa n_e = n_e [\kappa_m (0.025 \text{ eV}/k_B T_e)^{1/2} - (M_t/3M_s)\kappa_m (0.025 \text{ eV}/k_B T_e)^{1/2} \exp(-0.79 \text{ eV}/k_B T_e)] .$$

This expression yields a second relation between $n_e$ and $T_e$ which is shown as the bold line in Fig. 2. The intersection of the two relations yields $n_e = 5 \times 10^{11}$ cm$^{-3}$ and $k_B T_e = 0.12$ eV for the electrons in the negative glow of a 261-V, 0.846-mA/cm$^2$ discharge in 3.50-Torr helium.

The uncertainty in the metastable-atom diagnostic is due mainly to neglect of the $2\,^1P$-$2\,^1S$ collisional-radiative coupling in the negative glow. Including this rather complex coupling could shift the curve from the metastable experiment to higher electron density, but this effect will be no greater than a factor of 2.[1,8] Assuming a factor of 2 uncertainty in the electron–Rydberg-atom rate coefficient also, then $n_e$ will be between $4 \times 10^{11}$ and $1 \times 10^{12}$ cm$^{-3}$, and $k_B T_e$ will be between 0.07 and 0.16 eV. There are good prospects for improved knowledge of such rate coefficients.

Although the diagnostic based on the metastables may have limited applicability, it does have the distinct advantage that only electron collisions can couple the singlet and triplet He metastables. The Rydberg-atom diagnostic is broadly applicable since all atoms have Rydberg levels, and the level spacing may be chosen appropriately for the electron temperature of interest. Both laser-based diagnostics are noninvasive diagnostics and can provide good spatial and temporal resolution. They should be very useful in studying the structure of glow-discharge sheaths.

[1]E. A. Den Hartog, D. A. Doughty, and J. E. Lawler, Phys. Rev. A **38**, 2471 (1988).

[2]Yu M. Kagan, C. Cohen, and P. Avivi, J. Appl. Phys. **63**, 60 (1988).

[3]L. Vriens and A. H. M. Smeets, Phys. Rev. A **22**, 940 (1980).

[4]A. V. Phelps, Phys. Rev. **99**, 1307 (1955).

[5]R. A. Buckingham and A. Dalgarno, Proc. Roy. Soc. London A **213**, 506 (1952).

[6]D. C. Allison, J. C. Browne, and A. Dalgarno, Proc. Phys. Soc. London **89**, 41 (1966).

[7]W. C. Fon, K. A. Berrington, P. G. Burke, and A. E. Kingston, J. Phys. B **14**, 2921 (1981).

[8]E. A. Den Hartog, Ph.D. thesis, University of Wisconsin–Madison, 1989 (unpublished).

APPENDIX E    (Pg. 53-63)

# Self-consistent kinetic model of the cathode fall of a glow discharge

T. J. Sommerer

*Department of Physics, University of Wisconsin, Madison, Wisconsin 53706*

W. N. G. Hitchon

*Department of Electrical and Computer Engineering, University of Wisconsin, Madison, Wisconsin 53706*

J. E. Lawler

*Department of Physics, University of Wisconsin, Madison, Wisconsin 53706*

The electrons in the cathode-fall (CF) region of a helium dc glow discharge have been modeled at the kinetic level with a self-consistent electric field using a "convective-scheme" (CS) (propagator or Green's-function) solution method. The CS is both straightforward to implement and numerically efficient. CS electron calculations using one spatial and two velocity variables are shown to match Monte Carlo simulations of swarms in uniform $E/N$ and in the CF. The CS predictions are also shown to match experimental swarm results. A self-consistent CF solution is obtained through a slow relaxation of the electric field to that indicated by Poisson's equation. The electric field configuration as predicted by the CS agrees well with optogalvanic measurements. The discussion emphasizes both the physical nature of, and the difficulties associated with, a self-consistent-field calculation.

## I. INTRODUCTION

Interest in modeling glow-discharge properties has increased with the application of glow discharges to plasma processing. Understanding of the cathode fall (CF) is crucial to a global understanding of the discharge, as this region largely determines the stability of the discharge and the details of many plasma processes.

Efforts to model the CF are hampered by the lack of hydrodynamic equilibrium in the region due to the relatively strong electric field gradients and the presence of the cathode, which both absorbs and emits particles. Nonhydrodynamic conditions call into question the use of ionization and diffusion coefficients,[1] which are measured in swarm experiments at very low current densities and in spatially invariant electric fields. The absolute electron number density scales out of the solution when an *a priori* electric field is imposed and the behavior of other charged species is ignored, as is done in many Monte Carlo simulations. In contrast, a fully kinetic solution of the electron behavior in the cathode-fall region eliminates the use of empirical coefficients, and a self-consistent-field calculation couples the behavior of all charged species into the problem through Poisson's equation.

An overall approach to a self-consistent model of the CF region has been described in a previous paper.[2] There, a simple distribution function was assumed, and two moment equations, together with Poisson's equation, were integrated to demonstrate the validity of the proposed framework. This work implements a kinetic description of the electrons within a similar framework. The kinetic description is based on the convective scheme (CS), which is introduced to gaseous electronics in this paper.

This paper will begin with a brief discussion of several methods that have been used to model weakly ionized plasmas. In this way the CS will be couched in terms of more familiar approaches. The strengths and weaknesses of these methods will be discussed, as well as the similarities and differences between these approaches and the CS. The formal CS solution will then be presented in Sec. III. This section has a brief calculation to illustrate the gain in efficiency of the CS over an explicit finite difference calculation and presents a useful near-steady-state approximation. Section IV will then step through the essentials of a simplified CS example in two dimensions. This model is presented for pedagogical purposes, but would also be a most realistic model of ion transport when charge exchange collisions dominate. This is followed by a detailed description of a more sophisticated CS implementation in three independent variables, a model appropriate for the electrons in the CF of a helium dc glow discharge. A swarm in uniform $E/N$ and a CF calculation using fixed electric field configurations will then be presented and compared with Monte Carlo simulations and experimental results. Finally, a CF calculation with a self-consistent electric field will be presented and discussed in Sec. VI. Factors influencing the accuracy of the predicted electric field configuration will be discussed, along with some of the obstacles that must be overcome to allow a realistic negative glow (NG) model and a self-consistent electrode-to-electrode calculation.

## II. RELATED SOLUTION TECHNIQUES

The "convective scheme" (CS) presented here, which is based on a propagator or Green's-function method, combines aspects of a variety of techniques which have been applied to the CF problem. Details of the techniques relevant to the CS, along with recent or notable illustra-

tive published work, will now be discussed.

Fluid equations have been used extensively to model the cathode fall.[3,4] Three coupled differential equations are generated from the zero, first, and second velocity moments of Boltzmann's equation. No form of the distribution function is assumed; the first three moments of the distribution function are proportional to the number, momentum, and energy densities, respectively. However, fluid equations will not distinguish between various distribution functions as long as they have identical zero, first, and second moments. Fluid approaches can produce reasonable results, but errors associated with this approximation are difficult to estimate.

In a related approach which is computationally similar to fluid equations, a distribution function with $n$ free parameters is assumed and substituted into Boltzmann's equation. The first $n$ velocity moments of Boltzmann's equation are integrated to obtain $n$ coupled differential equations.[5] The authors used this technique to illustrate an overall method of tackling the CF.[2]

Segur and Keller[6] have manipulated Boltzmann's equation into a purely integral form and solved a CF problem with an imposed electric field. The method involves finding a matrix of "probability coefficients" for every electric field of interest and yielded results consistent with Boeuf and Marode's Monte Carlo results in the case of isotropic scattering.[7,8]

The method of explicit finite differences has been directly applied to Boltzmann's equation. The method has been used by Kitamori et al. to study relaxation properties of spatially invariant problems.[9] Time evolution information is available, as the calculation is iterated in time until a steady-state solution is found. The method is numerically intensive because of a stringent limit on the time step, the Courant-Friedrichs-Lewy (CFL) criterion.[10] The time step must be small enough that no particles in the calculation cross more than a single mesh in a time step $\Delta t$. The limit is numerical (depending upon the nature of the imposed numerical mesh) rather than physical (limited by some physical process), though the choice of mesh size was presumably based on physical grounds.

In principle, an explicit finite difference calculation could integrate the spatial coordinate $z$ away from a point where the velocity distribution is known, rather than iterating in the time variable. This would reduce the number of variables in a CF calculation by one. Finding such a point is problematic, and any changes to the electric field (such as occur during iteration to a self-consistent field) would require a recalculation of the entire distribution function for all $z$. An implicit finite difference calculation would not be restricted by the CFL constraint, but such a scheme relies heavily on the efficiency of solving tridiagonal matrix equations. Unfortunately, the collisions in the kinetic problem imply that the matrices are *not* tridiagonal, and much of the computational efficiency is lost.

Hybrids of these methods have been used extensively. A common hybrid is the expansion of the angular part of the distribution function of $l$ Legendre polynomials to obtain $l$ coupled differential equations.[11,12] The number of independent variables in Boltzmann's equation is thereby reduced at the expense of increasing the number of equations.

Monte Carlo simulations have been used to describe the electron behavior in the CF.[7,13,14] These simulations exactly track the kinetics of the sampled electrons, but self-consistent calculations demand good number density statistics at *all* spatial locations in the discharge. State-of-the-art Monte Carlo calculations[7] track each individual electron avalanche until the electrons hit an electrode, so no information is available on the time evolution of the discharge, and any adjustments of the electric field require a complete recalculation of the distribution. However, where the steady-state solution is important and good electric field and cross-section data are available, Monte Carlo simulations can generate results in excellent agreement with experiment.[15]

The CS to be presented here produces a distribution function which is a solution of the appropriate kinetic equation.[16] The CS is perhaps closest in spirit to particle-in-cell simulations, but no random numbers are needed. When the CS is used with small time steps, the CS is mathematically identical to the method of finite differences[16] (specifically, a donor cell or "up-streaming" method). Its implementation is very physical and intuitive, similar to a Monte Carlo scheme. It is a fully kinetic solution and therefore free of the errors that hamper fluid calculations and approaches that involve the assumption of a parametrized form of the distribution function. Unlike explicit finite differences, CS time steps are not restricted by the Courant-Friedrichs-Lewy criterion, but rather by the nature of the collisions. Specifically, the CS time step must be less than the smallest collision time in the energy range of interest. As implemented, the CS assumes no particles have undergone more than one collision during a time step, so inaccuracy arises once a time step becomes a large fraction of an average collision time (and a non-negligible fraction of particles have in reality undergone more than one collision during the time step).

## III. CONVECTIVE SCHEME

A general description of the CS method for systems of rate equations is given by Adams and Hitchon[17] and for kinetic equations by Hitchon et al.[16] The details of a particle mover for one space and one velocity variable are covered in Ref. 16. This paper will emphasize the generalizations necessary for a CF calculation—an additional velocity coordinate, a non-Cartesian phase space, a detailed treatment of the important electron-atom collision processes, and convergence to a self-consistent solution. This section outlines the formal CS solution, demonstrates the efficiency of the CS relative to finite difference calculations, and presents a near-steady-state approximation that simplifies scattering calculations.

### A. Formal solution

Formally, the CS requires the determination of the fraction $p$ of particles in a cell of phase space at $(r'',v'')$ that move to a new cell of phase space at $(r',v')$ after a
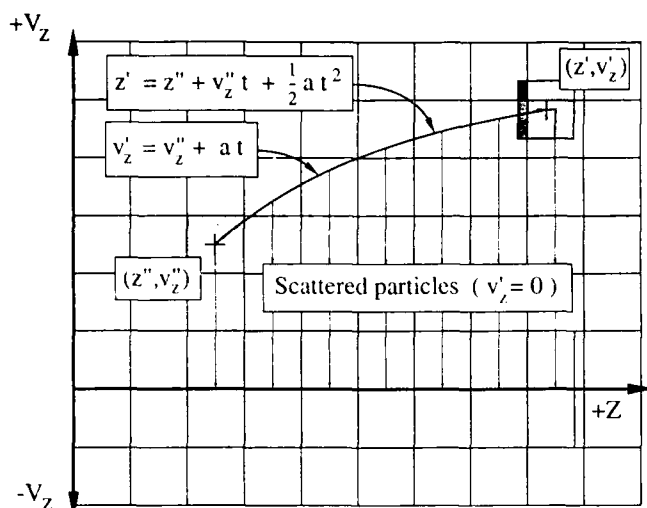
FIG. 1. Illustration of the ion convective scheme. Problem is one dimensional with two phase-space variables $z$ and $v_z$. Force (electric field) is assumed constant. Scattering shown is analogous to resonant ion charge exchange; particles completely stop after a collision. Note that the mesh straddles the $v_z = 0$ axis to avoid possible singularities.

time $\Delta t$ —the Green's function. (For consistency, doubly primed variables will always denote values *before* a movement or collision, and singly primed variables will label the values *after* the same.) Once this probability is known for all $(\mathbf{r}'', \mathbf{v}'')$ and $(\mathbf{r}', \mathbf{v}')$, the distribution of particles $f$ at an advanced time $t + \Delta t$ may be determined given the distribution at time $t$,

$$f(\mathbf{r}', \mathbf{v}', t + \Delta t) = \int d\mathbf{r}'' d\mathbf{v}'' p(\mathbf{r}', \mathbf{v}'; \mathbf{r}'', \mathbf{v}''; \Delta t)$$

$$\times f(\mathbf{r}'', \mathbf{v}'', t) . \tag{1}$$

When implemented on a numerical mesh, the integral becomes a sum over all cells of phase space in the mesh.

The task of evaluating $p$ may seem daunting until it is realized that only two mechanisms can remove particles from a particular cell of phase space in the kinetic problem.

(i) Unscattered particles in a cell will move along characteristic trajectories specified by the initial position $\mathbf{r}''$ and velocity $\mathbf{v}''$ associated with the cell, the electric field $\mathbf{E}$ along the trajectory, and the time step $\Delta t$.

(ii) Scattered particles will "jump" from the initial cell $(\mathbf{r}'', \mathbf{v}'')$ to a new cell at the same spatial location $(\mathbf{r}' = \mathbf{r}'')$ but with a new velocity $\mathbf{v}'$ defined by the nature of the collision.

These two processes are illustrated for a phase space with one spatial and one velocity coordinate in Fig. 1, which will be described in more detail in Sec. IV.

## B. Time step

The two particle-moving mechanisms outlined in Sec. III A can be implemented independently of each other provided that the distribution function changes on a time scale much longer than the time step and provided that

no particle undergoes more than one collision per time step. The latter condition can be approximately enforced by limiting the time step $\Delta t$ so that the fraction of particles that undergo two collisions in a time step is negligible,

$$[N\sigma_T(v)v\Delta t]^2 \ll 1 \tag{2}$$

for every speed $v$ of interest. The left-hand side of Eq. (2) is proportional to the error of the CS, but the full CS error is further reduced to the extent that scattering into a cell replaces scattering out of the cell.

The advantage of the CS over its finite difference cousin can then be seen by examining Fig. 2. Here, the mean collision time is plotted versus impact energy for electrons in the background gas of interest here (helium) at a density of $N = 11.2 \times 10^{16}$ cm$^{-3}$. The important feature of Fig. 2 is that the collision time minimizes at some energy (here around 80 eV) and then generally increases with increasing impact energy. This minimum governs the allowable CS time step; here we choose a time step of $\Delta t \ll 0.12$ ns consistent with the energies of a normal helium CF (up to 140 eV) and the neutral number density of interest. This CS time step does not change, even if electrons of very high energy are considered.

Contrast this time step limit with the Courant-Friedrichs-Lewy (CFL) criterion[10] that governs explicit finite difference methods: No particles may cross more than one cell in a time step. The limit applies to all independent variables in the problem; for a spatial variable $x$, even the fastest particles may not move more than the width of a single spatial cell $\Delta x$,

$$\Delta t_{CFL} < \Delta x / v_{max} . \tag{3}$$

In a kinetic calculation, the spatial grid spacing is chosen to be at most the order of the minimum mean free path $\lambda$: $\Delta x < \langle \lambda \rangle = \langle N\sigma_T(v) \rangle^{-1} \approx 0.012$ cm in this case. The total scattering cross section in $\sigma_T(v)$. With a maximum speed of interest $v_{max} \approx 7.0 \times 10^8$ cm/s, correspond-
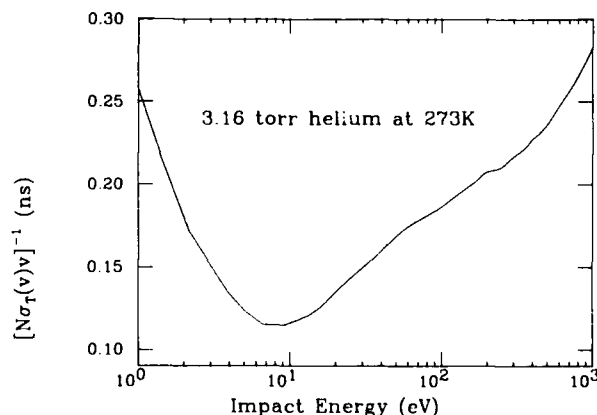


FIG. 2. Mean collision time for electrons in helium at $11.2 \times 10^{16}$ cm$^{-3}$ or 3.16 torr at 273 K. Minimum in the mean collision time within the energy range of interest governs the time step of the convective scheme.

ing to a normal CF potential energy in helium of around 140 V, the limiting time step from Eq. (3) is $\Delta t_{CFL} < 0.021$ ns. In practice, $\Delta t_{CFL} \ll 0.021$ ns unless a high-order scheme is used. Similar CFL limits exist for all other independent variables; for instance, the time step must also be limited to guarantee that no particles are accelerated through more than one cell in any velocity variable during $\Delta t$.

The advantage of the CS becomes even more apparent if electrons of higher energies are of interest, since $\Delta t_{CFL} \propto \tau_{max}^{-1/2}$, where $\tau_{max}$ is the maximum kinetic energy of interest, while the CS time step remains fixed.

### C. Nearly-steady-state approximation

An initial examination of the scattering shown in Fig. 1 might seem to imply that the spatial movement of the particles in the initial cell must be considered when the particles scattered out of the cell during the time step are reinserted into the mesh. This might be true if the number of particles in a cell varied greatly over a time step.

This complication is not necessary here. In this work, particles scattered out of a cell initially at $(r'', v'')$ are replaced at $(r' = r'', v')$ instead of being distributed along the same spatial trajectory that the initial cell traversed. The justification for this approximation rests upon the assumption that the number of particles at the initial location of the cell is roughly constant—particles may flow into and out of the cell during a time step, but in such a way as to approximately preserve the number of particles in the cell. The number of particles in a cell is certainly constant once a steady-state solution is obtained; provided the distribution changes on a time scale which is long compared to a time step, it is approximately true even during the transient solution. It would not be true, for example, if the CS were being used to study the expansion of a shock front, where particle densities vary greatly over a single spatial mesh cell and over a single time step.

### IV. CONVECTIVE-SCHEME IMPLEMENTATION

#### A. Two-dimensional example

A simplified but complete CS model will now be examined. This model would be entirely reasonable for ions in their parent gas (dominated by charge exchange), but is simple enough to be described in one figure (Fig. 1). For simplicity, a uniform electric field is assumed. A few terms will be defined to clarify the description of the CS. The CS requires a numerical mesh; some of the considerations in choosing a mesh will be described. The focus of this section is to step through an entire iteration (time step) of the CS.

To avoid confusion, the following naming convention will be observed for cells.

(i) The *initial* cell will refer to the cell in which the particles are initially located (either at the beginning of a time step or just prior to a collision). The size and shape of the cell in the phase space mesh is part of the specification of the initial cell. Particles within a cell are assumed to be uniformly distributed within the cell; that is, the phase-space density of a cell is assumed constant.

As previously mentioned, initial variables will be doubly primed.

(ii) The *moved* cell will refer to the location, size, and shape of the cell, after either a ballistic particle movement or just after a collision. The size, shape, and density of the moved cell may differ from that of the initial cell depending upon the nature of the phase space, and the moved cell does not, in general, correspond to any single cell of the mesh. The phase-space density of the moved cell is also assumed constant. Variables associated with the moved cell will be singly primed.

(iii) The *final* cells are those cells of the mesh that are overlapped by the moved cell. For example, the moved cell may be larger than the initial cell or a final cell due to phase-space considerations. The larger moved cell could then overlap many final cells.

The first step of a CS solution is to choose an appropriate phase-space mesh that can accurately describe the important physical processes. The considerations are much the same as for a finite difference solution method. Ions in their parent gas are dominated by charge exchange collisions; such ions simply stop after an ion-neutral collision in the cold gas approximation (resonant charge exchange), and no energy is directed into the transverse direction. If plane-parallel geometry is assumed, two variables are sufficient for the ions—the distance from the anode $z$, and the ion velocity along the discharge axis $v_z$.

A CS calculation is started by placing particles into the mesh; how this is done depends on the problem of interest. If the physical source of new ions is assumed spatially uniform and the ions start from rest, then new ions would be placed in the mesh in the cells corresponding to $\pm \Delta v_z / 2$ and uniformly distributed in $z$. The number of ions injected is determined from the ionization rate and the CS time step.

The CS now determines the fate of the ions in the mesh after a single time step $\Delta t$. As previously indicated, all particles are first moved as though no collisions occur. Then all collision rates are calculated and the scattered particles are redistributed.

The collisionless particle movement is a straightforward step and is shown for the ion phase space and a uniform electric field directed in the positive $z$ direction in Fig. 1. Each cell of the mesh is considered in turn. The location $z''$, and velocity $v_z''$ associated with the initial cell, combined with the electric field $E(z)$, and the time step $\Delta t$, completely specify the location $z'$ and velocity $v_z'$ of the moved cell. The equations shown in Fig. 1 assume a constant electric field: $E_0$, with an ion acceleration of $a = q_+ E_0 / m_+$, where $q_+$ is the ion charge and $m_+$ is the ion mass. The position of the moved cell after a time step $\Delta t$ is calculated, and the particles from the initial cell are distributed to final cells in proportion to the overlap of the moved cell with each of the four final cells. Realistic field configurations require a numerical integration. Each initial cell is examined in turn until all particles have been moved to their final positions.

The charge exchange collisions of this example are particularly easy to handle in the CS. Each cell of the mesh is examined in turn; the number of particles in a particu-

lar cell and the velocity associated with the cell are known. When combined with the neutral number density, the cross section, and the CS time step, the number of particles scattered out of the cell of interest can be found. These particles are removed from the initial cell and added to the two cells that straddle the $v_z = 0$ axis at the same spatial location (see Fig. 1). A nonzero background gas temperature could be handled by inserting the scattered ions with a Maxwellian velocity distribution. The scattering calculation is simplified by the fact that each cell of the mesh may be examined independently. Scattering rates are typically independent of spatial location and electric fields; in this case, the scattering probabilities can be calculated once for each velocity of interest on the mesh and then used for subsequent scattering calculations.

Once all cells of the mesh have been moved and then scattered, various moments of the distribution such as the number density and flux are calculated. If the calculation is self consistent, the electric field is recalculated. A new iteration is then started in this example by again injecting ions uniformly throughout the discharge in accordance with the assumed ionization rate.

### B. Three-dimensional electron model

A CS model of the electrons in a helium discharge will now be described, building upon the simpler ion model. The physical assumptions here are the same as described in Ref. 2. Briefly, the discharge is assumed to be plane parallel with negligible radial diffusion and an electric field directed along the axis of the discharge: $\mathbf{E} = E\hat{z}$. The positive $z$ axis points away from the cathode. This coordinate is reversed from that defined for the ions in Sec. IV A.

An adequate CS model of the electrons demands a realistic description of the angular scattering processes. An extra independent variable is therefore added to the model to describe motion transverse to the discharge axis. The independent variables are now the distance from the cathode $z$, the speed $v$, and $\mu$, the cosine of the angle $\theta$ between the velocity vector and the $z$ axis ($\mu = \cos\theta$). The discharge is azimuthally symmetric, so the azimuthal angle $\varphi$ does not appear.

A mesh equally spaced in speed (rather than energy) is chosen for good resolution of the low-energy particles. To improve numerical accuracy, the mesh is finer near $\mu = 1$ (forward-directed particles) than near $\mu = -1$ (backward-going particles). Specifically, a new integer variable $\xi$ which labels cells is introduced which has limits $0 < \xi < \xi_{max}$. Then $\mu$ at the boundary of the cells is calculated from $\mu = 1 - 2(\xi/\xi_{max})^2$. The electric field moves unscattered particles monotonically to higher $\mu$, and the use of the variable $\xi$ improves the resolution in the region near $\mu = 1$ in the mesh. (Note that this variation in mesh size is implemented with no difficulty, whereas the time step of a finite difference scheme would have to be reduced to accommodate the fine mesh near $\mu = 1$ and again ensure that no particles could transverse more than one of these smaller cells in a time step. Additional coding difficulties would also arise. The CS mesh size can be varied at will to more accurately describe regions of in-

terest with no such ill effects.)

As with the ion example, the electron CS calculation is started by placing electrons in the mesh. Here electrons are placed in the cells of the mesh immediately adjacent to the cathode with an assumed distribution function so as to satisfy a current balance condition at the cathode. The details of this injection are not important to the CS; they will be discussed later as part of the self-consistent calculations.

#### 1. Unscattered electrons

The ballistic movement of the electrons is more complex than that of the ions described previously. The complications arise out of the nature of the electron mesh, which has a variable Jacobian.

The ion CS model is considerably simplified by the fact that the ion phase space is Cartesian, and the size and shape of the cells do not change throughout the mesh. In general, the moved cell overlaps four final cells. The same cannot be said for the electron model; the Jacobian for this mesh is (approximately) $2\pi v^2$. A moved cell may fall completely within one final cell or may overlap many final cells. The CS accounts for this apparent variation in cell size by independently moving the center of each face of the initial cell to properly calculate the location and size of the moved cell. As before, the particles in the moved cell are distributed to each of the final cells in proportion to the volume of phase space occupied by the moved cell in each of the final cells.

#### 2. Scattered electrons

The scattering calculations for the electrons are illustrated in Fig. 3, and described here. All scattering processes are assumed isotropic, with the anisotropic differential elastic cross section being replaced with the
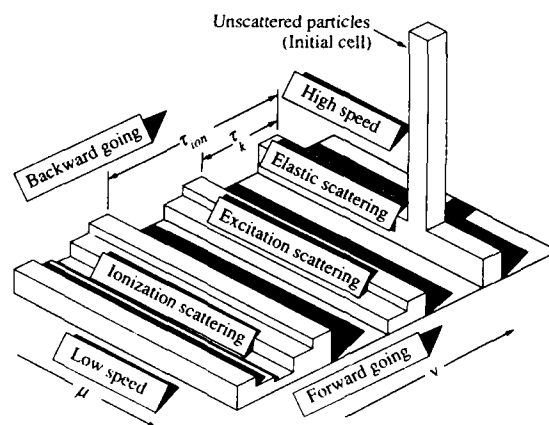


FIG. 3. Schematic of the electron collision operator. Electrons leaving a scattering event are distributed isotropically; anisotropic elastic scattering is described through the elastic momentum-transfer cross section. Electrons involved in an ionization event are distributed according to the differential energy scattering cross section. Ionization energy is $\tau_{ion}$. Excitation energy for the single process shown is $\tau_k$. Individual mesh cells have been omitted for clarity.

isotropic elastic momentum-transfer cross section. The assumption of isotropic inelastic scattering for electrons in a normal helium cathode fall is supported by the work of Den Hartog et al.[15] A detailed investigation of the effects of anisotropic scattering in nitrogen is presented by Phelps and Pitchford.[18] Although the present electron scattering calculations use isotropic scattering, it should be noted that any anisotropic distribution can be included in the CS.

The isotropic elastic momentum-transfer cross section is the simplest to examine. In this process, particles scatter from one polar angle $\mu''$ to another $\mu'$ at the same speed $(v'=v'')$. Particles scattered out within each cell $(z'',v'',\mu'')$ are replaced at the same spatial location $z'$ and speed $v'$ as the unscattered particles, but distributed evenly (isotropically) in the cosine of the polar angle $\mu'$.

Excitation collision processes are similar, but the scattered particles are replaced isotropically at a final speed $v'$ that is determined by the energy of the $k$th excitation process $\tau_k$: $v'^2=v''^2-2\tau_k/m$. The phase space of the electron mesh compresses as one moves toward lower velocities. This is again handled by calculating the positions of the faces of the moved cell when scattering from one speed $(v'')$ to another $(v')$; scattered particles lose a fixed energy $\tau_k$, rather than a fixed speed.

Ionization processes produce scattered particles over a range of speeds $0 \le v'^2 < v''^2 - 2\tau_{ion}/m$, where $\tau_{ion}$ is the ionization threshold energy. The number of particles scattered to each speed in this range is found using the differential energy ionization cross section. The scattered particles are then distributed isotropically as before.

As in the ion model, relevant moments of the distribution are calculated and (if self-consistent) the field is adjusted. As a final note, some moments are not found by integrating over the mesh. To improve the accuracy of finding moments like the average electron velocity $\langle v_z \rangle$ and the electron current density $j_e$, the electron flux across the $z$ boundaries within the mesh is tracked during the unscattered movement of electrons and used to calculate $\langle v_z \rangle$ and $j_e$.

## V. FIXED ELECTRIC FIELD CALCULATIONS

### A. Swarm experiment calculations

The CS is now used to model a swarm experiment in helium at a uniform reduced field of $E/N=282$ Td (where 1 Td $=10^{-17}$ V cm$^2$). The gas density $N$ is $3.53\times10^{16}$ cm$^{-3}$. The cross sections are taken from La-Bahn and Callaway[19] (elastic) and Alkhazov[20] (inelastic).

Figures 4(a)–4(d) show the predicted relative density $n$, the average $z$ velocity $\langle v_z \rangle$, the average electron energy $\langle \tau \rangle$, and the effective Townsend first ionization coefficient $\alpha$. The CS predictions are plotted, along with results from Doughty's Monte Carlo,[21] which uses the full anisotropic elastic scattering cross section. The Monte Carlo simulation should otherwise be directly comparable to the predictions of the CS.

The exact nature of the equilibration region near the cathode depends upon assumptions made about the dis-

tribution of electrons liberated from the cathode surface. A perfectly absorbing anode is assumed in both calculations, producing the observed absence of backscattered electrons near the anode. Assumptions about the nature of the electrode boundaries are common to both the CS and Monte Carlo methods, but do not affect the predicted swarm values.

Results from swarm experiments of Kücükarpaci et al.[22] are also displayed in Fig. 4. Kücükarpaci's results are in general agreement with an older but extensive set of swarm data compiled by Dutton.[23] Care has been taken to ensure a proper comparison of the average velocity $\langle v_z \rangle$ from the CS with the experimentally obtained drift velocity $v_d$. The average velocity attributed to Kücükarpaci in Fig. 4 was found using the drift velocity $v_d$, Townsend ionization coefficient $\alpha$, and longitudinal diffusion $D_L$ from Ref. 22,

$$\langle v_z \rangle = \frac{\Gamma}{n} = v_d - D_L\alpha \ . \tag{4}$$

The electron flux $\Gamma$ and density $n$ are well-defined moments.

The agreement of the predicted and experimental values is excellent. Kücükarpaci quotes an accuracy of $\pm5\%$ in $v_d$ and $\pm15\%$ in $D_L$ at this relative high $E/N$. The experimental uncertainties for $\alpha$ are larger; Dutton
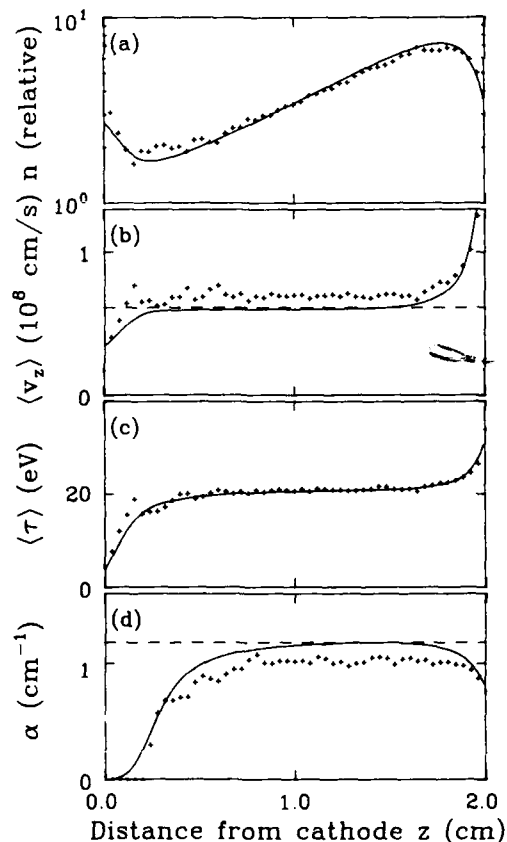
FIG. 4. Comparison of results of a swarm calculation. Solid lines denote the CS calculations and crosses are from the Monte Carlo calculation of Doughty (Ref. 21). Dashed lines indicate the experimental swarm values from Ref. 22 (see text).

discusses the problems in detail. The semiempirical inelastic cross sections from Alkhazov have an uncertainty of $\pm25\%$ at low impact energies and $\pm15\%$ at higher energies where the Born approximation is reliable. The differential elastic cross section from LaBahn and Callaway has an estimated accuracy of $\pm5\%$.

### B. Cathode fall

In this section the CS will be used to model the CF in the $j_D = 0.190$ mA cm$^{-2}$ near-normal glow discharge of Doughty et al.[24] and Den Hartog et al.[15]

An electric field configuration is imposed based on the field experimentally measured using optogalvanic detection of Rydberg atoms.[25] A linear field is assumed in the CF based on a least-squares fit to experimental electric field data.[15,24] The field is 897 V/cm at the cathode and extrapolates to zero at 0.382 cm from the cathode. The gas density is $11.2\times10^{16}$ cm$^{-3}$. A realistic model of the NG is beyond the scope of this paper, so a weak NG field was assumed (10 V/cm directed toward the cathode). This field configuration allows comparison with the Monte Carlo calculation, as the Monte Carlo calculation is unable to handle trapped particles (and therefore a field reversal). It also shortens the computation time required by sweeping electrons out of the NG region and into the anode.

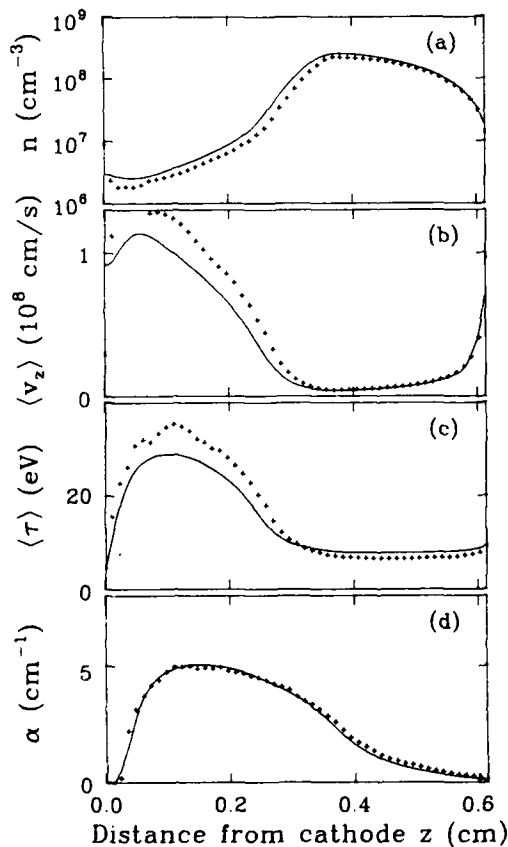A comparison of the results of the CS and Monte Carlo



FIG. 5. Comparison of results for a near-normal glow discharge from the CS and Doughty's Monte Carlo calculations (Ref. 21). The parameters and *imposed* electric field correspond to the $j_D = 0.190$ mA cm$^{-2}$ discharge of Ref. 24.

methods is shown in Fig. 5; the agreement here, as in the swarm calculations, is excellent. This fixed-field calculation should be an accurate indication of electron behavior in the CF. It should also be a reasonable model of the high-energy electrons that stream through the NG from the CF to the anode. It does not describe all of the NG electrons because the assumed NG field configuration does not allow a realistic anode sheath to form which would contain the highly mobile electrons within the NG plasma. A more detailed consideration of the NG will be presented along with the self-consistent CF calculations of Sec. VI C.

A brief review is in order. The CS method has been shown to accurately match the predictions of a fixed-field Monte Carlo code, where individual particle trajectories are followed exactly, unhampered by any mesh. Compared to an explicit finite difference solution, the CS algorithm is more efficient and free of numerical instabilities (it is inherently an integral, rather than a differential formulation). It is accurate *during* the time evolution of the system. Because the Green's function for the Boltzmann equation has an obvious interpretation, the CS method is very intuitive to implement, much in the spirit of Monte Carlo simulations.

## VI. SELF-CONSISTENT ELECTRIC FIELD

### A. Scope of solution

As mentioned in Sec. I, a self-consistent calculation of the CF demands an accurate description of all charged species. Here, singly charged ions (He$^+$) are assumed to be the only charged species present other than the electrons, and the ionic current is assumed to be the difference between the fixed discharge current and the electron current predicted by the CS [Eq. (6)]. Ion behavior is parametrized using the experimentally known mobility from Helm;[26] the details of this treatment and its justification in the CF are presented in Ref. 2.

Lawler[27] showed that the mobility parametrization of the ions should be adequate in the high-field part of the CF, but that the ion model is suspect near the CF-NG boundary. His calculations indicate that ions moving through rapidly changing fields (as exist near the CF-NG boundary) require several mean free paths to reach the speed indicated by the mobility, depending upon the actual field configuration and ionization source. The ion model does not describe the random thermal motion of the ions, which is important in low-field regions such as the NG. Because inertial effects are discounted, it cannot be expected to realistically model a possible field reversal in the discharge. The field must reverse somewhere in the discharge to allow the formation of an anode sheath and prevent a quick escape of NG electrons to the anode. Evidence placing the field reversal near the CF-NG boundary was recently reviewed by Den Hartog et al.[15] Microwave Doppler-shift measurements have indicated a slow ion drift toward the anode in the NG of a Kr-D$_2$ glow discharge,[28] indicative of a weak reversed field in the NG.

The numerical problems associated with a field reversal are strictly a function of the crude ion transport model.

A field reversal could be handled with ease if the CS were also used to describe the ions.

A self-consistent model of the CF-NG boundary and the NG will not be considered in this paper for several reasons. The physical assumptions appropriate in the NG differ markedly from those of the CF. Several mechanisms have been discounted in the present CS model of the CF that may be important in the NG, including energy transfer during elastic collisions, a nonzero neutral gas temperature, electron-ion recombination, Coulomb collisions, and the role of metastable atoms. A discussion of these and other mechanisms in a helium afterglow can be found in a comprehensive paper by Deloche *et al.*[29]

A more vexing problem is the physical time required to build up the large density of low-energy electrons existing in the NG. Recent experiments[15,30] on the $j_D = 0.190$ mA cm$^{-2}$ helium discharge being modeled here indicate a large density ( $\geq 10^{11}$ cm$^{-3}$) of relatively cold ( $\leq 0.25$ eV) electrons in the NG. If this density extends over 0.1 cm (around half) of the NG, $10^{10}$ electrons would exist in the NG per square centimeter of electrode area. If the source of these electrons is taken to be the electronic current crossing from the CF into the NG ($j_c = j_D = 0.190$ mA cm$^{-2}$ at the CF-NG boundary), and there are no losses (a best case assumption), it would take a minimum of $10^{-5}$ seconds for enough electrons to be generated in the discharge to obtain the observed NG electron density. Given the aforementioned CS time step of 0.05 ns (limited by the electron-atom collision rates in helium), this translates into a minimum of $2 \times 10^5$ CS iterations. A self-consistent electrode-to-electrode calculation must circumvent this problem.

### B. Boundary condition at the cathode

While the absolute number density in a fixed-field solution may be scaled arbitrarily by varying the number of injected electrons, absolute number densities are required in a self-consistent calculation for use in Poisson's equation. As previously indicated, the driving source in the CF is the secondary emission of electrons from the cathode by ion, metastable, and uv photon impact. The appropriate number of electrons to be launched in the present model is found using an effective emission coefficient $\gamma_p$, which determines the ratio of electron current density $j_e$ to ion current density $j_{ion}$ at the cathode surface,

$$\gamma_p j_{ion}(0) = j_e(0) . \tag{5}$$

As defined in Eq. (5), $\gamma_p$ includes all emission mechanisms and a correction for electrons that are elastically backscattered to the cathode. The composite value of $\gamma_p \approx 0.3$ is taken from the experimental results of Doughty *et al.*[24] The determination of $\gamma_p$ there is based on optogalvanic measurements of the electric field in a helium CF and the ion mobility as measured by Helm.[26]

The ion current density at the cathode is found by fixing the discharge current density $j_D$ throughout the discharge

$$j_D = j_{ion}(z) + j_e(z) . \tag{6}$$

The electron current density at the cathode can be

found once the total current density $j_D$ and the coefficient $\gamma_p$ are specified. The CS is therefore started by placing electrons into the mesh cells adjacent to the cathode with a chosen velocity distribution so as to satisfy the conditions of Eqs. (5) and (6). The distribution of electrons ejected from the cathode is also assumed in Monte Carlo calculations; a flat energy distribution with energies of less than 10 eV is typical[3,7,13,15,21,24] and reasonable in light of experimental measurements.[31]

### C. Self-consistent calculations

The self-consistent problem demands an extra condition on the electric field to completely specify a unique solution. This condition is discussed in Ref. 2. Within the present model, the simple ion transport description requires the ion velocity, and hence the ion current, to vanish any time the electric field nears zero. The extremum condition of Ref. 2 should be useful for the more ambitious electrode-to-electrode calculation and a full investigation of the CF-NG boundary.

A self-consistent-field calculation is started by first guessing a field configuration [Fig. 6(a)] and then running a fixed-field calculation to (near) stability. In comparisons with Doughty, his CF field measurements were used as the initial guess. As in the fixed-field calculation, the
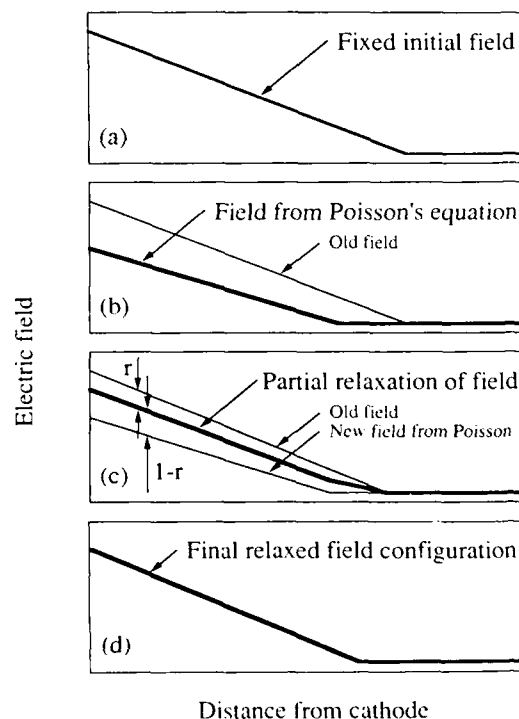


FIG. 6. Schematic of the field relaxation algorithm. Initial fixed-field configuration is guessed and the convective-scheme run to (near) stability (a). Poisson's equation is used to calculate a new field configuration (b). Old field is then allowed to relax a fraction r of the distance toward the new field (c). Partially relaxed field of (c) becomes the "old" field in (b) during the next iteration, and (b) and (c) are repeated until stability is again reached (d). Separation of the old and new fields, as well as the amount of relaxation r, have been exaggerated for clarity.

NG field is assumed to be directed toward the cathode with a magnitude of 10 V/cm, and the calculated field in the CF is matched to this value at the CF-NG boundary.

Once the fixed-field solution is found, Poisson's equation is combined with the field constraint $(j_{ion}=0$ if $E=0)$ to calculate an electric field. A search is made for the spatial location where the electrons carry the full discharge current, that is, where $j_e = j_D$. This defines the CF-NG boundary. (Such a point may not exist if the guessed field is too weak; the initial guess must then be modified.) The calculated field is set to zero at this point and its behavior in the CF is found by integrating toward the cathode using Poisson's equation. The 10 V/cm NG field is then imposed throughout the NG. A typical result at this stage is shown in Fig. 6(b).

The field being used in the run (currently the imposed field) is allowed to relax a fixed fraction $r$ (typically $r \approx 0.01$) of the difference between the field being used and the newly calculated field at each spatial location $z$ [see Fig. 6(c)]. A single time iteration of the CS is calculated with the new field configuration, then the field is again relaxed. This scheme consisting of a single CS time iteration followed by a partial field relaxation is continued until a stationary solution is again found, as in Fig. 6(d).

## VII. DISCUSSION OF SELF-CONSISTENT CALCULATION

The predicted electric field configuration for the $j_D = 0.190$ mA cm$^{-2}$ discharge of Doughty et al.[24] is presented in Fig. 7, along with the field measurements from optogalvanic experiments. The field decreases in a nearly linear fashion in the CF, as expected. The experimental and predicted fields are in good agreement in the high-field part of the CF. Factors influencing the predicted electric field will now be presented.

The slope of the predicted field in the CF is not directly dependent on the sophisticated kinetic treatment of the electrons; the electron density $n$ is a negligible fraction of

the ion density $n_+$ in the CF, so the ion density dictates the slope through Poisson's equation,

$$\frac{dE}{dz} = \frac{e}{\epsilon_0} n_+ . \tag{7}$$

The electric field is $E$, $\epsilon_0$ is the permittivity of free space, and $e$ is the unit charge $(e>0)$. Combining Poisson's equation with the current balance condition [Eq. (5)], continuity [Eq. (6)], and the mobility $(\mu_+)$ parametrization of the ion velocity $v_+$,

$$v_+ = \mu_+ (E)E , \tag{8}$$

yields a constraint on the electric field at the cathode,

$$\mu_+ (E)E\frac{dE}{dz} = \frac{j_D}{\epsilon_0(1+\gamma_p)} . \tag{9}$$

These considerations partially dictate the electric field configuration independent of the CS.

An accurate determination *has* been made of the electron current throughout the discharge, based on the de-
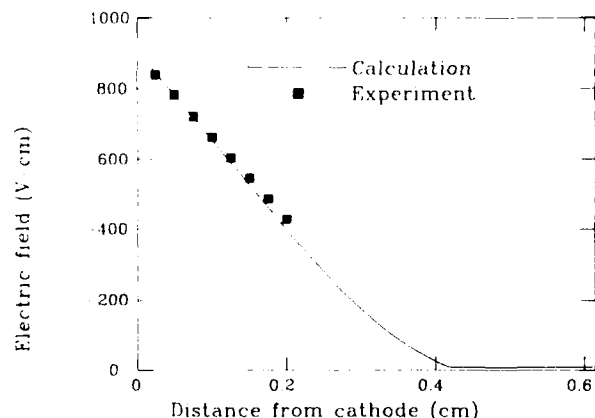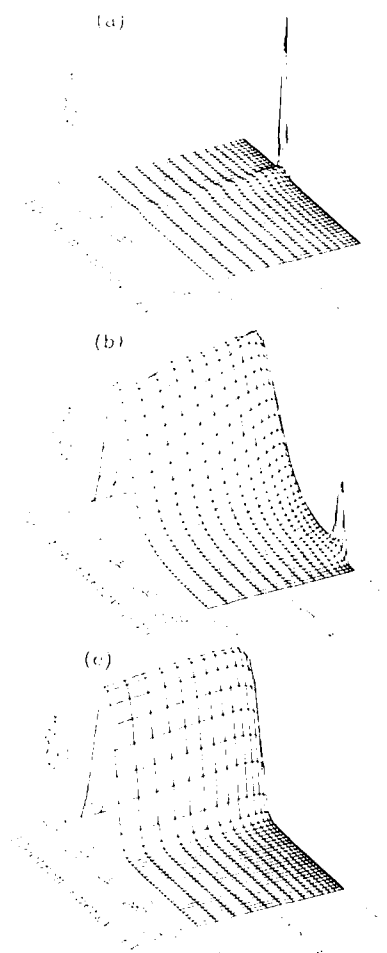


FIG. 8. Distribution functions from various spatial locations within the self-consistent CS calculation shown in Fig. 7. Distances from the cathode are (a) $z = 0.028$ cm (near the cathode), (b) $z = 0.243$ cm (midst of CF), and (c) $z = 0.489$ cm (midst of NG).



FIG. 7. Self-consistent electric field configuration as predicted by the convective scheme for the $j_D = 0.190$ mA cm$^{-2}$ discharge of Ref. 24. Experimental field points are optogalvanic measurements from the same reference.

tailed kinetic description of the CS. This, in turn, yields an accurate prediction of the ion current at all $z$ through the continuity requirement [Eq. (6)]. The location of the CF-NG boundary is then fixed by requiring $j_e = j_D$ ($j_{\text{ion}} = 0$) at the boundary.

The calculated electronic current is dependent upon the absolute accuracy of the ionization rate. The ionization cross section is from Alkhazov,[20] and the uncertainties have already been discussed. Two simplifying assumptions in the CS also affect the ionization rate. Associative ionization is not included, and all electrons leave scattering events with isotropic distributions. The first assumption underestimates the total ionization; the second overestimates it because the isotropic assumption results in more backscattered high-energy electrons that are more likely to undergo additional ionization events. Anisotropic elastic scattering is already present in the Monte Carlo simulations, and some of the effects of anisotropic inelastic scattering can be included by assuming that the two electrons leaving an ionization event scatter elastically after the event with no recoil from the ionized atom.[7] The Monte Carlo calculation indicates that the net result of these two assumptions is a slight underestimation of the ionization rate in the CS predictions in this near-normal discharge. An underestimation in the ionization rate corresponds to an overestimation of both the electric field strength in the CF and the length of the CF.

To emphasize the fully kinetic nature of this self-consistent calculation, distribution functions at three spatial locations in the discharge are presented in Fig. 8. Electrons that have survived unscattered from the cathode dominate Fig. 8(a), which is taken from near the cathode in the CF. Figure 8(b) is taken from the midst of

the CF, showing the expected buildup of inelastically scattered electrons. Electrons streaming through the NG from the CF to the anode are shown in Fig. 8(c); this region is dominated by electrons that have undergone several inelastic collisions. The distribution differs somewhat from a pure Maxwellian—high-energy electrons are depleted relative to a Maxwellian due to inelastic collision processes, and close inspection of Fig. 8(c) reveals a slight anisotropy of the NG electrons. These electrons are sometimes called "beam" or "ballistic" electrons because they are distinctly nonhydrodynamic electrons in the weak NG electric field; they are primarily responsible for excitation and ionization events in the NG.

Finally, the isotropic part of the distribution function versus position in the discharge and electron speed is shown in Fig. 9. The vertical scale of the graph has been truncated at one-tenth the largest magnitude of the distribution function to more clearly show the beam electrons that have survived unscattered from the cathode.

## VIII. SUMMARY

A convective-scheme method has been introduced to gaseous electronics in this paper. The method is more efficient than explicit finite difference schemes and able to accurately describe the time evolution of a plasma. The CS is very straightforward to implement, similar to Monte Carlo simulations. The CS was used to model two fixed-field discharges: a swarm experiment and the CF of a dc glow discharge. Predictions of the CS were shown to be consistent with Monte Carlo simulations. The swarm predictions were compared with experimental results, and uncertainties in both the experimental swarm results and the cross sections used in the CS were discussed. Self-consistent-field calculations of the CF were then presented. The field predicted by the self-consistent calculations was in excellent agreement with optogalvanic experiments. The accuracy of the electric field configuration was shown to depend on the detailed kinetic calculation primarily through the CS's prediction of the electron current. This, in turn, fixed the location of the CF-NG boundary and yielded the predicted electric field configuration.

The problems hampering the present model near this boundary would be avoided with an improved ion transport model. Physical and numerical considerations necessary for a realistic model of the NG were outlined. The efficiency of the CS should eventually allow a fully kinetic treatment of both the electrons and ions and a complete electrode-to-electrode calculation, including a detailed description of the true nature of the CF-NG boundary.
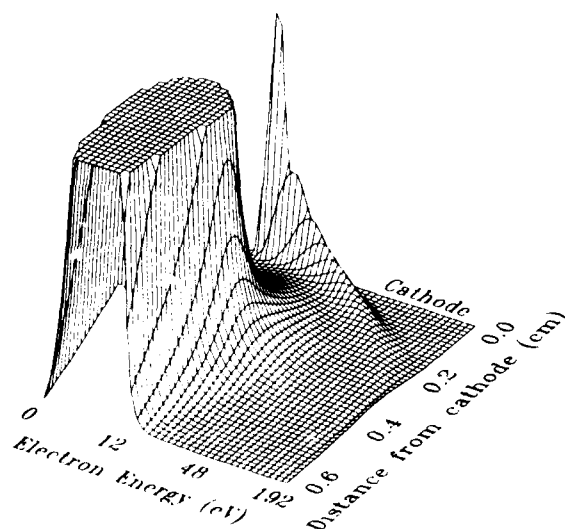


FIG. 9. Isotropic portion of the self-consistent electron distribution as a function of position within the discharge and electron speed. Vertical extent of the distribution function is truncated to show the unscattered beam of electrons from the cathode. Only every other mesh point in $z$ is plotted for clarity.

### ACKNOWLEDGMENTS

[1]T. J. Moratz, L. C. Pitchford, and J. N. Bardsley, J. Appl. Phys. **61**, 2146 (1987).

[2]T. J. Sommerer, J. E. Lawler, and W. N. G. Hitchon, J. Appl. Phys. **64**, 1775 (1988).

[3]P. Bayle, J. Vacquie, and M. Bayle, Phys. Rev. A **34**, 360 (1986).

[4]J. P. Boeuf, J. Appl. Phys. **63**, 1342 (1988).

[5]John H. Ingold, in *Gaseous Electronics*, edited by M. N. Hirsh and H. J. Oskam (Academic, New York, 1978), Vol. I, Chap. 2, p. 37.

[6]Pierre Segur and Robert Keller, J. Comput. Phys. **24**, 43 (1977).

[7]J. P. Boeuf and E. Marode, J. Phys. D **15**, 2169 (1982).

[8]P. Segur, M. Yousfi, J. P. Boeuf, E. Marode, A. J. Davies, and J. G. Evans, in *Electrical Breakdown and Discharges in Gases*, Vol. 89A of *NATO Advanced Study Institute, Series B: Physics*, edited by E. E. Kunhardt and L. H. Luessen (Plenum, New York, 1983), p. 331.

[9]K. Kitamori, H. Tagashira, and Y. Sakai, J. Phys. D **11**, 283 (1978).

[10]R. Courant, K. Friedrichs, and H. Lewy, Math. Ann. **100**, 32 (1928).

[11]L. C. Pitchford, in *Electrical Breakdown and Discharges in Gases*, Vol. 89A of *NATO Advanced Study Institute, Series B: Physics*, edited by E. E. Kunhardt and L. H. Luessen (Plenum, New York, 1983), p. 313.

[12]S. Yachi, Y. Kitamura, K. Kitamori, and H. Tagashira, J. Phys. D **21**, 914 (1988).

[13]Tran Ngoc An, E. Marode, and P. C. Johnson, J. Phys. D **10**, 2317 (1977).

[14]M. Ohuchi and T. Kubota, J. Phys. D **16**, 1705 (1983).

[15]E. A. Den Hartog, D. A. Doughty, and J. E. Lawler, Phys. Rev. A **38**, 2471 (1988).

[16]W. N. G. Hitchon, D. J. Koch, and J. B. Adams, J. Comput. Phys. (to be published).

[17]J. B. Adams and W. N. G. Hitchon, J. Comput. Phys. **76**, 159 (1988).

[18]A. V. Phelps and L. C. Pitchford, Phys. Rev. A **31**, 2932 (1985).

[19]R. W. LaBahn and J. Callaway, Phys. Rev. A **2**, 366 (1970); Phys. Rev. **180**, 91 (1969); *ibid.* **188**, 520 (1969).

[20]G. D. Alkhazov, Z. Tekh. Fiz. **40**, 97 (1970) [Sov. Phys.—Tech. Phys. **15**, 66 (1970)].

[21]D. A. Doughty, Ph.D. thesis, University of Wisconsin, 1987.

[22]H. N. Kücükarpaci, H. T. Saelee, and J. Lucas, J. Phys. D **14**, 9 (1981).

[23]J. Dutton, J. Phys. Chem. Ref. Data **4**, 577 (1975).

[24]D. A. Doughty, E. A. Den Hartog, and J. E. Lawler, Phys. Rev. Lett. **58**, 2668 (1987).

[25]D. K. Doughty and J. E. Lawler, Appl. Phys. Lett. **45**, 611 (1984).

[26]H. Helm, J. Phys. B **10**, 3683 (1977).

[27]J. E. Lawler, Phys. Rev. A **32**, 2977 (1985).

[28]Hugh E. Warner, William T. Conner, and R. Claude Woods, J. Chem. Phys. **81**, 5413 (1984).

[29]R. Deloche, P. Monchicourt, M. Cheret, and F. Lambert, Phys. Rev. A **13**, 1140 (1976).

[30]E. A. Den Hartog, T. R. O'Brian, and J. E. Lawler, Phys. Rev. Lett. **62**, 1500 (1989).

[31]Homer D. Hagstrum, Phys. Rev. **104**, 672 (1956).

APPENDIX F   (Pg. 64-67)

# Electron Heating Mechanisms in Helium rf Glow Discharges: A Self-Consistent Kinetic Calculation

T. J. Sommerer, [a] W. N. G. Hitchon, [b] and J. E. Lawler [a]

*University of Wisconsin, Madison, Wisconsin 53706*

(Received 22 August 1989)

Power dissipation mechanisms in low-pressure helium radio-frequency glow discharges are studied using a model which is able to describe the discharge at the kinetic level with a self-consistent electric field. We find a low average electron energy ($< 1$ eV) in the bulk plasma and a weak electric field ($\approx 2$ V/cm) that is largely out of phase with the sheath fields. The weak bulk field is shown to be important for heating electrons of all energies.

PACS numbers: 51.10.+y, 52.20.—j, 52.80.Hc

Fully self-consistent kinetic models of radio-frequency (rf) discharge plasmas are now possible using the "convective scheme" (CS).[1-4] Much progress toward understanding rf discharges has been made with more traditional models using the local-field approximation,[5] Monte Carlo simulations,[6,7] fluid approximations,[8] and other related approaches. Major challenges, such as the energy balance of the bulk electrons, are not easily addressed once the approximations inherent in these models have been made. Traditional models have sidestepped the energy balance of the bulk electrons by predicting only a density-temperature product,[9] calculating a spatially averaged energy balance for a restricted range of parameters,[10] or simply assuming a 1-eV average bulk electron energy.[11] A recent experiment shows that the average energy of the bulk electrons can be astonishingly low (0.043 eV).[12] We report in this Letter a fully kinetic model for rf discharge plasmas with a self-consistent electric field, and we use this model to study the energy balance of the bulk electrons.

An efficient numerical scheme based on propagators (Green's functions)[1-4] is employed here to yield distribution functions consistent with Poisson's equation for the electrons and ions in four He rf discharges. The kinetic model of the electrons described in Ref. 4 is modified[13] and combined with Poisson's equation and a kinetic description of the ions to yield a fully self-consistent, kinetic model. Energy loss by electrons during elastic collisions with neutrals has also been added here.

Calculations are typically started with a spatially uniform density of ions and electrons and run in the applied rf potential until the fractional change over a cycle in key quantities is less than a chosen value $c$. Typically, $c < 5 \times 10^{-4}$. Running to harmonic convergence is a most difficult problem because number densities (for instance) may continue to change by small amounts for many rf cycles. To avoid excessive computation times a run may be stopped, the particle densities adjusted (while preserving the net charge density at all spatial locations and hence the instantaneous field configuration), and then resumed from that point. The true final densities can thus be bracketed. We estimate that the present results differ from those of a perfectly converged solution by $< 15\%$ in absolute densities, better in most other variables.

Four sets of discharge conditions were considered. Most discussion will center on a "benchmark" 0.1-Torr He discharge with a gap of $d = 4$ cm, operating at a frequency $f_0 = 13.56$ MHz with an applied sinusoidal voltage $V^0 = 500$ V (peak). We assume 0.1 electron on average is released from an electrode per incident ion ($\gamma = 0.1$). Each of the other three discharges differs in one parameter: $V^0$, $f_0$, or $\gamma$. The results are summarized in Table I.

Results from the converged benchmark solution are shown in Fig. 1 over one rf cycle. The sheath electric

TABLE I. Summary of the results from the four He rf discharges. All discharges have an electrode spacing $d$ of 4 cm and a neutral He density $N$ of $3.535 \times 10^{15}$ cm$^{-3}$. The plasma potential, bulk ionization rate, and bulk average energy have been averaged over one rf cycle. The benchmark run is labeled "1."

| Run number | Potential amplitude $V^0$ (V) | rf frequency $f_0$ (MHz) | Secondary coefficient $\gamma$ | Current density $j\beta$ (mA cm$^{-2}$) | Plasma potential $V^{dc}(d/2)$ (V) | Maximum sheath length $L^{max}$ (cm) | Peak plasma density $n^{max}$ ($10^9$ cm$^{-3}$) | Peak ionization rate $S^{max}$ ($10^{14}$ cm$^{-3}$s$^{-1}$) | Bulk ionization rate $S(d/2)$ ($10^{14}$ cm$^{-3}$s$^{-1}$) | Bulk average energy $\langle \tau(d/2) \rangle$ (eV) | Bulk electric field $E^0(d/2)$ (V/cm) |
|---|---|---|---|---|---|---|---|---|---|---|---|
| 1 | 500 | 13.56 | 0.1 | 2.7 | 221 | 1.1 | 10.2 | 9.0 | 5.5 | 0.54 | 1.9 |
| 2 | 500 | 10 | 0.1 | 1.5 | 219 | 1.4 | 3.6 | 5.3 | 3.2 | 0.90 | 1.9 |
| 3 | 500 | 13.56 | 0.0 | 2.6 | 222 | 1.1 | 9.0 | 8.3 | 5.0 | 0.58 | 1.8 |
| 4 | 250 | 13.56 | 0.1 | 1.3 | 121 | 1.1 | 3.6 | 2.8 | 1.7 | 0.68 | 1.8 |

fields [Fig. 1(a)] are dominantly linear, reflecting a nearly constant (space and time) ion density outside the bulk and the dynamic action of the more mobile electrons as they move to neutralize ions in this region when the instantaneous field is small. ("Bulk" here refers to locations where the time-averaged field is weak; "sheath" refers to locations where the instantaneous field is strong.) The ion plasma frequency is of the order of the rf frequency; the ion density is nearly constant over a cycle, while the ion current to each electrode varies by around 30%. The electric field in the bulk ($E_{bulk}$) oscillates with a (roughly) spatially uniform amplitude of 1.9 V/cm. Surprisingly, $E_{bulk}$ is largely out of phase with the sheath fields, and is distinctly nonsinusoidal (Fig. 2). The field reversal occurs at the base of a given sheath while the sheath is reaching its maximum extent and also during the subsequent contraction. Conversely, the reversal is at the opposite side of the bulk when a sheath is minimal in extent and during the next expansion. The time-averaged fields in the bulk are roughly consistent with an ambipolar diffusion loss of ions.[14]

The average energy of the bulk electrons is low, averaging 0.54 eV over an rf cycle at the center of the discharge. Experiments have seen similar or even lower bulk electron temperatures in various He rf (Ref. 12) and dc (Ref. 14) discharges. At this pressure (0.1 Torr), the mean free path for ionization in He is several discharge lengths, and the ionization is due to high-energy electrons streaming through the discharge, as in a negative glow region or a beam-sustained discharge. The ionization rate (per unit volume) therefore peaks near the sheath-bulk boundary [Fig. 1(b)] as electrons that had migrated toward the electrode during the anodic part of the cycle are accelerated by the expanding sheath [Fig. 1(a)] during the cathodic phase. These discharges all appear to operate in a regime where sheath expansion is the dominant electron heating mechanism.[7,9,11] Figure 1(c) shows the deposition of power into the electrons; energy is given to the electrons during sheath expansion, but also flows from the particles into the field during sheath contraction. Bulk ion loss is dominated by a process analogous to ambipolar diffusion; that is, the product of the ion density, ion mobility, and average energy of the bulk electrons is approximately
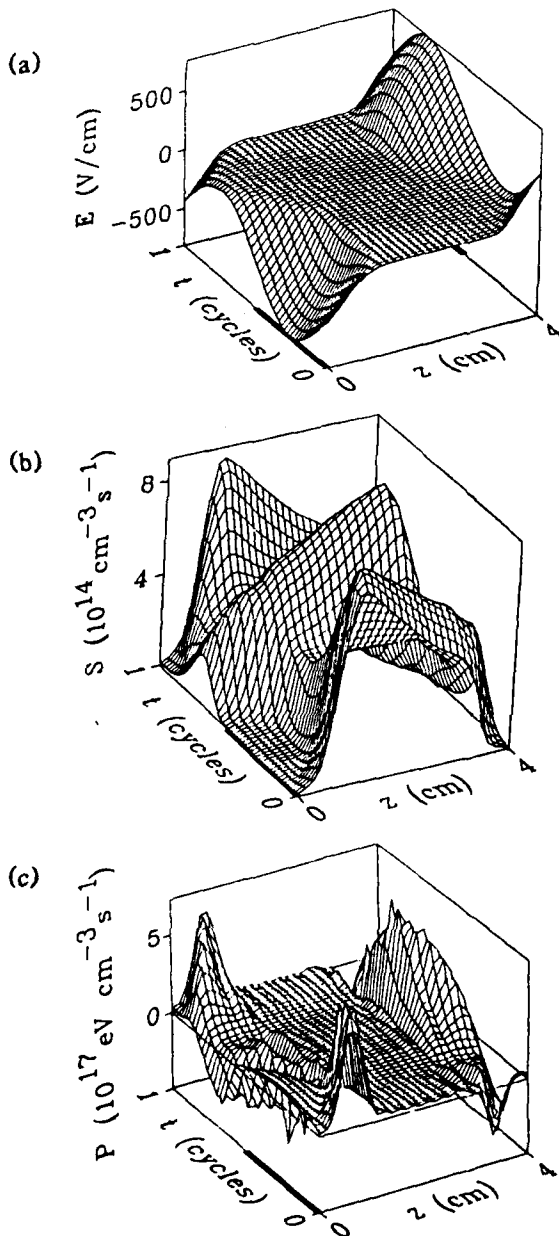


FIG. 1. Benchmark run: (a) electric field $E(z,t)$, (b) primary ionization rate per unit volume $S(z,t)$, and (c) power deposition into the electrons $P(z,t) = -n_e|e|E_z\langle v_z\rangle$, over one rf cycle $T = 7.375\times10^{-8}$ s. The heavy portions of the $z = 0$ and $z = 4$ cm lines indicate parts of the rf cycle where the corresponding electrode is cathodic.
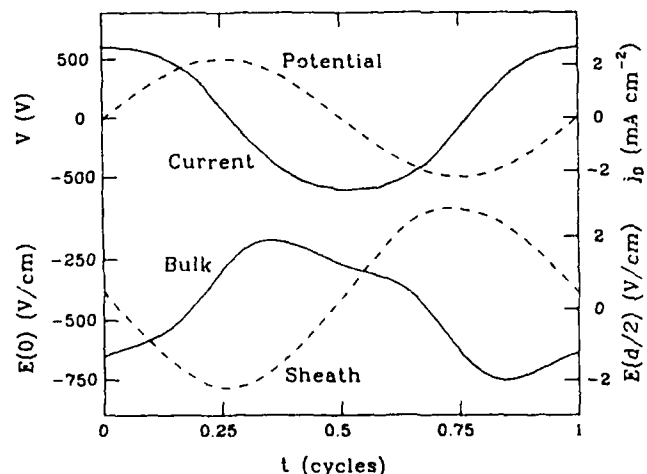


FIG. 2. The applied potential, discharge current, electric field at the $z = 0$ electrode, and bulk electric field ($z = d/2$) of the benchmark discharge over one rf cycle $T$.

equal to the product of the diffusion length squared and the average ionization rate.[14]

"Tracking" calculations utilizing the results of this benchmark discharge were used to examine the behavior of the bulk electrons. These runs were started when the left electrode was most cathodic [$t = T/4$ in Fig. 1(a)]. The electron distribution was cleared except for bulk electrons at one selected speed. These electrons were then followed for one or more cycles using the electric field and other results from the benchmark run as input to the tracking calculation. The true benchmark field was used initially. The role of $E_{bulk}$ in heating these electrons was clarified by modifying the benchmark field and performing identical tracking runs. Two variations were used: The first was to simply set $E_{bulk}$ to zero, and the second was to invert the sign of $E_{bulk}$. The strong sheath fields were not modified.

Low-energy (0.5-eV) bulk electrons respond to the bulk field, but require on the order of an rf cycle ($T = 7.375 \times 10^{-8}$ s) to cross the bulk and undergo several collisions during the crossing. The sheaths move with speeds of up to $\approx 5 \times 10^7$ cm/s [see Fig. 1(a)]. Low-energy electrons are gently pushed by $E_{bulk}$ toward an electrode as the sheath retreats toward that electrode during the anodic part of the cycle. They move too slowly to catch the retreating sheath, bounce, and lose energy. These slow electrons are unable to move away during the subsequent sheath expansion, and are heated as the sheath moves past. Setting $E_{bulk}$ to zero or inverting it inhibits the coldest electrons from moving in behind the retreating sheath and halves the total ionization due to these low-energy electrons during the first tracking cycle.

Higher-energy (15-eV) electrons can cross the bulk several times per rf cycle and have twice the mean free path of the 0.5-eV electrons; they can cross the bulk and collide with a sheath at any time. They gain energy from the field during collisions with expanding sheaths and lose energy to the field upon hitting a contracting sheath [Fig. 1(c)], and the energy gain or loss is dependent upon the relative speed of the electron and sheath. $E_{bulk}$ hinders heating of these high-energy electrons because for most of an rf cycle it slows electrons moving toward expanding sheaths and accelerates them toward contracting sheaths. Inverting or zeroing $E_{bulk}$ aids electron heating by the expanding sheaths and increases total ionization during the first tracking cycle by $\approx 20\%$.

An overwhelming majority of the discharge electrons have energies less than 1 eV, and only a tiny fraction of these cold electrons need be heated and subsequently ionize neutral atoms to sustain the discharge. Obtaining the correct $E_{bulk}$ and a realistic picture of the power balance is a prerequisite for a quantitative understanding of plasma chemistry. The 0.043-eV electrons observed by Hebner, Verdeyen, and Kushner[12] in He could attach to an electronegative gas and form negative ions, while the several-eV electrons predicted by Kushner[7,15] (various

molecular gases) and Graves and Jensen[8] (fictitious gas) would dissociate many molecular species. Though the Ar-SiH$_4$ discharges studied by Kushner[7] differ greatly from these He discharges, his conclusions regarding the magnitude of $E_{bulk}$ needed for significant bulk heating are largely applicable here. Power is not directly deposited into the bulk electrons in great quantity [Fig. 1(c)] in these discharges, but $E_{bulk}$ is the only source of energy for the coldest electrons. In one rf cycle even the coldest bulk electrons can gather sufficient energy from $E_{bulk}$ to be efficiently heated by the expanding sheaths.

The huge amount of information available in these kinetic calculations is evident in Fig. 3, which shows the isotropic part of the electron velocity distribution function (EVDF) of the benchmark run when the left electrode is most cathodic. There are very few electrons in the sheath. The secondary electrons liberated from the left electrode and accelerated to the sheath potential are clearly shown, as is the very low average energy of the bulk electrons. The full angular distributions corresponding to Fig. 3 shows the expected beam of secondaries traveling in the $+z$ direction and an isotropic distribution of low-energy electrons. The electrons in the local maximum in $f$ at $\tau \approx 250$ eV are secondaries which have been scattered and are moving transverse to the discharge axis.

Table I summarizes the three other calculations. The $E_{bulk}$ wave forms were remarkably similar for all of these discharges. The current leads the applied voltage by almost $\pi/2$, and is nearly sinusoidal (only the $3f_0$ harmonic, at 5%–7%, was more then 1% of the fundamental $f_0$).
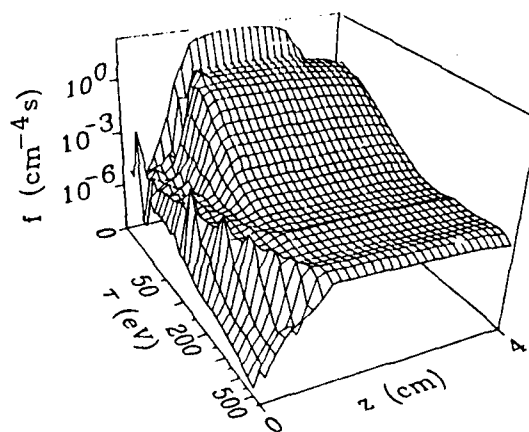


FIG. 3. Isotropic part of the EVDF of benchmark run. The left electrode is most cathodic at this phase of the rf cycle. $f = \sum_\mu N^{z v \mu}/A \Delta z \Delta v$, where $N^{z v \mu}$ is the number of electrons in one mesh cell centered at $z$, $v$, and $\mu = \cos\theta$. $\Delta z$, $\Delta v$, and $\Delta \mu$ are the dimensions of the cell, and $A$ is the area of the discharge. The energy axis is equally spaced in velocity, but labeled in energy units for convenience ($\tau = m v^2/2$). Note the overwhelming number of low-energy electrons and the beam of electrons ejected from the $z = 0$ electrode. The spikes in this beam are an artifact of the energy-conserving algorithm and the finite mesh size.

The ionization rates were all of the same form as Fig. 1(b), though differing significantly in magnitude. The similarity of the ionization rates of runs 1 and 3, which differ only in $\gamma$, shows that the electrons ejected from the electrodes by ion impact play only a minor role in these discharges. Run 2 differed from the benchmark by only 26% in rf frequency, yet differed markedly in overall ionization rate, plasma density, and bulk average energy.

We have used a self-consistent kinetic calculation of rf discharges to study the energy balance of the bulk electrons. The dominant electron heating mechanism in the discharges studied here is sheath expansion, yet the bulk electric field feeds energy into the coldest bulk electrons (which are the most numerous) and improves the efficiency of the sheath-expansion heating mechanism. It reduces the energy gained by higher-energy electrons by accelerating them toward contracting sheaths, where they bounce and lose energy, and slowing their movement toward expanding sheaths, where they gain energy. These kinetic calculations, in addition to addressing difficult challenges such as the energy balance of the bulk electrons, will enable us to explore the limits of various traditional approximations. They make possible accurate *a priori* predictions of discharge properties that are limited only by the quality of the physical approximations and the accuracy of the available electron emission coefficient and cross-section data.

[a]Department of Physics.

[b]Department of Electrical and Computer Engineering.

[1]J. B. Adams and W. N. G. Hitchon, J. Comput. Phys. **76**, 159 (1988).

[2]W. N. G. Hitchon, D. J. Koch, and J. B. Adams, J. Comput. Phys. **83**, 79 (1989).

[3]W. N. G. Hitchon, J. Plasma Phys. **41**, 323 (1989).

[4]T. J. Sommerer, W. N. G. Hitchon, and J. E. Lawler, Phys. Rev. A **39**, 6356 (1989).

[5]J. P. Boeuf, Phys. Rev. A **36**, 2782 (1987).

[6]R. W. Boswell and I. J. Morey, Appl. Phys. Lett. **52**, 21 (1988).

[7]Mark J. Kushner, IEEE Trans. Plasma Sci. **14**, 188 (1986).

[8]David B. Graves and Klavs F. Jensen, IEEE Trans. Plasma Sci. **14**, 78 (1986).

[9]V. A. Godyak and A. S. Khanneh, IEEE Trans. Plasma Sci. **14**, 112 (1986).

[10]G. R. Misium, A. J. Lichtenberg, and M. A. Lieberman, J. Vac. Sci. Technol. A **7**, 1007 (1989).

[11]J. P. Boeuf and Ph. Belenguer, in "Non-equilibrium Processes in Partially Ionized Gases," Proceedings of the NATO Advanced Study Institute, Acquafredda di Maretea, Italy, 4–17 June 1989 (to be published).

[12]G. A. Hebner, J. T. Verdeyen, and M. J. Kushner, J. Appl. Phys. **63**, 2226 (1988).

[13]W. N. G. Hitchon, T. J. Sommerer, and J. E. Lawler, in Proceedings of the Seventh IEEE Pulsed Power Conference, Monterey, California, 11–14 June 1989 (to be published).

[14]E. A. Den Hartog, T. R. O'Brian, and J. E. Lawler, Phys. Rev. Lett. **62**, 1500 (1989).

[15]M. J. Kushner, J. Appl. Phys. **54**, 4958 (1983).